# Modeling of the Atomic Structure and Electronic Properties of Highly Mismatched Amorphous $GaN_{1-x}As_x$ Alloys

**Ph.D. Thesis**

**in**

**Engineering Physics**

**University of Gaziantep**

**Supervisor**

**Prof. Dr. Beşire Gönül**

**by**

**Ebru Bakır Kandemir**

**DECEMBER 2013**

©2013 [Bakır Kandemir, E.]

T.C.
GAZİANTEP UNIVERSITY
GRADUATE SCHOOL OF
NATURAL AND APPLIED SCIENCES
ENGINEERING PHYSICS

| | | |
|---|---|---|
| Name of the Thesis | : | MODELING of the ATOMIC STRUCTURE and ELECTRONIC PROPERTIES of HIGHLY MISMATCHED AMORPHOUS $GaN_{1-x}As_x$ ALLOYS |
| Name of the Student | : | Ebru BAKIR KANDEMİR |
| Exam Date | : | 26.12.2013 |

Approval of the Graduate School of Natural and Applied Sciences.

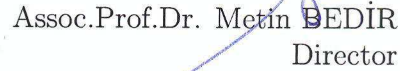

Assoc.Prof.Dr. Metin BEDİR
Director

I certify that this thesis satisfies all the requirements as a thesis for the degree of Doctor of Philosophy.

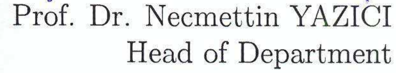

Prof. Dr. Necmettin YAZICI
Head of Department

This is to certify that we have read this thesis and that in our opinion it is fully adequate, in scope and quality, as a thesis for the degree of Doctor of Philosophy.

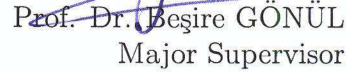

Prof. Dr. Beşire GÖNÜL
Major Supervisor

Examining Committee Members:

Prof. Dr. Beşire GÖNÜL

Prof. Dr. Oğuz GÜLSEREN

Prof. Dr. Bülent GÖNÜL

Prof. Dr. Hayriye TÜTÜNCÜLER

Asst.Prof.Dr.Koray KÖKSAL

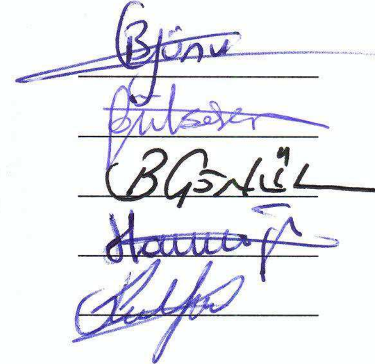

**I hereby declare that all information in this document has been obtained and presented in accordance with academic rules and ethical conduct. I also declare that, as required by these rules and conduct, I have fully cited and referenced all material and results that are not original to this work.**

**Ebru BAKIR KANDEMİR**

# ABSTRACT

MODELING OF THE ATOMIC STRUCTURE AND ELECTRONIC PROPERTIES OF HIGHLY MISMATCHED AMORPHOUS $GaN_{1-x}As_x$ ALLOYS

BAKIR KANDEMİR, Ebru

Ph.D. in Engineering Physics

Supervisor: Prof. Dr. Beşire GÖNÜL

December 2013, 100 pages

The aim of this thesis work is to model and investigate the properties of atomic and electronic behaviours of amorphous $GaN_{1-x}As_x$ alloys. For this goal, we have constructed structural models via molecular-dynamics simulations and continuous random network (CRN) methods. The nuclear positions were fully relaxed for all these generated models using density functional theory (DFT) calculations. The analysis of network topology has been achieved by examining partial-pair correlation functions (PDF), bond angle distributions, ring statistics and average coordination numbers. The electronic properties of $a-GaN_{1-x}As_x$ alloys have been estimated by means of electronic density states (EDOS) and inverse participation ratios (IPR). We then compared their structural and electronic properties with band anti-crossing (BAC) model and experiments. We have shown that a clear band gap which is similar to the experimental results could be obtained by CRN model which is at the same time computationally less expensive and reliable in comparison to other methods. The study of EDOS and IPR also proves that the obtained band gap are in good agreement with the experimental results and BAC model.

**Key words:** Continuous Random Network (CRN),Highly mismatched alloys (HMAs), a-GaNAs, amorphous semiconductors.

# ÖZ

YÜKSEK ÖRGÜ UYUMSUZ AMORF $GaN_{1-X}As_X$ ALAŞIMLARININ ATOMİK YAPILARININ VE ELEKTRONİK ÖZELLİKLERİNİN MODELLENMESİ

BAKIR KANDEMİR, Ebru

Doktora Tezi, Fiz. Müh.

Tez Yöneticisi: Prof. Dr. Beşire GÖNÜL

Aralık 2013, 100 sayfa

Bu tez çalışmasının amacı amorf $GaN_{1-x}As_x$ alaşımlarının atomik ve elektronik özelliklerinin davranışını modellemek ve araştırmaktır. Bu amaç doğrultusunda moleküler dinamik simulasyonları ve sürekli rastgele örgü modeli kullanılarak yapısal modeller oluşturduk. Bu oluşturulan modellerin atom pozisyonlarındaki yapı gerilimi yoğunluk alan fonksiyonu ile azaltıldı. Örgü topoloji analizleri kısmi-çift korelasyon fonksiyonları, bağ açı dağılımları, zincir istatistikleri ve ortalama komşuluk sayıları incelenerek elde edildi. Amorf $GaN_{1-x}As_x$ alaşımlarının elektronik özellikleri ise elektron durum yoğunlukları ve ters katılım oranları hesaplanarak belirlendi. Daha sonra bu modellerin yapısal ve elektronik özellikleri bant çakışmama modeli ve deney sonuçları ile karşılaştırıldı. Deney sonuçları ile uyumlu net bir bant aralığının güvenilir sürekli rastgele örgü modeli kullanılarak ve ayrıca diğer modellere göre daha ekonomik hesaplama zamanı ile elde edilebileceği gösterildi. Ayrıca kullanılan modelin amorf malzemeler için temel prensip hesapları ile ulaşılabilecek minimum enerji konfigurasyonuna yakın ideal bir temel yapı sağlayabildiğini doğruladık. Elektron durum yoğunlukları ve ters katılım oran hesapları ile elde edilen amorf $GaN_{1-x}As_x$ bant aralıklarının deney ve bant çakışmama modeli ile uyumlu olduğu ispatlandı.



**Anahtar kelimeler:** Sürekli Rastgele Örgü, Yüksek Örgü Uyumsuz Alaşımlar, a-GaNAs, amorf yarı iletkenler.

*I dedicate this work to intellectual curiosity*

## ACKNOWLEDGEMENTS

This work would not have been possible without the support, advice, friendship and help of a number of people. No words can describe the appreciation for all the support from my advisor, Prof.Dr. Beşire GÖNÜL, who is a great mentor on life. I am also very grateful to her for her tolerance in letting me pursue my own academic path in a new research area. Her invaluable guidance and optimistic attitude throughout this work was essential for all the achievements of the present work. I also wish to express my sincere gratitude to Prof.Dr. Bülent GÖNÜL who has always inspired me with his unique perspectives on life and physics.

I am very grateful to Dr. Wladek Walukiewicz, Dr. Kin Man Yu and Dr. Lin Wang Wang for accepting me in Solar Energy Materials Research Group and Computational Material Science and Nano Science Group to carry out a part of my research work under the funding from the Council of Higher Education of Turkey (YÖK). It was great opportunity for me to work with them. I am grateful for all of valuable feedbacks from them and also their group members. I also appreciate the provided computational time in NERSC and all the necessary facilities to carry out this Ph.D. work.

My gratitude and special thanks extends to Prof.Dr. Gerard Barkema, without his collaboration and his model this study would not be achieved. I also would like to thank to Prof.Dr. Oğuz Gülseren, who has always been so kind and helpful during this thesis.

There are, of course, many other people whose advice, discussions, comments and feedbacks have contributed to my Ph.D. work, both directly and indirectly. I owe particular thanks to Asst.Prof.Dr. Hüseyin Toktamis, Dilek Toktamis, Sedat Öztürk, Ömer Lütfi Ünsal for making my life easy and enjoyable with their friendship and unforgettable coffee breaks. Thank you one more time! I also would like to thank Engineering Physics staff.

I appreciate for all the supports and unconditional love from my parents throughout all these years. My sister Arzu and my cousin Ayşen have been my best friends along this journey, as always. Grateful thanks go to my beloved husband Zafer who supported me during the whole time of my work. I have learn a lot from him. To all of my relatives, friends and neighbors thank you for your

love, support and prayers. My heartfelt gratitude are for all of you for believing in me when I did not believe in myself thanks for your comforting words and your genuine support!

# TABLE OF CONTENTS

**CHAPTER**


**1** INTRODUCTION **1**

**2** THEORY AND FUNDAMENTAL CONCEPTS **5**
- 2.1 Introduction . . . 5
- 2.2 Semiconductor Alloying and Bandgap Engineering . . . 5
- 2.3 Highly Mismatched Alloys . . . 9
- 2.4 History of $GaN_xAs_{1-x}$ alloys . . . 13
  - 2.4.1 Band Anti-crossing Model . . . 14
  - 2.4.2 Growth of $GaN_xAs_{1-x}$ . . . 18
- 2.5 Amorphous semiconductor materials . . . 19
- 2.6 Summary . . . 24

**3** COMPUTER SIMULATION METHODS **25**
- 3.1 Introduction . . . 25
- 3.2 Classical Molecular Dynamics . . . 27
- 3.3 *Ab initio* Molecular Dynamics . . . 30
  - 3.3.1 Interaction Potentials and Forces . . . 30
  - 3.3.2 Density Functional Theory . . . 30
- 3.4 Continuous Random Network (CRN) . . . 32
  - 3.4.1 WWW algorithm to build a CRN . . . 32
- 3.5 Structural Properties . . . 34
  - 3.5.1 Basic definitions . . . 34
  - 3.5.2 Radial Distribution Functions . . . 34
  - 3.5.3 Ring Statistics . . . 37
- 3.6 Electronic Properties . . . 40
  - 3.6.1 Electronic Density of State (EDOS) and Inverse Participation Ratio (IPR) . . . 40
  - 3.6.2 Summary . . . 40

**4** MODELING OF THE AMORPHOUS $GaN_{0.5}As_{0.5}$ ALLOY **42**
- 4.1 Introduction . . . 42
- 4.2 *Ab initio* Molecular Dynamics Simulation of $GaN_{0.5}As_{0.5}$ . . . 43
- 4.3 Classical Molecular Dynamics Simulation of $GaN_{0.5}As_{0.5}$ . . . 45
  - 4.3.1 Three body Tersoff potential . . . 46
- 4.4 Continuous Random Network Modeling of $GaN_{0.552}As_{0.448}$ . . . 52
- 4.5 Summary . . . 55

**5** MODELING OF THE AMORPHOUS $GaN_{1-x}As_x$ ALLOYS **56**
5.1 Introduction . . . . . . . . . . . . . . . . . . . . . . . . . . . . . . . . 56
5.2 Atomic Structure of Amorphous $GaN_{1-x}As_x$ alloys . . . . . . . . . 57
5.2.1 Total Radial and Partial Pair Distribution Functions of $GaN_{1-x}As_x$ . . . . . . . . . . . . . . . . . . . . . . . . . 57
5.2.2 Bond Angle Distribution . . . . . . . . . . . . . . . . . . . . 60
5.2.3 Ring Statistics and Coordination Number . . . . . . . . . . 62
5.3 Electronic Properties of Amorphous $GaN_{1-x}As_x$ alloys . . . . . . . . . . . . . . . . . . . . . . . . . 64
5.4 Summary . . . . . . . . . . . . . . . . . . . . . . . . . . . . . . . . . 68

**6** CONCLUSIONS **70**

**REFERENCES** **73**

**PUBLICATIONS** **82**

## LIST OF TABLES

**Table**

2.1 Covalent and ionic radii of the elements in common group IV, $III - V$ and oxide semiconductors [18, 19]. . . . . . . . . . . . . . . 11
2.2 Electronegativity difference and mismatched classification for some semiconductors . . . . . . . . . . . . . . . . . . . . . . . . . . . . . . . 11

4.1 Parameter sets for the three interaction types [111, 112]. . . . . . 50

5.1 Fraction (%) of different types of bonds over the total number of bonds and average coordination number for an As concentration of $a - GaN_{1-x}As_x$ of $0.168, 0.304$ and $0.704$ . . . . . . . . . . . . . 63

## LIST OF FIGURES

**Figure**


2.1 Band gap versus lattice constant for some well known semiconductors. The right-hand scale gives the light wavelength $\lambda$, corresponding to the band gap energy at 300°K. . . . . . . . . . . . . . 6
2.2 The crystal structures of a) zincblende b) wurtzite and c) rocksalt structures. Dark sphere and bright sphere represent cation and anion, respectively. . . . . . . . . . . . . . . . . . . . . . . . . . . 7
2.3 The relationship between the bandgap and lattice constant for most III-V alloys. The curve for $GaN_xAs_{1-x}$ that exhibits huge bowing is a fit to experimental bandgaps on the GaAs-rich side using VCA. . . . . . . . . . . . . . . . . . . . . . . . . . . . 13
2.4 Illustration in k-space of the band anticrossing effects on the nitrogen level and GaAs conduction band . . . . . . . . . . . . . . . 14
2.5 Measured bandgap of $GaN_xAs_{1-x}$ as a function of x and its comparison with a) VCA [12] and b) BAC model [41] . . . . . . . . . 15
2.6 Measured bandgap of $GaN_{1-x}As_x$ as a function of x and its comparison with a) VCA [12] and b) VBAC model [41] . . . . . . . . 18
2.7 The energy dependence of the square of the absorption coefficient $\alpha^2$ for $GaN_xAs_{1-x}$ layers grown by Yu et al. [1] at different temperatures from $\sim 100$ to $\sim 600°C$. . . . . . . . . . . . . . . . . . . . 20
2.8 Schematic sketches of the atomic arrangements in (a) a crystalline solid, (b) an amorphous solid, and (c) a gas [**?**]. . . . . . . . . . . 21
2.9 A typical amorphous structure of 216-atom model of a-GaAs. Green (small sphere) represents Ga and white (larger sphere) represents As. . . . . . . . . . . . . . . . . . . . . . . . . . . . . . . . 21
2.10 Schematic representation of the density of states g(E) as a function of the energy E of an amorphous semiconductor (such as Si) near the region that corresponds to the band gap of the crystalline structure [51]. . . . . . . . . . . . . . . . . . . . . . . . . . . . 22
2.11 Schematic representation of Anderson localization in a one-dimensional periodic system of atoms. . . . . . . . . . . . . . . . . . . . . . 23

3.1 Schematic of the hierarchical multiscale modeling. . . . . . . . . . 26
3.2 General flow chart for classical MD simulations. . . . . . . . . . . 28
3.3 Diagram depicting the WWW bond transposition. Four atoms A, B, C, and D are selected following the geometry shown left; two bonds, AB and CD, are then broken and atoms A and D are reassigned to C and B, respectively, creating two new bonds, AC and BD, resulting in the geometry shown right. . . . . . . . . . . 33

3.4 Illustration of several definition of structural properties: a) tetrahedral bonding, b) corner-sharing tetrahedra, c) edge-sharing tetrahedra, d) nearest neighbor distance, e) bond angle and f) coordination number. . . . . . . . . . . . . . . . . . . . . . . . . . . 35
3.5 The density function $g(r)$ plotted as a function of $r$ for an amorphous solid. . . . . . . . . . . . . . . . . . . . . . . . . . . . . 35
3.6 Atomic structure of a) crystalline GaAs (c-GaAs) and b) amorphous GaAs (a-GaAs). Blue (dark sphere) represents gallium and white (bright sphere) represents arsenic. Total Radial distribution function for c) c-GaAs and d) a-GaAs . . . . . . . . . . . . . . . 37
3.7 a) King's shortest path criterion in the ring statistics: a ring represents the shortest path between two of the nearest neighbors (N1 and N2) of a given node (At). b) Guttman's shortest path criterion in the ring statistics: a ring represents the shortest path which comes back to a given node (At) from one of its nearest neighbors (N). . . . . . . . . . . . . . . . . . . . . . . . . . . . . . . 38
3.8 Primitive rings in the ring statistics: the AC ring defined by the sum of the A and the C paths is primitive only if there is no B path shorter than A and shorter than C which allows to decompose the AC ring into two smaller rings AB and AC. . . . . . . . . . . . . 39
3.9 The a) chair and b) boat configurations of six-atom rings. . . . . . 39

4.1 a) Initially random 216-atom model and b) Partial-pair distribution functions (PDFs) of initial $ZB - GaN_{0.5}As_{0.5}$. Blue (dark sphere), green and white (big bright sphere) spheres represents N, Ga and As atoms, respectively. . . . . . . . . . . . . . . . . . . 43
4.2 *Ab initio* Molecular Dynamics Scheme . . . . . . . . . . . . . . 44
4.3 Partial-pair distribution functions of 216 atom model of $a-GaN_{0.5}As_{0.5}$, obtained from AIMD method, before (dash line) and after (solid line) the relaxation. . . . . . . . . . . . . . . . . . . . . . . . . 45
4.4 Electronic Density of States (EDOS) of $a-GaN_{0.5}As_{0.5}$ calculated by LDA and LDA+C at 300K. Vertical line indicates the position of Fermi level, $E_F$. . . . . . . . . . . . . . . . . . . . . . . . . 46
4.5 Interatomic potential of a dimer with respect to interatomic distance. 47
4.6 Tersoff-Brenner type total potential energy for Ga-N, Ga-As, N-As, N-N, As-As and Ga-Ga dimers according to a) parameters suggested in K. Albe et al.[111, 112] and b) modified two body interaction terms as a function of atomic separation ($\AA$ ). . . . . . 49
4.7 Phase separation of $GaN_{0.5}As_{0.5}$ alloy as GaAs:N before the melting temperature . . . . . . . . . . . . . . . . . . . . . . . . . 50
4.8 Classical Molecular Dynamics Scheme . . . . . . . . . . . . . . . 51
4.9 The partial-pair distribution functions of *Ab initio* relaxed 216-atom model of $a - GaN_{0.5}As_{0.5}$ via classical molecular dynamics. . 52
4.10 Electronic density of states (EDOS) of $a - GaN_{0.5}As_{0.5}$ calculated by LDA and LDA+C based on classical molecular dynamics model simulation . . . . . . . . . . . . . . . . . . . . . . . . . . . . 52
4.11 a) The topology of $a-GaN_{0.552}As_{0.448}$ structure before and b) after DFT relaxation. . . . . . . . . . . . . . . . . . . . . . . . . . . 53

4.12 The partial-pair and total radial distribution functions of $a-GaN_{0.552}As_{0.448}$ after DFT relaxation. . . . . . . . . . . . . . . . . . . 54
4.13 Electronic density of states of 250 atom model of $a-GaN_{0.552}As_{0.448}$. The Fermi level is at 0 eV. . . . . . . . . . . . . . . . . . . . . . . 54

5.1 Total and partial-pair distribution functions (PDFs) of $a-GaN_{1-x}As_x$ for As concentrations of 16.8%, 30.4% and 70.4% by means of CRN model (left-hand side) and DFT relaxed (right hand side). A bin size of 0.1 Å used for calculations. . . . . . . . . . . . . . . . . . . 58
5.2 DFT relaxed 250-atom model of $a-GaN_{0.552}As_{0.448}$ cell. Red (small dark sphere) represents nitrogen, blue (big dark sphere) represents arsenic and yellow (bright sphere) represents gallium. . 60
5.3 Partial bond-angle distribution in amorphous $GaN_{1-x}As_x$ alloys for triple-correlation function As-Ga-As, N-Ga-N, As-Ga-N, Ga-N-Ga and Ga-As-Ga as a function of As concentrations. . . . . . . 61
5.4 Distribution of primitive rings per cell in $a-GaN_{1-x}As_x$ alloys. 62
5.5 Illustration of the presence of tetrahedrally bonded atoms for a $a-GaN_{0.832}As_{0.168}$ system. . . . . . . . . . . . . . . . . . . . . . . 64
5.6 The electron density of states and inverse participation ratio (IPR) of $a-GaN_{1-x}As_x$ alloys versus energy for 16.8%, 30.4% and 70.4% As concentrations. The dashed line shows the mobility edges of conduction- and valance-bands. . . . . . . . . . . . . . . . . . . . . 66
5.7 Electronic energy gap ($E_g$) versus arsenide concentration x for $GaN_{1-x}As_x$ alloys. Experimental concentration dependence of the bandgap of crystalline and amorphous GaNAs alloys and calculated concentration dependence according to BAC and our model results are shown. . . . . . . . . . . . . . . . . . . . . . . . . . . . 67

## LIST OF SYMBOLS

$HMA$ : Highly Mismatched Alloy

$MBE$ : Molecular Beam Epitaxy

$MOVPE$ : Metal-Organic Vapor Phase Epitaxy

$CRN$ : Continuous Random Network

$VCA$ : Virtual Crystal Approximation

$BAC$ : Band Anti-crossing

$EDOS$ : Electronic Density of States

$IPR$ : Inverse Participation Ratio

$RDF$ : Radial Distribution Function

$PDF$ : Partial-Pair Distribution Function

$MD$ : Molecular Dynamics

$AIMD$ : *Ab initio* Molecular Dynamics

$QM$ : Quantum Mechanics

$DFT$ : Density Functional Theory

$GGA$ : Generalized Gradient Approximation

$LDA$ : Local Density Approximation

$LDA+C$ : Corrected Local Density Approximation

$KS$ : Kohn-Sham

$WWW$ : Wooten, Winer and Weaire

$DTW$ : Djordjevic, Thorphe and Wooten

$NVT$ : Canonical Ensemble

$CN$ : Coordination Number

$VASP$ : Vienna *Ab initio* Simulation Package

$LAMMPS$ : Large-Scale Atomic/Molecular Massively Parallel Simulator

$ZB$ : Zinc-Blende

$CBM$ : Conduction Band Minimum

$HUMO$ : Highest Occupied Molecular Orbital

$LUMO$ : Lowest Unoccupied Molecular Orbital

$VBE$ : Valence Band Extended

$VBL$ : Valence Band Localized

$CBE$ : Conduction Band Extended

$CBL$ : Conduction Band Localized

# CHAPTER 1

# INTRODUCTION

Semiconductor alloys are material basis for modern technology including diode lasers, light-emitting diodes (LED), solar cells, transistors, photo detectors, high-electron-mobility transistors (HEMT), electro-optic modulators and many others. New and more specialized semiconductor alloys can solve the problems of today and tomorrow. At this point highly mismatched alloys (HMAs), a new class of semiconductor materials, can offer unique optical and electronic properties. HMAs include a class of III-V, II-VI and IV-IV compound semiconductors that are formed of materials with distinctly different electronegativities and atom size between host and substitutional atoms. The electronic properties of these materials, such as band gap, conduction- and the valence-band offset can be controlled by the alloy composition. Unusual properties of HMAs arise from dramatic restructuring of the electronic bands due to anti-crossing interaction between localized impurity states and the extended conduction or valance band states of the matrix. These unusual behaviors of HMAs can be successfully expressed by a simple band anti-crossing (BAC) model, including the composition and pressure dependence of the band gap, the presence of a new high energy transition and a nitrogen-induced enhancement of the electron effective mass.

$GaN_{1-x}As_x$ alloy, one of the most prominent example of HMAs, is the main subject of this thesis. The energy band gap of $GaN_{1-x}As_x$ can be continuously changed from 1.5 eV to 3.5 eV, making this material suitable for a variety of optoelectronic applications including low cost, high efficiency multi-junction solar cells. HMAs are immiscible under standard growth conditions and because of this only dilute HMAs (up to $\sim 10\%$) can be grown due to large differences in atomic size and electronegativity of the host and the alloying element. Recently K. M. Yu et al. and S. V. Novikov, et al.[1, 2] were overcome the miscibility gap of GaAs and GaN alloys using a non-equilibrium low temperature molecular beam epitaxy (LT-MBE) technique. They have managed to incorporate arsenic into a GaN film over the whole composition range to produce films of differing optical band gap properties depending upon the concentration of the As. They have reported that, it is possible to incorporate more and more As into GaN thin films by lowering

the growth temperature and increasing $As_2$ flux. However, they have obtained amorphous thin films in the composition range of $0.17 > x > 0.75$ under these conditions. The films had a crystalline nature outside this region [1, 2]. They also stated that the amorphous $GaN_{1-x}As_x$ films have a smooth morphology, homogeneous composition, and sharp well defined optical absorption edges. The energy band gap of amorphous $GaN_{1-x}As_x$ alloys measured by optical absorption experiments shows a monotonic decrease with increasing As concentration. The amorphous nature of the $GaN_{1-x}As_x$ alloys are particularly advantageous due to the fact that no lattice matching is required between adjacent amorphous layers and low cost substrates such as glass. Therefore amorphous $GaN_{1-x}As_x$ alloys are good candidates for full spectrum multi junction solar cells.

It has been seen from the experimental band gap of both As-rich [3] and N-rich [4] $GaN_{1-x}As_x$ that the theoretical models like virtual crystal approximation (VCA) or forced quadratic fitting cannot explain the experimental gap energies using a single bowing parameter. Surprisingly BAC model shows the same trend with the experimental gap energies through the full composition range. However, there is a lack of theoretical calculation for modeling amorphous $GaN_{1-x}As_x$ alloys to understand the nature of the electronic and structural properties. Thus this work has been strongly motivated to computational modeling of the atomic structure and electronic properties of amorphous $GaN_xAs_{1-x}$ alloys. We have reviewed different modeling techniques to describe realistic amorphous highly mismatched alloys. We have found that continuous random network model (CRN) with density-functional theory is an idealized model for perfectly coordinated amorphous semiconductors. This effective method has been successfully applied to generate model systems of $GaN_xAs_{1-x}$ as a function of As concentration. For all models, the network topology is analyzed through ring statistics, average coordination number, radial and angular distribution functions. The main features of the electronic structure are explained by analyzing the electronic density of states (EDOS) and inverse participation ratio (IPR).

This thesis begins with the basics of semiconductor physics focusing on semiconductor alloying and band gap engineering. It is accepted that the change in band gap can be explained by a linear interpolation of the constituent semiconductors for most of the semiconductor alloys. Therefore we present Vegards law and Virtual Crystal Approximation (VCA) to describe the variation of band gap by alloying. We next provide a description of the highly mismatched alloys (HMAs) and its anomalous properties with a discussion of isoelectronic impurities. We then focus on the history of $GaN_xAs_{1-x}$ alloy which is one of the most notable example of HMAs. It has been shown that the dramatic change of the energy gap of As- and N-rich $GaN_xAs_{1-x}$ alloys cannot be explained neither by

Vegards law nor VCA but band anti-crossing (BAC) model can. We further summarize the difficulties in the growth of $GaN_xAs_{1-x}$ alloys. It has been stated in the literature that even though it is possible to grow $GaN_xAs_{1-x}$ in the whole range by special low-temperature molecular beam epitaxy (LT-MBE) technique, the resulting alloys are amorphous in the intermediate compositional range. Finally, we present the basic concepts of amorphous semiconductor materials for better understanding of amorphous $GaN_xAs_{1-x}$ alloys.

Chapter 3 presents the computational simulations methods such as molecular dynamics (classical and *ab initio*) and continuous random network (CRN) to generate $GaN_xAs_{1-x}$ glass. A review of the classical and *ab initio* molecular dynamic methods is provided. We have then introduced the quenching from the melt technique based on these methods. These methods can be considered as a possible way to obtain structural information of amorphous materials and predict their physical properties. The continuous random network which plays an important role in modeling of amorphous $GaN_xAs_{1-x}$ (CRN) has been introduced by means of the Wooten, Winer and Weaire algorithm. Finally the most frequently used analysis methods for structure and electronic properties have been reviewed.

We have generated in chapter 4 an amorphous $GaN_{0.5}As_{0.5}$ by means of computer simulation methods that have been mentioned in chapter 3. The electronic structure calculations obtained using different methods have been compared with each other and also experiment. To achieve our purpose we have first studied the atomic and electronic structure of amorphous $GaN_{0.5}As_{0.5}$ by *ab initio* molecular dynamics method (AIMD) through the melt-quenching simulation. There was no energy gap for our generated $GaN_{0.5}As_{0.5}$ by AIMD contrary to experiments. In order to improve the quality of our generated structure to observe an energy gap consistent with experiment one needs to lower the melting temperature and/or increase the simulation time. With this way it is possible to achieve more realistic structure. However, this is computationally very expensive. So, although AIMD is powerful technique, we have decided to generate the same structure with classical molecular dynamics which is computationally much cheaper. Thus classical MD is presented as a second method. In this method, Tersoff potential is used with and without modified two body interaction terms as a force field to create our initial structure. The electronic density of states (EDOS) are calculated after *ab initio* relaxation. An energy band gap is not found for our generated amorphous $GaN_{0.5}As_{0.5}$ with this technique too. In spite of this deeper conduction- and valance band valley has been achieved by a reduction in homopolar bonds obtained by modified Tersoff potential. Finally, an initial structure is generated by means of CRN and performed relaxation. Our calculated results belonging this generated structure have shown that network do

not consist of any unwanted bonds and EDOS has a clear band gap similar to the experimental results.

The focus of chapter 5 is to provide a systematic study of atomic structure and electronic properties of amorphous $GaN_xAs_{1-x}$ as a function of As concentration by CRN model for the first time up to our knowledge. We have demonstrated that CRN provides an ideal initial network close to minimum energy configuration that can be reached from the first principle calculations for amorphous materials. We have also determined that the calculated bond lengths are in good agreement with the experimental data. An investigation of the coordination numbers, ring statistics, and bond angle distribution of amorphous $GaN_xAs_{1-x}$ has been carried out as well. It has been then concluded that generated systems have slightly disordered tetrahedral and bond angle characteristics which decrease with increasing As concentration. Our analysis has revealed that the band gap gets narrower with increasing As concentration in agreement both with experimental data and BAC model. We have then concluded that the CRN model is an ideal model to create initial structure to obtain realistic amorphous structures.

Finally, a summary of the thesis work is provided in chapter 6.

# CHAPTER 2

# THEORY AND FUNDAMENTAL CONCEPTS

## 2.1 Introduction

The objective of this chapter is to provide a review of the fundamental theoretical background of this dissertation. For this purpose, we firstly overview the bandgap engineering of semiconductor compounds. Secondly, we introduced the III-N-V based highly mismatched alloys covering the basic definitions. Thirdly we present the the $GaN_xAs_{1-x}$ alloys and theoretical models which can describe the novel properties of III-N-V based HMAs. Finally, we briefly survey the amorphous semiconductors and its electronic band structure.

## 2.2 Semiconductor Alloying and Bandgap Engineering

Compound semiconductors provide the materials basis for a number of well-established commercial technologies such as high-electron-mobility and heterostructure bipolar transistors, diode lasers, light-emitting diodes, photodetectors, electro-optic modulators and frequency-mixing components. The operating characteristics of these devices depend critically on the physical properties of the constituent materials. The ability to control all of the properties of a semiconductor is critical for device optimization. Thus, semiconductor alloying is a very important technique to tailor the materials properties like the electronic structure or optical behavior. Fig.2.1 shows the band gaps and lattice parameters for common elemental and binary semiconductors. The lines on this diagram represent ternary compounds which are alloys of the binaries labeled at their end-points. Materials shown in plain and italicized text refer to direct and indirect bandgap semiconductors, respectively. A direct band gap is more efficient than an indirect band gap at emitting and absorbing light, because direct bandgap transitions are between electrons and holes whereas a phonon is needed to achieve these transitions in an indirect semiconductor.

A semiconductor alloy is a combination of two or more elements. If an alloy has two component than it is called a binary alloy, for one with three is a ternary alloy. An alloy is formed from a physical mixture of two or more

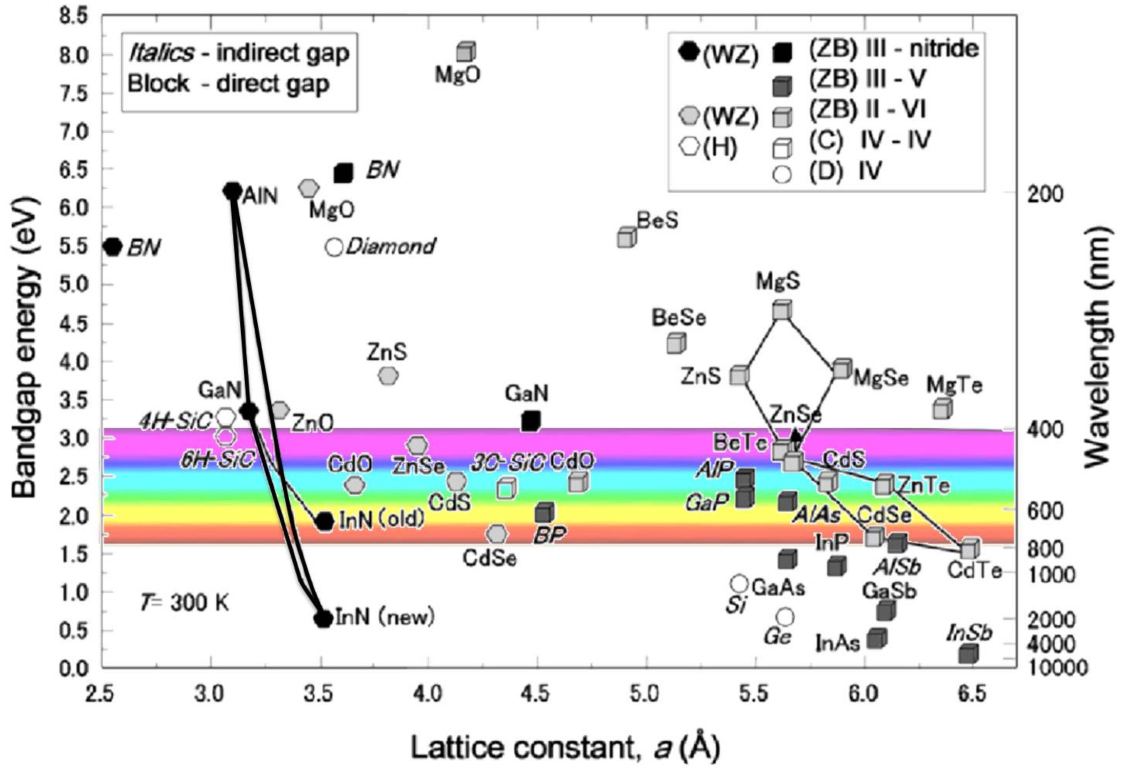


Figure 2.1: Band gap versus lattice constant for some well known semiconductors. The right-hand scale gives the light wavelength $\lambda$, corresponding to the band gap energy at 300°K [5].

substances, while a compound is formed from a chemical reaction. For example, GaAs is a compound consisting of Ga atoms bonded to As atoms. However, $GaN_xAs_{1-x}$ is an alloy compound consisting of GaN and GaAs with a mole ratio of $x : (1-x)$. Character of $GaN_xAs_{1-x}$ alloys have covalent and ionic terms. The bonds in diamond, C-C, can be described by the covalent bond term only. So it is an elemental semiconductor, like Si or Ge [6]. As can be seen from Fig.2.1, semiconductors with small lattice constants exhibit large band gap energy. The small lattice constant shows that the material exhibits strong interatomic forces, with the outermost shell electrons, that are responsible for chemical bonding, being strongly bound to the lattice thus leading to a large band gap energy.

Fig.2.2 illustrates the cubic (diamond and zincblende), hexagonal (wurtzite), and rock salt (NaCl) structures which are also represented by the hexagon and square symbols in Fig.2.1. The diamond, zinc blende and wurtzite structures are the three most common crystal structures of semiconductors. Zincblende structure consists of two interpenetrating face-centred cubic (fcc) lattices offset along the body diagonal by one quarter of the length of the diagonal. For binary compounds, atoms A and B represent different elements (zinc blende structure) and for elemental semiconductors atoms A and B represent the same element

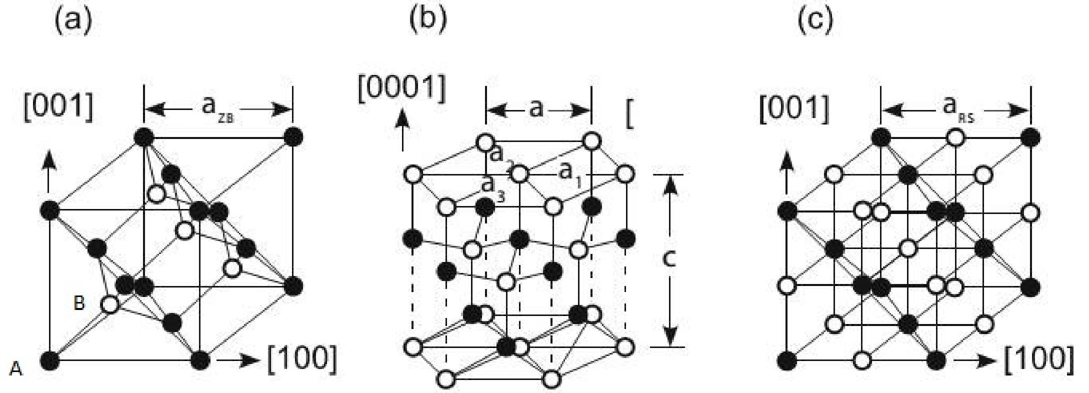


Figure 2.2: The crystal structures of a) zincblende b) wurtzite and c) rocksalt structures. Dark sphere and bright sphere represent cation and anion, respectively.

(diamond structure). Wurtzite is similar to the zinc blende structure, both are fourfold coordinated, except that the former has a hexagonal close-packed (hcp) bravais lattice rather than fcc. In Rock-salt crystal structure, Fig.2.2.c, each of the two atom types A and B forms a separate face-centered cubic lattice, with the two lattices interpenetrating so as to form a 3D checkerboard pattern.

The band gap of a semiconductor is dependent on the lattice parameter and electron phonon interaction; therefore, the temperature dependence of the band gap is related to the thermal expansion of the lattice and the temperature effects is related to the electron-phonon interaction. Traditionally, temperature variation of the band-gap energy Eg is expressed in terms of the Varshni formula as[7];

$$E_g(T) = E_g(0) - \frac{\alpha T}{T + \beta} \tag{2.1}$$

where $E_g(0)$ is the band-gap energy at $T = 0\,K$, $\alpha$ is in electron volts per Kelvin and $\beta$ is closely related to the Debye temperature of the material (in Kelvin).

The band gap change with alloying are generally linear or have a constant curvature. This linear behaviour can be explained by Vegard's law [8]. It states that the energy gap of a semiconductor alloy is calculated by a linear interpolation of the energy gap of the constituent semiconductor. Linear interpolations are also suggested for the electron masses in X and L valleys, split-off hole mass, and heavy-hole and light-hole masses along [001] direction. The lattice constants and elastic moduli may also be linearly interpolated. The energy gap can thus be expressed for $A_xB_{1-x}C$ alloy as a function of $E_{g(AC)}$ and $E_{g(BC)}$ energy gaps respectively:

$$E_{g(A_xB_{1-x}C)}(x) = xE_{g(AC)} + (1 - x)E_{g(BC)} \tag{2.2}$$

where $E_{g(AC)}$ and $E_{g(BC)}$ are the bandgaps of the binary constituents AC and BC. For some material parameters, however, energy gap calculations are deviate largely from the linear relation of Eqn.2.2. In this case, semiconductor alloys can usually be described by a quadratic polynomial in concentration x with the quadratic coefficient being called the bowing coefficient. Such as;

$$E_{g(A_xB_{1-x}C)}(x) = xE_{g(AC)} + (1-x)E_{g(BC)} - bx(1-x). \quad (2.3)$$

The bandgap bowing coefficient b, also known as optical bowing coefficient, describes the deviation from linearity and is close to a constant for most alloys. In the early 1970's, it was shown that the form of Eq.2.3 could be derived by considering the effects of alloy disorder within the currently available theoretical models, and that the value of b could be estimated by considering the electronegativity mismatch of the elements in the alloy [9, 10]. In early studies of electronic structures of random alloys in the 1930's, a linear dependence of the crystal potential on the alloy composition was adopted as a first order approximation [11]. In this approximation the composition disorder of the alloy is neglected, and the crystal potential of the alloy that the valence electrons feel is assumed to have perfect periodicity as in pure crystalline materials. The value of this periodic crystal potential is linearly interpolated between that of the endpoint crystals; therefore, the alloy is approximated by a new, perfect crystal with this interpolated crystal potential. This approach is named the Virtual Crystal Approximation (VCA). In the framework of VCA the bowing parameter for the bandgap of a semiconductor alloy is expected to be small, because there is no strong non-linearity in the dependence of the energy gap on the crystal potential in band-structure calculations. It has been proposed that the total bowing parameter should be the sum of the intrinsic bowing $b_i$ found in the VCA and the extrinsic bowing $b_e$ associated with disorder (non-periodicity)[9, 12].

For most III-V alloy bandgap is typically smaller than the linear interpolation result and so b is positive. Typically the magnitude of b is not dependent on the composition of the material. However, a much greater deviation from the VCA is observed in the bandgap of dilute nitride alloys of III-V compounds than in non-nitrogen containing mixed cation or anion III-V alloys. More importantly, the bowing parameter for dilute nitride alloys is composition dependent.

### Electronegativity

Electronegativity is a chemical property that describes the ability of an atom (or, more rarely, a functional group) to attract electrons towards itself in a covalent bond [13], and assigned the symbol $\chi$. An atom's electronegativity is affected by both its atomic weight and the distance that its valence electrons

reside from the charged nucleus. The higher the associated electronegativity number, the more an element or compound attracts electrons towards it. The metals are electropositive and the non-metals are electronegative, such that there is a broad sweep from the most electropositive metal at the bottom left (cesium, Cs, $\chi = 0.7$) to the most electronegative non-metal to be found top right (fluorine, F, $\chi = 3.98$) of the long form of the periodic table.

Electronegativity cannot be directly measured and must be calculated from other atomic or molecular properties. Electronegativity, as it is usually calculated, is not strictly an atomic property, but rather a property of an atom in a molecule[14]. Several methods of calculation have been proposed using physical parameters including enthalpy data, ionisation energy and electron affinity, effective nuclear charge and covalent radius etc., although there may be small differences in the numerical values of the electronegativity, all methods show the same periodic trends between elements. Due to the importance of Paulings scale[14] where electronegativity ranges from Cs, $\chi = 0.7$ to F, $\chi = 4.0$, all the other electronegativity scales are routinely normalised with respect to Paulings range. Strong correlations between numerous atomic parameters, physical and chemical, the term electronegativity integrates them into a single dimensionless number between 0.78 and 4.00 that can be used to predict much of an elements physical character and chemical behaviour.

## 2.3 Highly Mismatched Alloys

Typical semiconductor alloys are formed from elements with similar atomic radii and electronegativity (e.g., AlGaAs, GaAsP). However, over the last decade, it has been well established that the isoelectronic substitution of anions with very different ion size and/or electronegativity can result in dramatic restructuring of the electronic bands of semiconductor alloys. Such semiconductor alloys have been known as highly mismatched alloys (HMAs)[15]. Highly mismatched alloys include a class of III-V and II-VI compound semiconductors such as $GaN_xAs_{1-x}$, $GaBi_xAs_{1-x}$, $GaSb_xAs_{1-x}$, $ZnS_xTe_{1-x}$, $ZnTe_xSe_{1-x}$ and $ZnO_xTe_{1-x}$. Because of large miscibility gaps, typically HMAs consist of a host semiconductor matrix with the substitution of only a small amount of distinctly different isovalent atoms. Fundamental properties of host material dramatically changes with this very small amount of isovalent atoms. For example, dilute $III-V$ nitrides (up to $\sim 10\%$) shows unusual effects such as

- localization of states near the conduction band minimum (CBM)
- giant band gap bowing, and

- composition dependent bowing.

This is in contrast to conventional semiconductor alloys such as GaAsP and AlGaAs whose physical, electronic and optical properties can be deduced from a linear interpolation between their corresponding end point compounds with only a slight deviation, as predicted by the virtual crystal approximation (VCA). The properties of highly mismatched alloys (HMAs) deviate drastically from the predictions of the VCA. The unusually strong dependence of the fundamental gap on the N content in the group III-N-V alloys has been well described by the anticrossing interaction between localized N states and the extended conduction band states of the III-V matrix [16, 15, 17]. This model which can accurately describe the composition and pressure dependencies of the fundamental band gaps of HMAs is called Band Anticrossing (BAC) (in section 2.4.1).

### Isoelectronic Impurities

Isovalent or isoelectronic impurities are known as the substitutional impurity which has the same valance as the substituted atoms in the host lattice. Although they have the same valency, the impurity atom may differ from the host atom in many other aspects, such as a different atom size and different electronegativity which results dramatic restructuring of the electronic bands of semiconductor alloys. The radii of the elements in common group IV, $III-V$, and oxide semiconductors are shown in Table.2.1. The covalent radius is merely the measured radius when two atoms are pulled closely together to the point at which they are just touching. Ionic radii depend on two factors; the degree of ionization and the number of neighboring atoms (or coordination number). The length of an ionic bond reflects a balance between the electrostatic Coulomb attraction of the unlike charges and the mutual Born repulsion of the positively charged nuclei.

Table2.2 presents the classification of the semiconductor alloys in three categories according to the difference in the electronegativities between host and substituted atoms (isovalent atoms). Isovalent atom/impurity creates a perturbation to the host band structure, this perturbation is usually small, hybridizes with the host states and remains unnoticeable. But if electronegativity, size and ionization energy difference are big these impurity can act as a deep center with localized potential. For example, substituting In for Ga or P for As in GaAs produces a very weak perturbation whereas substituting N for P in GaP produces excitonic bound states. Isovalent impurities creating bound states are generally referred to as isoelectronic impurities and impurities attractive to electrons and holes are often termed as pseudo-acceptors or pseudo-donors, respectively. Creat-

Table 2.1: Covalent and ionic radii of the elements in common group IV, $III-V$ and oxide semiconductors [18, 19].

| Element | Covalent radius (A) | Ionic radius (A) |
|---|---|---|
| Si | 1.17 | - |
| Ge | 1.22 | - |
| Ga | 1.25 | - |
| In | 1.5 | - |
| N | 0.7 | - |
| P | 1.1 | - |
| As | 1.21 | - |
| B | 0.81 | - |
| Al | 1.25 | - |
| Sb | 1.41 | - |
| O | - | 1.4 |
| Ti | - | 0.745 |
| Zn | - | 0.74 |
| U | - | $1.14^{\dagger}$ |
| Co | - | 0.79 |

ing a highly localized center is attractive to one type of carrier via a short-range potential. The trapped carrier can subsequently bind a carrier of opposite charge via coulombic interaction. Therefore, an isoelectronic impurity can bind excitons [20].

Table 2.2: Electronegativity difference and mismatched classification for some semiconductors [12]

| Highly Mismatched Alloys | Electronegativity difference (eV) |
|---|---|
| III-N-As | 1.0 |
| III-N-Sb | 1.2 |
| III-N-P | 0.9 |
| II-O-Te | 1.4 |
| II-O-Se | 1.1 |
| II-O-S | 1.0 |
| Moderately Mismatched Alloys | Electronegativity difference (eV) |
| II-S-Te | 0.4 |
| II-Se-Te | 0.3 |
| Lightly Mismatched Alloys | Electronegativity difference (eV) |
| III-P-As | 0.1 |
| II-S-Se | 0.1 |

The impurity energy levels are not sensitive to the positions of the conduc-

tion and valance band edges since the deep states have localized wavefunctions in real space which may involve Bloch functions from several bands over a large region of k-space. Thus it is not expected to shift significantly in energy with a change in composition or pressure [17]. To calculate the energy positions of these deep levels, one needs to know the defect potential and then solve the corresponding Schrödinger equation. In many cases the exact functional form of the localized potential is not very crucial; the deep center wavefunction is predominantly determined by the host crystal rather than by the deep impurity. The main difficulty of the problem lies in the second step, i.e., finding the solution to the Schrödinger's equation. In 1980, Hjalmarson et al. made the first systematic theoretical investigation of this problem [21]. Employing a Koster-Slater model for the localized potential, they established the eigenvalue equation in a tight-binding-function basis. For $A_1$ symmetry deep states tend to lie in a range of energies relative to the vacuum level that happens to be near the conduction band edges of most semiconductors, while those with $T_2$ symmetry are located near the valence band edges. This generalized theory is intended to identify the broad chemical trends in the localized levels of the impurities and is therefore effective in predicting the approximate behavior of an impurity within a host crystal. When the defect potential is restricted to nearest neighbor distances, the problem is simplified to a difference in s-orbital energies of the impurity and host for $A_1$ symmetries and p-orbital energies for $T_2$ symmetries.

The nature of the impurity within the host will ultimately determine the symmetry of the deep center and consequently its location within the bandstructure of the host semiconductor. Highly electronegative isoelectronic impurities, such as N in $III{-}V$ compounds, act as weak acceptors and localize electrons in $A_1$ states near the conduction band edge of the host. For example, the $KosterSlater$ theory predicts that the N defect level is resonant with the conduction band in GaAs, while it is bound just below the conduction band minimum (CBM) of GaP [21]. These calculations correspond quite well with experimental observations [22, 23]. Oxygen in $II - VI$ compounds behaves in a similar manner and is a bound $A_1$ state in ZnTe [24]. Likewise, C is expected to lie within the conduction band of both Si and Ge [21]. Metallic impurities, on the other hand, act as weak donors and localize holes in a $T_2$ state near the valence band of the host semiconductor. For example, As defect level lies just above the valence band edge of GaN [25, 4]. Sb and Bi have a lower ionization energy than As as well, and their defect levels are also predicted to lie near or within the valence bands of other $III - V$ compounds [26, 27]. These approximate trends serve as a guide to the behavior of dilute nitrides and other moderately and highly mismatched alloys.

## 2.4 History of $GaN_xAs_{1-x}$ alloys

III-V compound semiconductors have been the focus of a major research effort in the recent years. In the case of As-rich $GaAs_{1-x}N_x$ and N-rich $GaN_{1-y}As_y$ alloys, one important reason for this interest is their capability to produce light in a wavelength region which reaches from infrared to ultraviolet. This makes them very attractive e.g. for optoelectronic applications. The band gap change with alloying show band bowing for most of the compound semiconductor alloys. For GaAsN alloys this effect is very strong, which allows large changes in the bandgap value with a small change in composition. If we use Eqn. 2.3 to describe the energy gap of $GaN_xAs_{1-x}$ with x up to about 0.05 would require a bowing parameter greater than 14 eV, and would predict a negative bandgap for a large range of compositions as shown in Fig.2.3.

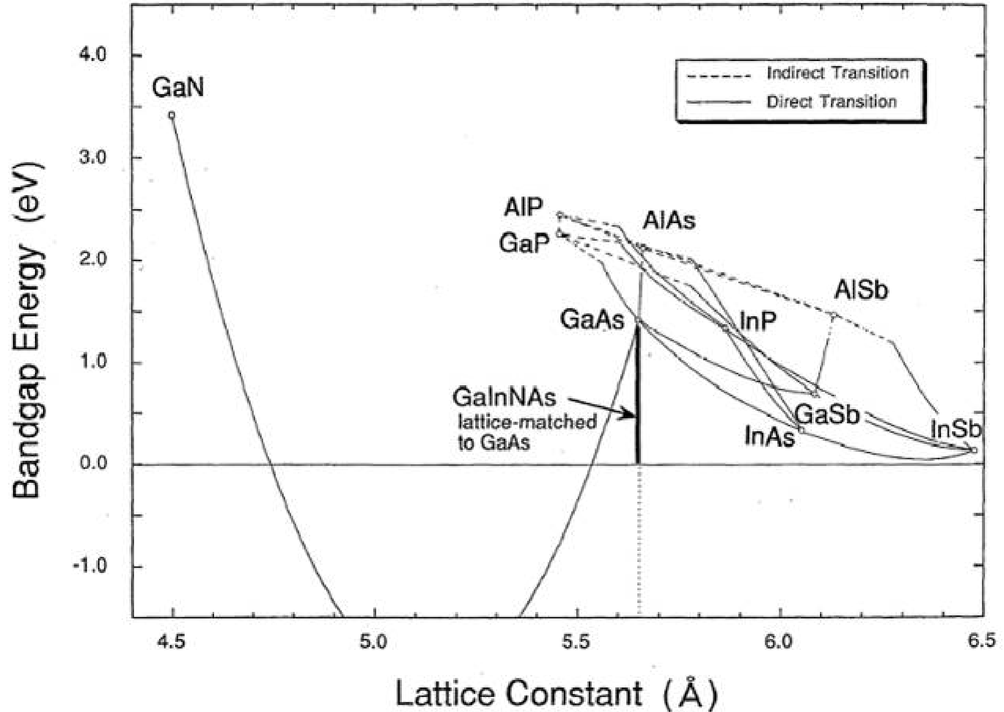


Figure 2.3: The relationship between the bandgap and lattice constant for most III-V alloys. The curve for $GaN_xAs_{1-x}$ that exhibits huge bowing is a fit to experimental bandgaps on the GaAs-rich side using VCA [12].

Because of the large size mismatches between N atoms and As atoms, Stable alloys are only found to grow in very narrow composition ranges near the binary endpoints (miscibility gap) [28, 29, 30, 31]. For the the As-rich GaNAs, the band-anticrossing (BAC) model is usually used to describe the dependence of the band gap energy on their compositions [32, 33, 34, 35, 36]. For the N-rich GaNAs, only a few investigations on the band gap energy have been reported [37, 38, 39, 40].

### 2.4.1 Band Anti-crossing Model

#### Conduction Band Anti-crossing Model

Shan et al. [16] have shown that unusual behaviours of HMAs can be quite well understood within a simple band anti-crossing (BAC) model. The model explains the properties of HMAs, including the composition and pressure dependence of the band gap, the presence of a new high energy transition and a nitrogen-induced enhancement of the electron effective mass. The BAC model treats the interaction of the localized defect states and the extended states of the conduction band in analogy to perturbation theory for a two-level system. This interaction leads to a splitting of the matrix band into two characteristic non-parabolic bands that are typically labeled $E_+$ and $E_-$ for the high and low energy bands respectively. The resulting bands have mixed localized and delocalized character from the interaction of the two types of states [41].

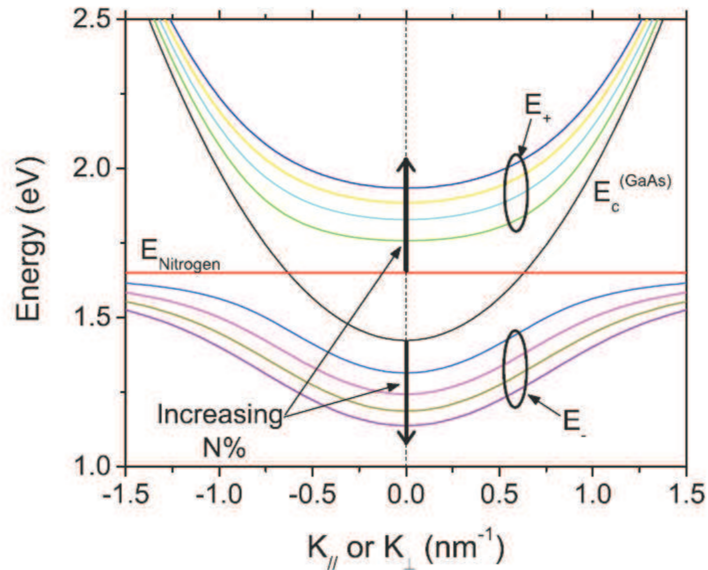


Figure 2.4: Illustration in k-space of the band anticrossing effects on the nitrogen level and GaAs conduction band [42]

The alloying of an HMA can be treated as an anti-crossing interaction if it is assumed that the defect states are randomly distributed over the lattice, replace the anion sites, and are weakly coupled to the host lattice. First for the case of the substitution of a more electronegative anion into the lattice results in an energy level close to the conduction band. The eigenvalue problem for the perturbed system can be written as:

$$\begin{vmatrix} E_M(k) - E(k) & V_{MD} \\ V_{MD} & E_D - E(k) \end{vmatrix} = 0 \qquad (2.4)$$

where $E_M(k)$ is the dispersion relation for the unperturbed host conduction band, $E_D$ is the defect energy level, $E(k)$ is the dispersion relation of the perturbed system that are all relative to the valence band edge (VBE). $V_{MD} =< k|V|D >$ is the matrix element describing the coupling between the localized defect states, D, and the extended host matrix conduction band states. The matrix element, $V_{MD}$, can be simplified to $C_{MN}x^{1/2}$ assuming that the defect states are randomly distributed and their concentration is low enough so there is no appreciable defect state wavefunction overlap. $C_{MN}$ is an empirically determined coupling constant between the extended matrix states and the localized defect states and x is the mole fraction of the defect. The solution to Eqn.2.4 is then

$$E_{\mp}(k,x) = \frac{E_M(k) + E_D \mp \sqrt{(E_M(k) - E_D)^2 + 4C_{MD}^2 \cdot x}}{2} \quad (2.5)$$

so the original system of a parabolic band and a localized defect level results in a splitting into two highly non-parabolic bands, $E_+(k)$ and $E_-(k)$, that depend on the composition, x. $E_-(k)$ becomes the new conduction band dispersion relation of the alloy and defines the band gap. Fig.2.4 shows the $GaN_xAs_{1-x}$ where the defect level is resonant with the conduction band. As the alloying is increased, the separation between $E_+$ and $E_-$ increases and the band gap decreases as can be seen in Fig.2.4.

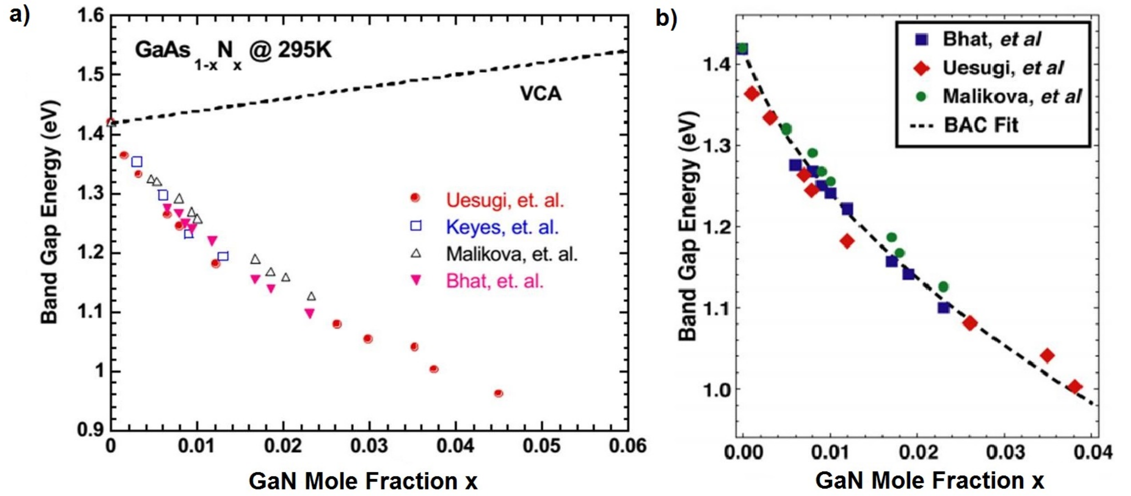


Figure 2.5: Measured bandgap of $GaN_xAs_{1-x}$ as a function of x and its comparison with a)VCA [12] and b) BAC model [41]

The composition dependence of the bandgap of $GaN_xAs_{1-x}$ according to measurements and virtual crystal approximation and BAC model are shown in

Fig.2.5a and b, respectively. As can be seen clearly the bandgap dependence deviates significantly from the VCA prediction. Even the trend of the change in the bandgap is reversed from the VCA dependence on the As-rich side. While the VCA predicts a slight increase in the bandgap, it is observed the bandgap energy dropping rapidly as a function of N concentration. In the As-rich side a huge bowing parameter (more than 14 eV) is required to express this strong composition dependence by a quadratic polynomial. However, BAC fits show very good agreement with the experimental data and provide a physical explanation for how alloying with a highly dissimilar anion changes the band structure of the HMA (Fig.2.5b). The BAC has been calculated for the band gap dependence on composition for $GaN_xAs_{1-x}$ with $C_{MN} = 2.70eV$ and $E_N = 1.65eV$.

**Valance Band Anti-crossing Model**

The complimentary case to the nitrogen defect in GaAs is the arsenic defect in GaN. The more metallic and larger arsenic atom replaces the highly electronegative nitrogen anion. It has been reported that the doping of GaN with arsenic results in a new emission band at about 2.65 eV [63]and the arsenic defect level has been theoretically predicted to lie 0.4 eV above the valence band [64]. Fig.2.6 shows the experimentally determined band gap for $GaN_{1-x}As_x$ (GaN-rich), along with the bowing parameter determined for $GaAs_{1-x}N_x$ (GaAs-rich) and the virtual crystal approximation [65]. As GaAs is alloyed with GaN there is a discontinuous decrease in the band gap as it shifts from 3.4 eV to about 2.6 eV, where the arsenic defect level resides. The band gap continues to decrease with increasing arsenic concentration. Neither the bowing parameter nor the VCA fit the experimental data.

The full treatment of this system considers the perturbation of the valence band due to the presence of the metallic defects through $k \cdot p$ formalism. The approach is the same as the conduction band anti-crossing model, except that a 6x6 matrix element is needed to describe the valence bands and the p-type defect level. The metallic defects are p-type states with $T_2$ symmetry, which are represented by a 6x6 matrix. The valence band Hamiltonian is constructed on

the basis of the six time-reversal symmetry invariant wavefunctions:

$$\left|\frac{3}{2},\frac{3}{2}\right\rangle = \frac{1}{\sqrt{2}}|(X+iY)\uparrow\rangle \tag{2.6a}$$

$$\left|\frac{3}{2},\frac{1}{2}\right\rangle = \frac{i}{\sqrt{6}}|(X+iY)\downarrow -2Z\uparrow\rangle \tag{2.6b}$$

$$\left|\frac{3}{2},\frac{-1}{2}\right\rangle = \frac{1}{\sqrt{6}}|(X-iY)\uparrow +2Z\downarrow\rangle \tag{2.6c}$$

$$\left|\frac{3}{2},\frac{-3}{2}\right\rangle = \frac{i}{\sqrt{2}}|(X-iY)\downarrow\rangle \tag{2.6d}$$

$$\left|\frac{1}{2},\frac{1}{2}\right\rangle = \frac{1}{\sqrt{3}}|(X+iY)\downarrow +Z\uparrow\rangle \tag{2.6e}$$

$$\left|\frac{1}{2},\frac{-1}{2}\right\rangle = \frac{i}{\sqrt{3}}|(-X+iY)\uparrow +Z\downarrow\rangle \tag{2.6f}$$

Using the standard 6x6 Kohn-Luttinger $k \cdot p$ matrix describing the $\Gamma_7$ and $\Gamma_8$ valence bands, the random distribution of impurities can be resolved through configurationally averaging within the coherent potential approximation. The 6x6 valence band matrix is enhanced by the 6x6 defect matrix resulting in a 12x12 matrix is given by: $H_v =$

$$\begin{bmatrix}
H & \alpha & \beta & 0 & \frac{i\alpha}{\sqrt{2}} & -i\sqrt{2}\beta & V(x) & 0 & 0 & 0 & 0 & 0 \\
\alpha^* & L & 0 & \beta & \frac{iD}{\sqrt{2}} & i\frac{\sqrt{3}}{\sqrt{2}}\alpha & 0 & V(x) & 0 & 0 & 0 & 0 \\
\beta^* & 0 & L & -\alpha & -i\frac{\sqrt{3}}{\sqrt{2}}\alpha^* & \frac{iD}{\sqrt{2}} & 0 & 0 & V(x) & 0 & 0 & 0 \\
0 & \beta^* & -\alpha^* & H & -i\sqrt{2}\beta^* & -\frac{i\alpha^*}{\sqrt{2}} & 0 & 0 & 0 & V(x) & 0 & 0 \\
-\frac{i\alpha^*}{\sqrt{2}} & -\frac{iD}{\sqrt{2}} & i\frac{\sqrt{3}}{\sqrt{2}}\alpha & i\sqrt{2}\beta & S & 0 & 0 & 0 & 0 & 0 & V(x) & 0 \\
i\sqrt{2}\beta^* & -i\frac{\sqrt{3}}{\sqrt{2}}\alpha^* & -\frac{iD}{\sqrt{2}} & \frac{i\alpha}{\sqrt{2}} & 0 & S & 0 & 0 & 0 & 0 & 0 & V(x) \\
V(x) & 0 & 0 & 0 & 0 & 0 & E_d+i\Gamma_d & 0 & 0 & 0 & 0 & 0 \\
0 & V(x) & 0 & 0 & 0 & 0 & 0 & E_d+i\Gamma_d & 0 & 0 & 0 & 0 \\
0 & 0 & V(x) & 0 & 0 & 0 & 0 & 0 & E_d+i\Gamma_d & 0 & 0 & 0 \\
0 & 0 & 0 & V(x) & 0 & 0 & 0 & 0 & 0 & E_d+i\Gamma_d & 0 & 0 \\
0 & 0 & 0 & 0 & V(x) & 0 & 0 & 0 & 0 & 0 & E_d+so\Gamma_d & 0 \\
0 & 0 & 0 & 0 & 0 & V(x) & 0 & 0 & 0 & 0 & 0 & E_d+so\Gamma_d
\end{bmatrix} \tag{2.7}$$

where

$$H = -\frac{\hbar^2}{2m_0}\left[(k_x^2+k_y^2)(\gamma_1+\gamma_2)+k_z^2(\gamma_1-2\gamma_2)\right] \tag{2.8a}$$

$$L = -\frac{\hbar^2}{2m_0}\left[(k_x^2+k_y^2)(\gamma_1-\gamma_2)+k_z^2(\gamma_1+2\gamma_2)\right] \tag{2.8b}$$

$$\alpha = \sqrt{3}\frac{\hbar^2}{m_0}\left[k_x(k_x-ik_y)\gamma_3\right] \tag{2.8c}$$

$$\beta = \frac{\sqrt{3}}{2}\frac{\hbar^2}{m_0}\left[(k_x^2-k_y^2)\gamma_2-2ik_xk_y\gamma_3\right] \tag{2.8d}$$

$$D = L - H \tag{2.8e}$$

$$S = \frac{1}{2}(L+H) - \triangle_0 \tag{2.8f}$$

and, $\gamma_1$, $\gamma_2$ and $\gamma_3$ are the Luttinger parameters of the host semiconductor and $\triangle_0$ is the spin orbit splitting energy of the host semiconductor. Diagonalization of the matrix yields the dispersion relations for the $E_-$ and and $E_+$ bands for each of the original valence bands. Again, V can be simplified to $C_{MD}x^{1/2}$ as for the conduction band. $C_{MD}x^{1/2}$ is the empirically determined coupling parameter. Fig.2.6 shows the VBAC fitting for the band gap change of $GaN_xAs_{1-x}$ with

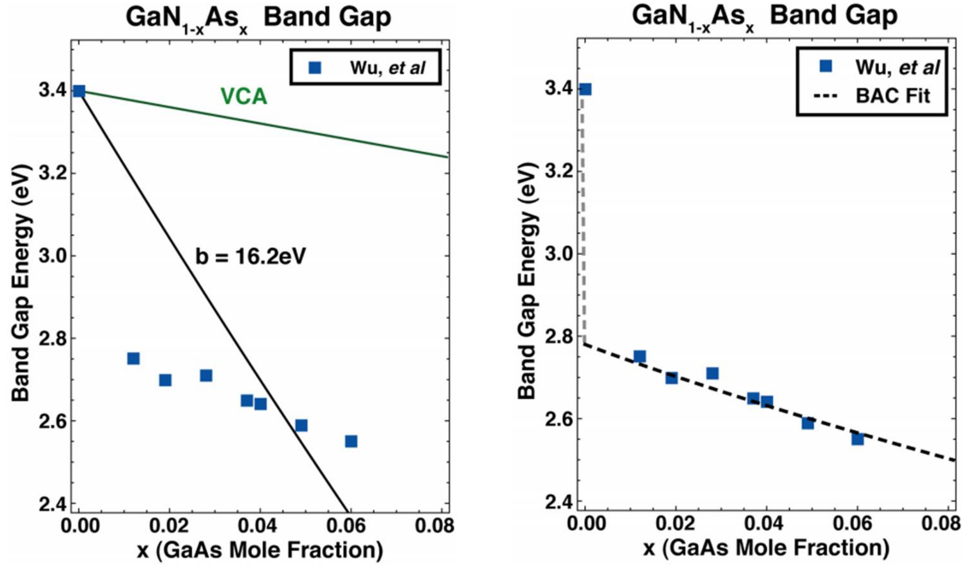


Figure 2.6: Measured bandgap of $GaN_{1-x}As_x$ as a function of x and its comparison with a) VCA [12] and b) VBAC model [41]

$C_{MAs} = 1.60eV$ and $E_{As} = 0.62eV$. The fit shows a good agreement with the experimental data and provides a physical explanation for the discontinuous band gap change in $GaN_xAs_{1-x}$[41].

### 2.4.2 Growth of $GaN_xAs_{1-x}$

Before Weyers et al. [43] introduced $GaN_xAs_{1-x}$ with x up to 0.016, the common belief was that it is not possible to grow $GaN_xAs_{1-x}$ alloy due to the miscibility gap. Then, first-principles total-energy calculations by Zhang et al. [44] showed that the maximum N composition x would be about 0.04 at the low temperature of $650°C$, which is in agreement with the experiments at that temperature. However, special techniques are necessary to grow $GaN_xAs_{1-x}$ alloys at lower temperatures to reach higher N compositions. $GaN_xAs_{1-x}$ alloys at the N-rich end of the phase diagram have been grown by metal-organic vapor phase epitaxy (MOVPE) and by molecular beam epitaxy (MBE)[45]. For both

techniques, it is difficult to obtain a high concentration of As in the alloy before phase separation occurs. The highest reported As content in the MOVPE grown layers is $x \sim 0.067$ [39, 37, 4]. Even lower maximum As contents of $x \sim 0.0026$ [46] and $x \sim 0.01$ [47] were achieved in MBE layers grown at $750°C$ and $500°C$, respectively.

Recently, materials with constituents having drastically different chemical or physical properties at compositions or structures far exceeding their thermodynamic solubility and stability limits have been synthesized using extreme non-equilibrium synthesis techniques [48, 49, 50]. The atomic diffusion length in these non-equilibrium processes is long enough to form crystalline lattices with uniform compositions, but short enough to avoid equilibrium phase segregation. Similarly, low-temperature molecular beam epitaxy LT-MBE has been employed to overcome the miscibility gap in the $GaN_xAs_{1-x}$ alloy system, allowing the synthesis of thin films of $GaN_xAs_{1-x}$ alloys over the whole composition range [1]. Yu at al. reported that the $GaN_xAs_{1-x}$ alloys are amorphous in the composition range of $0.17 < x < 0.75$ and crystalline outside this region. Also, amorphous films have smooth morphology, homogeneous composition, and sharp, well defined optical absorption edges. Fig.2.7 shows the optical gaps measured by optical absorption spectroscopy for a series of crystalline and amorphous $GaN_xAs_{1-x}$ films over the entire composition range.

Our aim is to understand and model the amorphous $GaN_xAs_{1-x}$ alloys from the band gap engineering point of view for energy-related semiconductor devices. The band structure modeling of amorphous semiconductor materials will be presented in the next section.

## 2.5 Amorphous semiconductor materials

Amorphous semiconductors possess a number of remarkable electronic properties, making them ideally suited for a wide range of large area electron device applications. Many properties of these materials are very different from those of crystalline materials. Some of their properties are different even from one sample to another of the same material.

An ideal crystal is defined as an atomic arrangement that has infinite translational symmetry in all the three dimensions, whereas such a well-defined definition is not possible for an ideal amorphous solid (a-solid). Although an a-solid is usually defined as one that does not maintain long-range translational symmetry or has only short-range order, it does not have the same precision in its definition, because long- or short-range order is not precisely defined. One can distinguish two general types of amorphous solids:

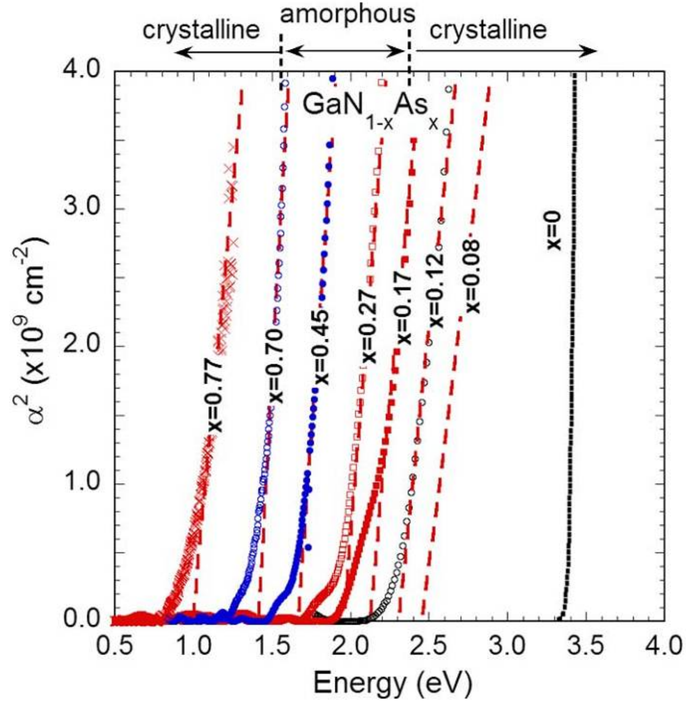


Figure 2.7: The energy dependence of the square of the absorption coefficient $\alpha^2$ for $GaN_xAs_{1-x}$ layers grown by Yu et al. [1] at different temperatures from $\sim 100$ to $\sim 600°C$.

- Solids composed of one type of atom (or a very small number of atom types) which locally see the same environment throughout the solid, just like in simple crystals. The local environment cannot be identical for all atoms (this would produce a crystal), so it exhibits small deviations from site to site, which are enough to destroy the long-range order. Amorphous semiconductors and insulators (such as Si, Ge, $SiO_2$), chalcogenide glasses (such as $As_2S_3$,$As_2Se_3$), and amorphous metals are some examples.

- Solids composed of many different types of atoms have complicated patterns of bonding. The class of structures based on long polymeric chains, that we refer to as plastics, is a familiar example [51].

A real crystal does not have infinitely long translational symmetry because of its finite size, which means that a crystal has surface atoms that break the translational symmetry. In addition to surface atoms in amorphous materials, however, there are also present other structural disorders due to different bond lengths, bond angles and coordination numbers at individual atomic sites. This is a consequence of extreme topological and/or chemical disorder present in an

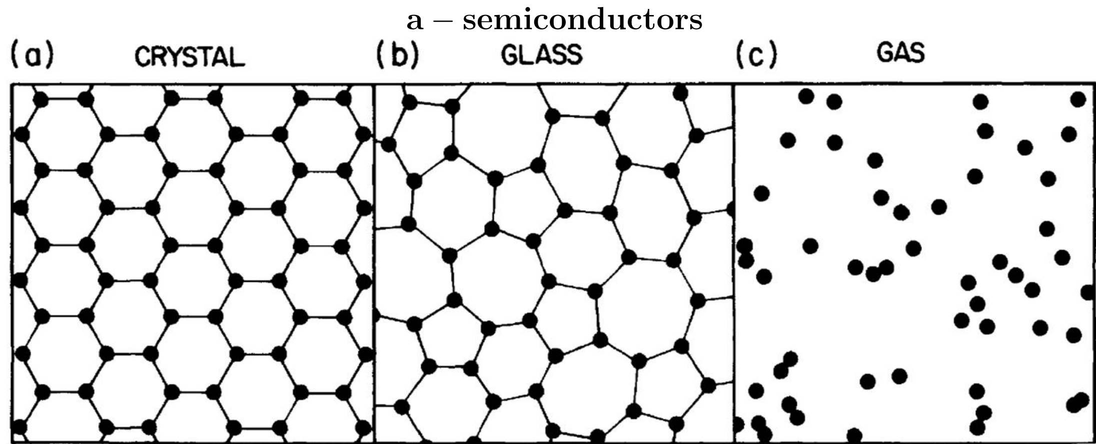


Figure 2.8: Schematic sketches of the atomic arrangements in (a) a crystalline solid, (b) an amorphous solid, and (c) a gas.

amorphous solid. In an elemental solid, defect can be categorized into two types: coordination defects and strain defect. The term coordination defect is used for those atoms that have a coordination number (number of neighbors) different than "8-N" rule [52]. Electronically, coordination defects create mid-optical-gap states and these states are highly localized in space. The term strain defect designates badly strained sites. In a-semiconductors, lattice sites usually maintain fourfold bonding but the bond angles and bond lengths (strongly) deviate from the crystalline structure [53].

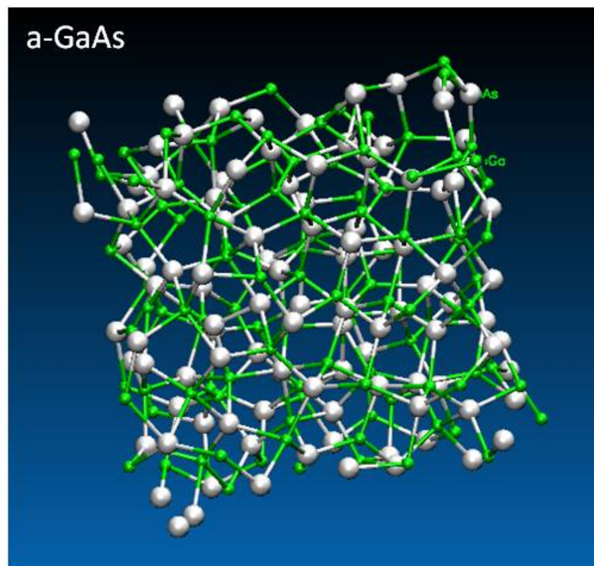


Figure 2.9: A typical amorphous structure of 216-atom model of a-GaAs.

The lack of any long-range order in disordered structures implies that we cannot use the concept of reciprocal-space vectors, and consequently one cannot expect any sharp features in $\rho(\epsilon)$. Indeed, the density of states (DOS) of

amorphous solids whose local structure resembles a crystalline solid has similar overall behavior to the crystalline DOS but with the sharp features smoothed out. This statement applies also to the band edges, i.e. the top of the valence band (corresponding to the bonding states) and the bottom of the conduction band (corresponding to the antibonding states). The fact that there exist regions in the amorphous DOS which can be identified with the valence and conduction bands of the crystalline DOS, is in itself quite remarkable. It is a consequence of the close similarity between the amorphous and crystalline structures at the local level (the nature of local bonding is very similar), which gives rise to similar manifolds of bonding and antibonding states in the two structures.

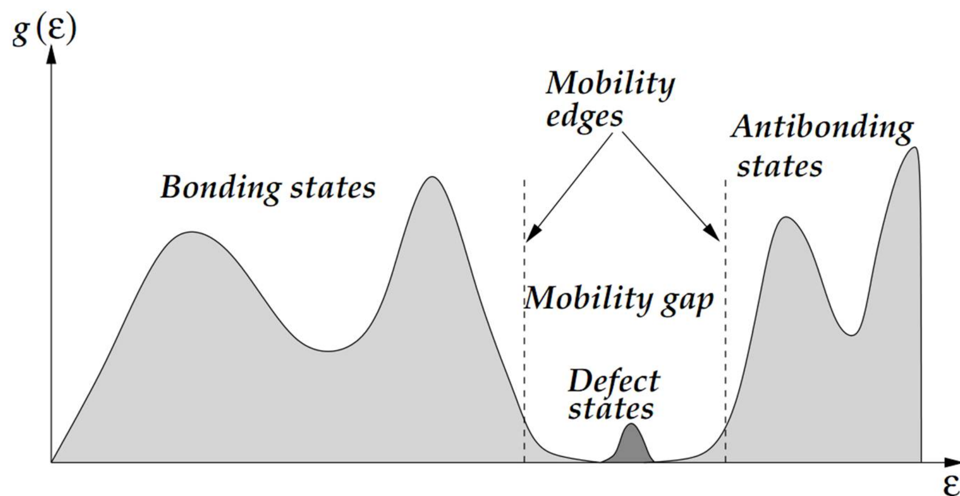


Figure 2.10: Schematic representation of the density of states g(E) as a function of the energy E of an amorphous semiconductor [51].

In the amorphous system, there is a range of energies where the DOS is very small, almost negligible compared with the DOS in the bonding and antibonding regions. Moreover, the DOS on either side of this region decays smoothly. The presence of strained and weak bonds gives rise in a-semiconductors to what are called band tail states. Interestingly, the states within this range of very small DOS tend to be localized, while states well within the bonding and antibonding manifolds are extended. Accordingly, the values of the energy that separate the extended states in the bonding and antibonding regions from the localized states are referred to as mobility edges; the energy range between these values is referred to as the mobility gap.

Usually many of the localized states in the mobility gap (especially those far from the mobility edges, near the middle of the gap) are related to defects, such as the dangling bond and floating bond. In this case, it is easy to understand the origin of localization, since these defect-related states do not have large overlap with states in neighboring sites, and therefore cannot couple to wavefunctions

extending throughout the system.

There is, however, a different type of disorder-related localization of electronic wavefunctions, called Anderson localization, which does not depend on the presence of defects. This type of localization applies to states in the mobility gap of amorphous semiconductors which are close to the mobility edges. The theoretical explanation of this type of localization, first proposed by P. W. Anderson [51], was one of the major achievements of modern condensed matter theory (it was recognized by the 1977 Nobel prize for Physics, together with N.F. Mott and J. H. van Vleck). The basic model consists of a set of electronic states with energies $\epsilon_i$ which take values within an interval W. The values of the electronic states correspond to a random distribution in the interval W for a disordered structure. If the system had long-range order and all the individual states had the same energy, the corresponding band structure would produce a band width B. Anderson argued that if $W > \kappa B$, then the electronic wavefunctions in the disordered system will be localized (where $\kappa$ is an unspecified numerical constant of order unity). In the ordered case, the crystalline wavefunctions are delocalized since they have equal weight in any unit cell of the system due to the periodicity.

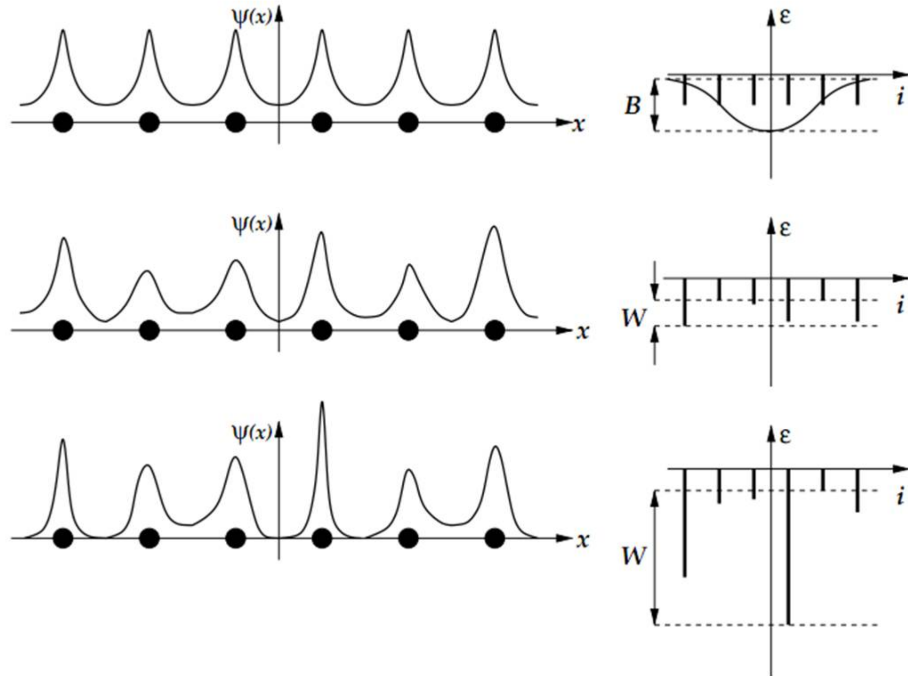


Figure 2.11: Schematic representation of Anderson localization in a one-dimensional periodic system of atoms.

In the Fig.2.11 left panels show the atomic positions (indicated by the filled circles) and electronic wavefunctions $\psi(x)$. The right panels show the distribution of electronic energies $\epsilon$ associated with the different sites labeled by the index i . Top: delocalized wavefunctions, which arise from identical energies at each atomic

site and a band structure of width B. Center: delocalized wavefunctions, which arise from random on-site energies distributed over a range $W \leq B$. Bottom: localized wavefunctions, which arise from random on-site energies distributed over a range $W >> B$ [51].

## 2.6 Summary

In the first part of this chapter, a brief summary of the alloying semiconductors and band gap engineering was presented. This part provides a necessary theoretical background to calculate the band-gap energy variation with temperature and alloying for conventional compound semiconductors. We then introduced highly mismatched alloys and their novel properties. Finally, we present the history of $GaN_xAs_{1-x}$ alloys, covering the required theoretical model to describe its band gap variation with alloying. In addition, basics definitions such as band tailing or mobility band gap are provided for amorphous semiconductors.

# CHAPTER 3

# COMPUTER SIMULATION METHODS

## 3.1 Introduction

Computer simulation methods are the development of an idealized model of a physical system of interest. The results of a computer simulation can serve as a bridge between laboratory experiments and theoretical calculations. In some cases one can obtain essentially exact results by simulating an idealized model that has no laboratory counterpart. The results of the idealized model can serve as a stimulus to the development of the theory [54].

Fig.3.1 illustrates the regime of accessible lenght- and time-scales for different types of simulations. As seen in Fig.3.1 hierarchical multiscale modeling uses separate simulations to compute structure-property relations at one length scale in order to pass the "effect" to higher length scales [55, 56, 57, 58]. At the smallest scale quantum mechanics (*ab initio* calculations) can be used, with relevant lengths of angstroms and time scales of $10^{-15}$ s, while at the largest scale continuum mechanics is stated, relevant lengths can exceed meters and the times can approach years. In principle, all properties of all materials and phenomena are describable by quantum mechanics (QM) (Schrodinger's equation), unfortunately direct use of QM is impractical for solving applications that involve a large number of atoms ($>\sim 1K$). Classical and quantum-based, adiabatic and non-adiabatic approximations to Schrodinger's equation lead to simplified equations of motion (molecular mechanics/dynamics - MM/MD) that are applicable to much larger systems while still retaining the atomistic and electronic degrees of resolution ($\sim$ millions of atoms and electrons). Further, classical approximations on these systems include coarse-grain models based on rigid-bodies of constrained particles, suitable, for example, in sampling the dihedral conformational space of large-scale molecular systems, Monte Carlo techniques, averaging and homogenization techniques to explore larger and longer length- and time-scales, close to or within the mesoscale regime. At the higher-end of the length- and time-scales, phenomenological-based continuum-level methods [including finite elements] are the norm, yet these are incapable of capturing fundamental nanoscale properties and phenomena that are critical for understanding, elucidating and optimizing

the behavior of matter at the macroscale.

In this chapter, we provide a brief description of computational methods that we used throughout this dissertation. This chapter consist of five sections; first three sections summarize the Molecular Dynamics simulations (classical and *ab initio*) and Continuous Random Network, fourth section present some basic definition required for topology analysis of the structure, and last section introduces the electronic density of states and inverse participation ratio.

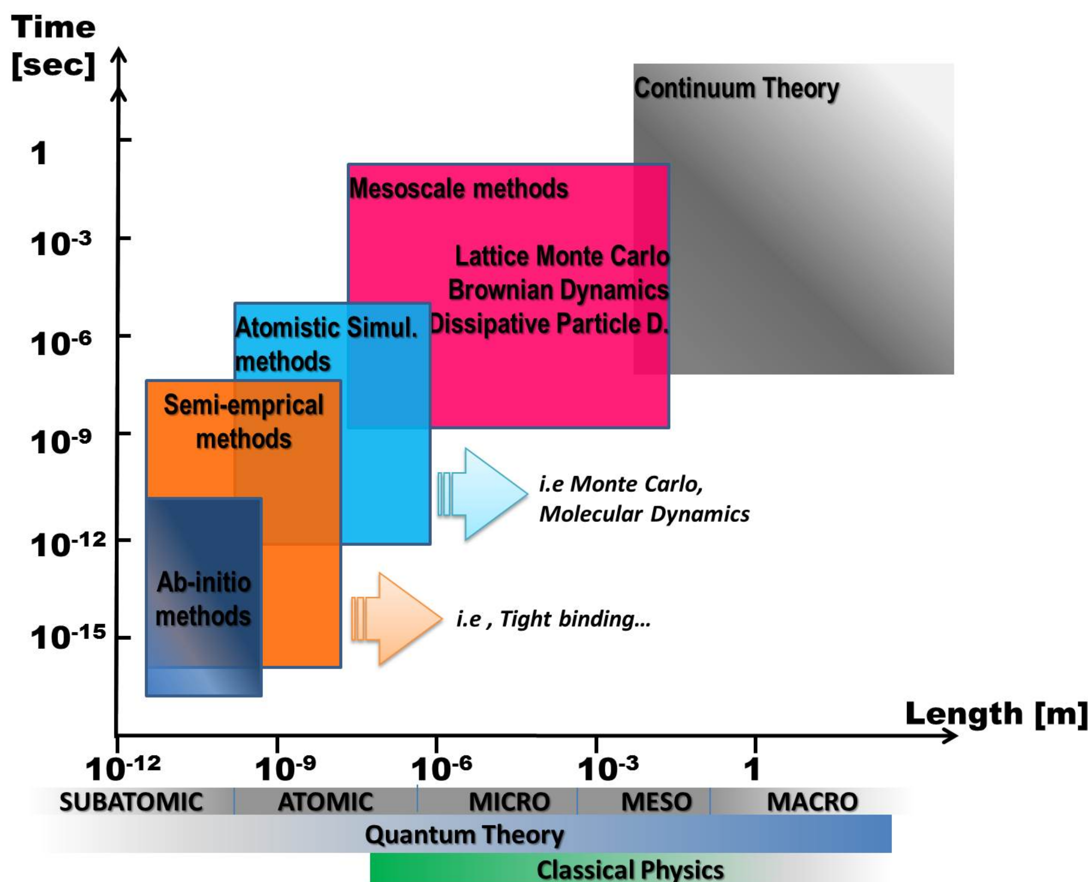


Figure 3.1: Schematic of the hierarchical multiscale modeling.

There is no distinct lines to sort out simulations method according to length and time scale in multiscale modelling. For example, Monte Carlo lattice methods can be applied at the femto-scale, angstrom-scale or even at the micrometer-scale according to desired properties. Thus, it is important to decide computer simulation method according to related phenomena and properties which are the primarily interest of research topic. Considering these points molecular dynamics (MD) simulations and *ab initio* calculations are chosen for our calculations. The molecular dynamics method was first introduced by Alder and Wainwright in the late 1950's [59] to study the interactions of hard spheres. Many important insights concerning the behavior of simple liquids emerged from their studies. The next

major advance was in 1964, when Rahman carried out the first simulation using a realistic potential for liquid argon [60]. The first molecular dynamics simulation of a realistic system was done by Rahman and Stillinger in their simulation of liquid water in 1974 [61].

## 3.2 Classical Molecular Dynamics

Classical molecular dynamics (MD) simulations are based on predefined potentials (force fields) either based on empirical data or on independent electronic structure calculations. It has been extensively used to predict the motions of particles with time for a large number of phenomena such as amorphous materials, defect in solids, phase transitions, liquid structures, fracture, friction, polyelectrolyte, biomolecules, clusters or surfaces. The main aim is to define macroscopic behavior of the system from microscopic interactions. In principle the future velocities and accelerations of many thousands of atoms, interacting via a predefined classical force field, can be computed from the Newton's equations of motion.

Consider a system of N atoms in volume V. The equation of the motion of atoms can be solved as

$$m_i \frac{d^2 \overrightarrow{r_i}}{dt^2} = \overrightarrow{F_i} = -\nabla_i U, \; i = 1, 2, ....., N \tag{3.1}$$

where $m_i$ and $\overrightarrow{r_i}$ are the mass and position of $i^{th}$ atom, respectively, and $\overrightarrow{F_i}$ is the force acting on this particle. The equation of motion which is in vector form represents a set of 3N coupled second order differential equations which are solved numerically to obtain the positions and momenta of the particles. Force can be obtained by summing the forces acting on particle $i$ from all other particles $j$ in the system. Thus, it can be written as,

$$\overrightarrow{F_i} = \sum_{j \neq i}^{N} f_{ij} \tag{3.2}$$

where $f_{ij}$ is the force between two particles $i$ and $j$.

The general scheme of the classical molecular dynamics is presented in Fig.3.2. After obtaining forces and set of equations, the next step is to integrate them. Verlet algorithm [62, 63] is one of the integration schemes that can be used to solve future velocities of the particle. These algorithms are based on Taylor series expansions and the resulting finite difference forms. The positions of the particles at time $t + \Delta t$ are obtained using:

$$\overrightarrow{r}_i(t + \Delta t) = \overrightarrow{r}_i(t) + \overrightarrow{v}_i(t)\Delta t + \frac{\overrightarrow{f}_i(t)}{2m_i}(\Delta t)^2, \tag{3.3}$$

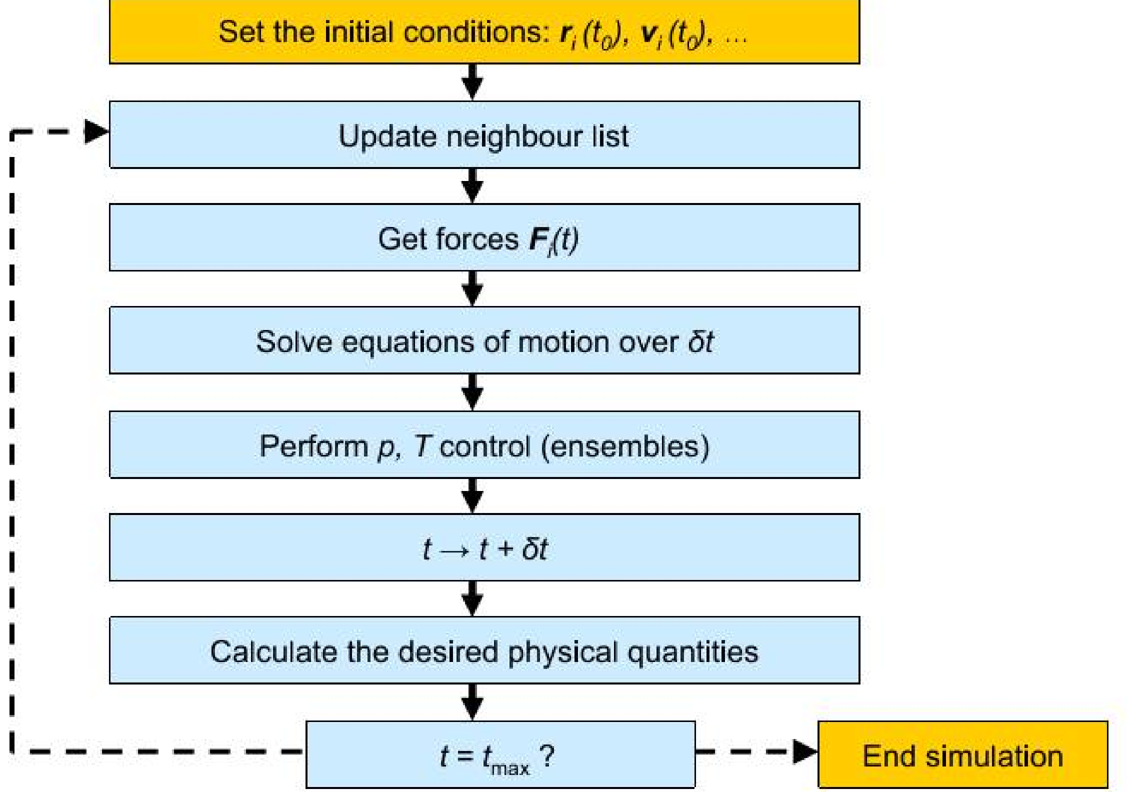


Figure 3.2: General flow chart for classical MD simulations.

and,

$$\vec{v}_i(t + \Delta t) = \vec{v}_i(t) + \frac{\vec{f}_i(t + \Delta t) + \vec{f}_i(t)}{2m_i}\Delta t. \tag{3.4}$$

Thermodynamic quantities has to be controlled by choosing an appropriate statical ensemble for the system. In the canonical ensemble (NVT) the number of atoms (N), the volume of the space (V), and the average kinetic energy (T) are kept constant. Thus, the system trajectory was achieved consistent with the canonical ensemble. There are also different thermostat methods available to add and remove energy from the boundaries of an MD system in a realistic way, approximating the canonical ensemble. Berendsen thermostat [64] , Anderson thermostat [65] , Langevin (stochastic) thermostat, and Nose-Hoover thermostat [66, 67] are the commonly used techniques to control temperature of the system. The main aim of a thermostat is to ensure that the average temperature of a system be the desired one. We have worked with canonical ensemble (NVT) coupled to Nose-Hoover thermostat during modeling of $GaN_{1-x}As_x$ alloys.

The thermal interaction between the heat reservoir and the system results in exchange of the kinetic energy between them. Instantaneous temperature (T)

can be calculated from the velocities of the particles at any time t as:

$$3(N-1)k_BT = \sum_{i=1}^{N} m_i|\overrightarrow{\upsilon}_i|^2, \tag{3.5}$$

where (N-1) factor is for momentum conservation and $k_B$ is the Boltzmann constant.

The simulation must first undergo an equilibration phase before thermal equilibrium is reached. During equilibration, there is a significant drift in the macroscopic observable of the system such as the total kinetic energy or pressure. By monitoring these observables as a function of time one can determine when equilibrium has been reached. After equilibration, the macroscopic observables will fluctuate around their equilibrium values. At this point one usually begins to calculate variables of interest (such as pressure or energy) for the accumulation of time averages. The simulation is continues until the statistical error in the averages becomes small.

### Quenching from the melt

Quenching from the melt is usually known as the melt-and-quench approach [68] in the literature. Since 1985, Car-Parrinello molecular dynamics [69] and quenching from the melt of periodically-continued supercells have been extensively used to generate amorphous structures of covalent semiconductors. This method successfully applied to silica [70] and some chalcogenide glasses [71, 72, 73]. As presented by Drabold [68] quenching from the melt method should work when;

- the structure of the liquid is essentially similar to the structure of the glass, and
- the ordering is quite local.

Disadvantage of the quenching from the melt is the difference between time scales of real the experiment and simulation. Although, the typical experimental cooling rates changes from $10^{-2}$ to $10^{3}$ K $s^{-1}$, it is in the order of $10^{12}$ to $10^{15}$ K $s^{-1}$ in MD simulations [74]. Such high cooling rates introduces large number of defects, which are not observed in real experiments, into the structure [75, 76]. In addition, it is also very important to keep strain as low as possible for a realistic simulation of amorphous structure. Higher bond length and angle distribution increases the strain and causes poor electronic properties.

## 3.3 *Ab initio* Molecular Dynamics

### 3.3.1 Interaction Potentials and Forces

Force model used to describe the atomistic interactions analytically is the hearth of any molecular dynamic simulations. Force models are also the computationally most intensive parts of a molecular dynamics simulation code, taking up to 95% of the total simulation time. Regardless of the merits of the other algorithms in the simulation code (integrators, pressure and temperature controls etc.), whether or not your simulation produces realistic results depends ultimately on the force model. In turn, the local environment (coordination, bond lengths, bond angles, the environment of the neighboring atoms and so on) created from chosen force field will define the electronic and structural properties of the material. Besides, it is not easy to compute forces on the atoms in the amorphous structure especially because of the varying bond lengths and angles. The complexity of interatomic potentials also grows rapidly with the number of distinct atomic species even for binary systems, and there are very few reliable empirical potentials available.

The usual approach for developing a potential is to determine a functional form motivated by physical intuition and then to adjust the parameters either to *ab initio* data and/or some physical properties to come up with an empirical potential. Although, such empirical potentials provide a simple and physically interpretable description for the interatomic interactions, their applicability is limited to the type of data to which it was fitted. Once fitted, there is no easy way to improve upon it, without refitting the data. A solution to this problem is to model the system using *ab initio* electronic structure calculations by solving Schrödinger's equation, to compute the potential energy and forces from the first principles. Such a technique can provide very accurate description of the interatomic interactions, but are computationally very extensive and hence limited only to small systems involving only a few atoms.

### 3.3.2 Density Functional Theory

Hohenberg and Kohn [77] reported in 1964 the modern formulation of density functional theory in which all properties of a quantum many-body system are considered as a function of the ground state density of particles. In the Kohn and Sham approach [78], the energy calculation in inhomogeneous electron systems with the complex problem relies on a comparison of functionals describing interacting and non-interacting electrons in the effective potential. The difference between the full ground-state energy obtained from the correct many-body wave function and the one obtained from the Hartree-Fock or Kohn-Sham Slater

determinant is represented by the functional of charge density called exchange-correlation energy ($E_{xc}[n(r)]$). This approach results in formulation of the set of equations, known as Kohn-Sham (KS) equations. The simplest approximation to $E_{xc}[n(r)]$ is the local density approximation (LDA). It assumes that $E_{xc}[n(r)]$ is simply an integral over all space with the exchange-correlation energy density at each point assumed to be the same as in a homogeneous electron gas with that density. The LDA is generally very successful in predicting atomic structures and some of its properties, but its limitations are very obvious in some cases. For example, the band gaps in semiconductors and insulators are systematically underestimated and the cohesive energies are significantly overestimated by LDA. In order to overcome these limitations, the generalized gradient approximations(GGA) have been introduced by considering the dependence of exchange-correlation function on the local variations of the electron density. In the GGA, there is an explicit dependence of the $E_{xc}[n(r)]$ on the gradient of the electron density. In order to reduce the problem of finding the total energy of an infinite system with an infinite number of electrons to that of the problem with a finite number of electrons moving in the periodic potential, the periodic cell approximation is used. The Bloch's theorem allows the expansion of electronic wave function at each k-point in the Brillouin zone as a series of plane waves. To expedite the computation, this expansion usually includes only the plane waves with a kinetic energy less than a certain cutoff energy. The KS equations are solved self-consistently for the ground state of the non-interacting electrons in effective potentials [79]. Only outer-shell electrons are considered while core electrons are replaced with pseudo-potential. Special k-point sampling scheme proposed by Monkhorst and Pack [80], symmetry considerations and the electron smearing methods allow to reduce the number of k-points in the Brillouin zone considerably. Ultrasoft Vanderbilt pseudopotentials [81] result in a smaller set of the plane waves needed for the accurate representation of the electronic wavefunctions. The atoms in the supercell are fully relaxed using conjugate gradient or quasi-Newton algorithm until all residual forces on the atoms become sufficiently small [82].

Briefly, the density functional theory (DFT) is one of the most widely used method for *ab initio* calculations of the structure of atoms, molecules, crystals, surfaces, and their interactions. The main idea of DFT is to describe an interacting system of fermions via its density and not via its many-body wave function and this approach gives a description of ground state properties of metals, semiconductors, and insulators.

## 3.4 Continuous Random Network (CRN)

Continuous random network (CRN) model introduced more than 60 years ago by Zachariasen [83]. Many properties of disordered materials can be understood by looking at idealized structural models, in which the strain is as small as possible in the absence of long-range order. Continuous random network is an idealized structural model for covalent amorphous semiconductors and glasses. Contrary to perfect crystals, however, CRNs exist with widely varying quality, and optimizing their overall properties has been a central goal for the theorists studying covalent amorphous materials. In this model, each atom is placed in a crystal-like local environment, with perfect coordination and chemical ordering, yet longer-range order is nonexistent. Defects, such as missing or added bonds, or chemical mismatches, however, are not accounted for this basic model.

Even though it is easy to assemble a generic CRN, it is much more difficult to create a network that minimizes the strain and yet satisfies fully the basic constraints of coordination. This network represents the ideal state for elemental amorphous semiconductors. Experimentally, this state is not uniquely defined and depends strongly on the method of preparation as well as on the annealing history. However, well annealed samples are thought to be represented by low-strain CRNs.

After Zachariasen, Bell and Dean achieved in an hand-built model for CRN [84]. Soon after, the first hand-built model of elemental amorphous semiconductor was assembled by Polk [85]. Starting with a random core of a few atom, Polk proceeded to add further atom so that all bonds at the surface is satisfied. Following this simple algorithm, Polk assembled 440 units and measured, the position of each atom by hand. The radial distribution function of the model turned out to be in reasonable agreement with the experimental data.

These models had open boundary conditions and a limited size. The resulting large number of surface atoms made them unsuited for studying bulk properties. Henderson managed to build by hand a network of 61 atoms with periodic boundary conditions [86]; clearly, the future was for computer generated structures. It took another decade before Wooten, Winer and Weaire (WWW) introduced a well-defined and scalable numerical procedure for preparing CRNs with periodic boundary conditions [87]. The WWW algorithm remains to this day the basic approach for generating high-quality CRNs.

### 3.4.1 WWW algorithm to build a CRN

In the approach of WWW, a configuration consists of the coordinates of N atoms and a list of the 2N bonds between them. The structural evolution consists

of a sequence of bond transpositions as illustrated in Fig.3.3: In a chain of four bonded atoms, ABCD, the two bonds AB and CD are replaced by two other bonds AC and BD, leading to a chain ACBD after the bond transposition. The generation of a CRN starts with a cubic diamond structure which is randomized by a large number of such bond transpositions.

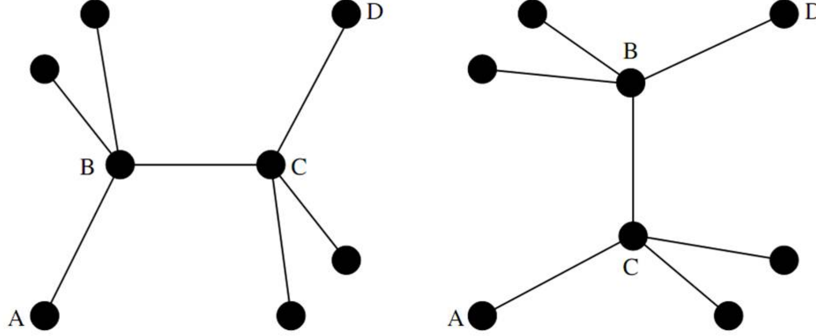


Figure 3.3: Diagram depicting the WWW bond transposition.

After randomization, the network is relaxed through a sequence of bond transpositions, accepted with the Metropolis acceptance probability [88]:

$$P = min[1, exp(\frac{E_b - E_f}{k_B T})] \tag{3.6}$$

where $k_B$ is the Boltzmann constant, T is the temperature, and $E_b$ and $E_f$ are the total quenched energies of the system before and after the proposed bond transposition.

The list of neighbors determines the topology, but also the energy of the network: independently of the distance between two atoms, they interact only if they are connected in the list of neighbors. With an explicit list of neighbors, it is possible to use a simple interaction such as the Keating potential: [89]

$$E = \frac{3}{16}\frac{\alpha}{d^2} \sum_{<ij>} (\mathbf{r}_{ij} \cdot \mathbf{r}_{ij} - d^2)^2 + \frac{3}{8}\frac{\beta}{d^2} \sum_{<jik>} (\mathbf{r}_{ij} \cdot \mathbf{r}_{ik} + \frac{1}{3} d^2)^2, \tag{3.7}$$

where $\alpha$ and $\beta$ are the bond-stretching and bond-bending force constants. With the approach described above Wooten and Weaire obtained 216-atom structures with an angular distribution as low as 10.9°. A decade later, using the same approach but with more computing power, Djordjevic, Thorpe, and Wooten (DTW) produced some large (4096-atom) networks with a better quality, with a bond-angle distribution of 11.02° for configurations without four-membered rings and 10.51° with four-membered rings[90]. Mousseau and Barkema manage to produce 1000-atom and 4096-atom model by using a series of algorithmic improvements and faster computers with lower bond angle distributions [91]. Eventhough the

continuous random network model has been widely used and accepted as the basis for the structure of glasses and amorphous materials with no defects, this limit can be more and more closely approached for both vitreous silica and amorphous silicon with carefully prepared samples [92].

## 3.5 Structural Properties

### 3.5.1 Basic definitions

An 'ideal' amorphous semiconductor can be defined as a random network with no long range order but an excellent short range order. In the ideal amorphous semiconductor all atoms are covalently bonded according to their valency with strong bonds favored over weak bonds whenever possible. Hybridization of the valence electrons into $sp^3$ orbitals that lead to tetrahedral bonding (Fig 3.4-a). Two possible connectivities of tetrahedra: edge-sharing and corner-sharing configurations are presented in Fig 3.4-b and -c.

Nearest neighbor distance is the distance between two nearest neighbors in a structure (Fig. 3.4-d). For the tetrahedrally coordinated semiconductors, the number of nearest-neighbors is 4. The bond angles between nearest neighbor of an atom that has a regular tetrahedral structure are 109.45°(Fig 3.4-e). Coordination number, CN, is defined as the total number of nearest neighbors of a central atom in a molecule or ion as shown in (Fig 3.4-f). Covalently bonded materials follow, in general, the '8-N Rule' of structure. If N is the number of outer shell electrons, the coordination number is CN=(8-N). Experiment suggests that in amorphous semiconductors generally, as well as in tetrahedrally coordinated systems, the nearest neighbor coordination required by the generally accepted chemical valence, usually as specified by the 8-N rule, is mostly realized.

### 3.5.2 Radial Distribution Functions

In amorphous materials due to the lack of long range order. The determination of structure is very difficult. In spite of this, the atomic arrangement in amorphous material and the presence of short-range order can be illustrated by a one dimensional probability function, called radial distribution function (RDF). The RDFs are categorized into total RDF and partial-pair distribution function (PDF).

The RDF, $g(r)$, describes how the atomic density varies as a function of distance from one particular atom. Specifically, it is a measure of, on average, the probability of finding a particle at a distance away from a given reference particle, relative to that for an ideal gas. The general algorithm involves determining how many particles are within a distance of $r$ and $r + dr$ away from a particle.

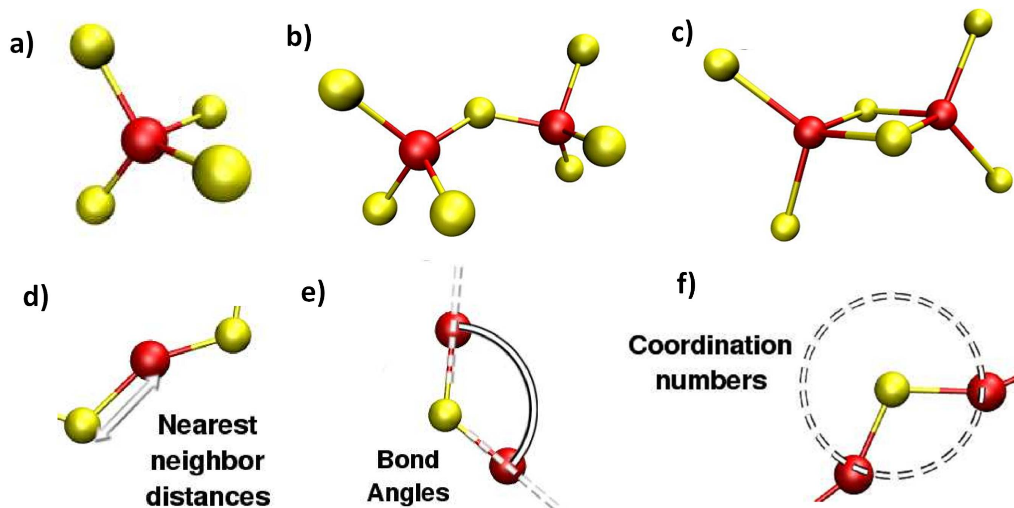


Figure 3.4: Illustration of several definition of structural properties: a) tetrahedral bonding, b) corner-sharing tetrahedra, c) edge-sharing tetrahedra, d) nearest neighbor distance, e) bond angle and f) coordination number.

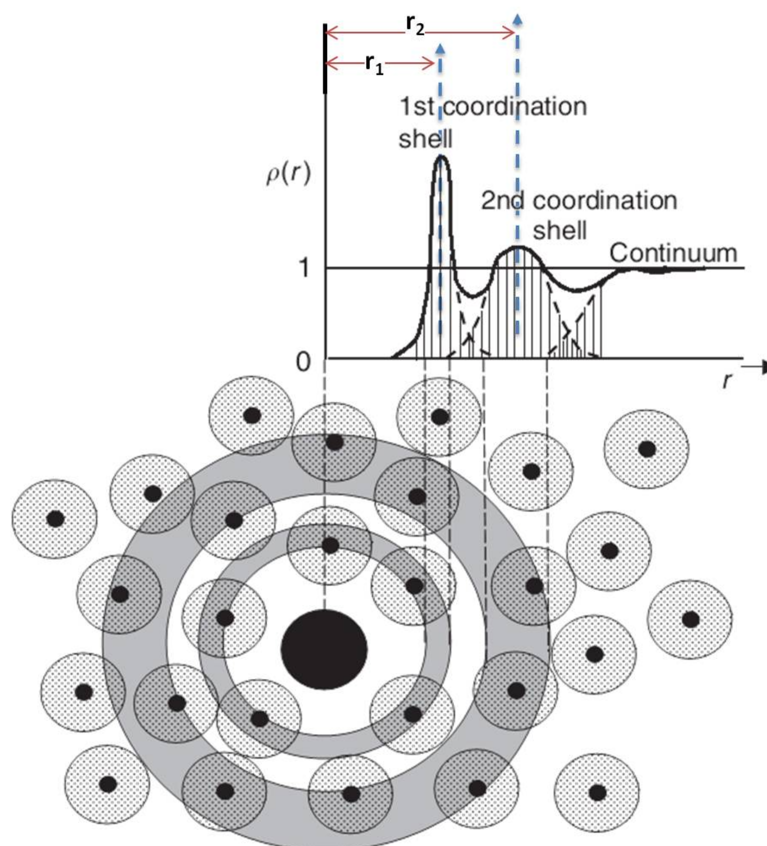


Figure 3.5: The density function $g(r)$ plotted as a function of r for an amorphous solid.

This general theme is depicted in the Fig.3.5, where the particle in the center is our reference. The average number of neighbors of a given atom up to

a distance R is given by

$$4\pi\rho_0 \int_0^R r^2 g(r) dr. \tag{3.8}$$

where $\rho_0$ is averaged number of density and $g(r)\rho_0$ gives the probability density that a particle is separated by a distance r from another one. Since interatomic distances can not be smaller than the atomic core diameters, we have $\lim_{r\to 0} g(r) = 0$. For very large separations, $g(r)$ approaches unity and the systems behaves as a structureless continuum, $\lim_{r\to\infty} g(r) = 1$.

As shown in Fig.3.5, $g(r)$ exhibits oscillatory behavior, due to the fact that the peaks of the probability function represent average interatomic separations. As a result of this, the RDF oscillates about the average density parabola given by the curve $4\pi r^2 \rho_0$. The position of the first peak in the RDF produces the average nearest-neighbor bond length $r_1$ and the position of second peak gives the next-nearest-neighbor distance $r_2$. The second peak is generally wider than the first for covalent a-solids, which can be attributed to a static variation in the bond angles $\theta$. If no bond-angle variation exist, then the width of the first two peaks should be equal.

The atomic structure of the crystalline GaAs (c-GaAs) and amorphous GaAs (a-GaAs) are depicted in Fig 3.6-a and -b for comparison, respectively. The RDF of c-GaAs consist of a series of sharp peaks located at the first nearest-neighbor distance, the second nearest-neighbor distance, and so forth Fig 3.6-c. In contrast, for a-GaAs, the characteristic features are a number of peaks that become broader and less distinct with increasing r. The position of the first peak is an estimate for the average first-nearest neighbor distance $r_1$, the position of the second peak is an estimate for the average second-nearest neighbor distance $r_2$, and so forth.

In general, there will be a number of different atomic species in the system and it is then possible to define a partial pair correlation function, $g_{\alpha\beta}(r)$ for correlations between atoms of species $\alpha$ and $\beta$. In more detail, just by counting the numbers of atoms of kind $\beta$ that are a distance between $r$ and $r + dr$ from a fixed atom of kind $\alpha$, and a averaging over all atoms $\alpha$ gives the correlation function, $g_{\alpha\beta}(r)$, which can be written as

$$g_{\alpha\beta}(r) = \frac{1}{4\pi r^2 \rho N c_\alpha c_\beta} \sum_{i\neq j} \delta(r - r_{ij}) \tag{3.9}$$

where N is the total number of particles in the system; $\rho = N/V$ is the number density, $c_\alpha = N_\alpha/N$ and $c_\beta = N_\beta/N$ . $N_\alpha$ and $N_\beta$ are the number of $\alpha$ and $\beta$ particles, respectively.

Experimental determination of radial and partial-pair distribution functions are possible by diffraction experiments utilizing X-ray diffraction, electron

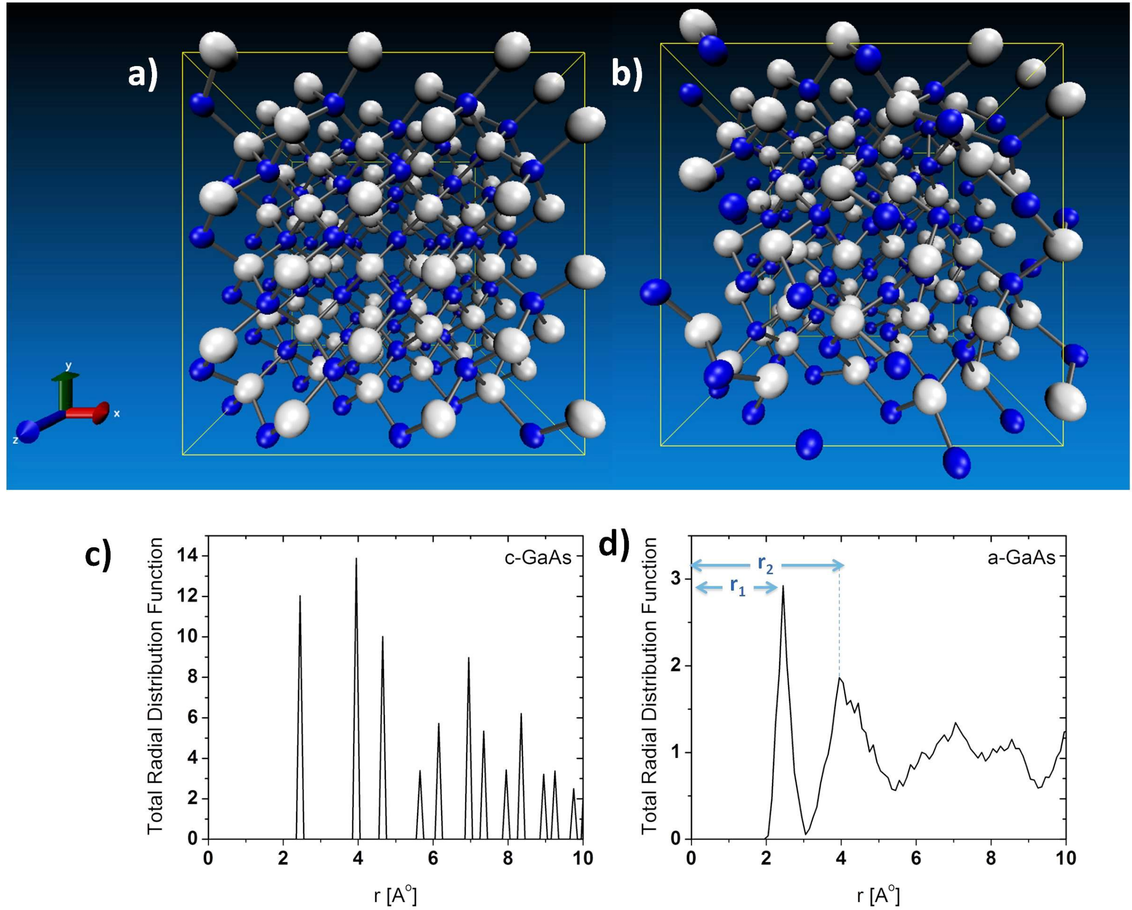


Figure 3.6: Atomic structure of a) crystalline GaAs (c-GaAs) and b) amorphous GaAs (a-GaAs). Blue (dark sphere) represents gallium and white (bright sphere) represents arsenic. Total Radial distribution function for c) c-GaAs and d) a-GaAs

diffraction or neutron diffraction, or combinations of it.

### 3.5.3 Ring Statistics

In random-network models of amorphous solids, ring statistics provide a measure of medium-range order [93]. Ring statistics are associated with viewing the material as being made up of a distribution of rings composed of nodes for the atoms and links for the bonds. The arrangements of the rings formed by the atoms can describe the topology of these systems. In many amorphous solids, ring statistics have become a generally accepted measure of medium range order. Basically a ring can be defined as a closed path.

One can use the total number of nodes of the ring for the numbering of rings, therefore a N-membered ring is a ring containing N nodes. Although ring can be defined as closed path, there are different definitions for counting the rings. Finding all rings in a system is computationally intensive because the ring

computation contains Hamiltonian cycle problem as a special case and there are possibly an exponential number of rings in the system. Considering all rings in the system is not practical for relatively large systems.

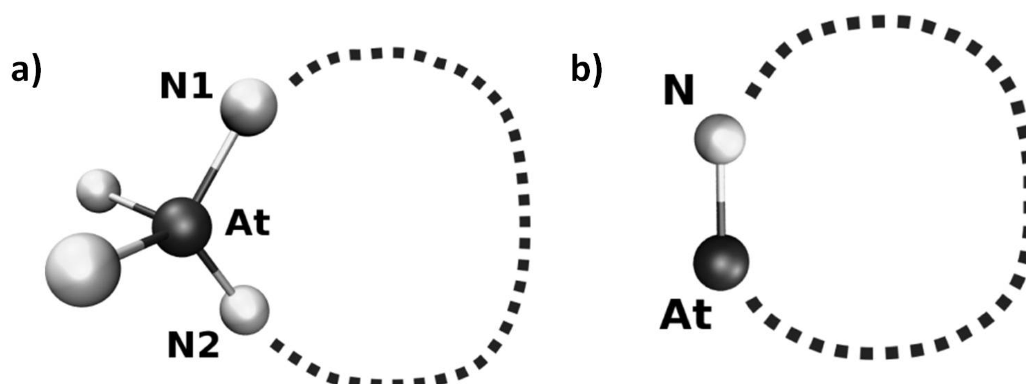


Figure 3.7: a) King's shortest path criterion in the ring statistics: a ring represents the shortest path between two of the nearest neighbors (N1 and N2) of a given node (At). b) Guttman's shortest path criterion in the ring statistics: a ring represents the shortest path which comes back to a given node (At) from one of its nearest neighbors (N) [94].

The first way to define a ring has been given by King [95] as the shortest path which comes back to a given node from one of its nearest neighbors. Using the Kings criterion, in some cases, shortest paths were ignored by the algorithm. With the shortest path criterion [96, 97], the algorithm has been modified and a ring represents the shortest path between two of the nearest neighbors of a given node. King's shortest path and Guttman's shortest path criterion are illustrated in Fig.3.7-a and -b, respectively.

In our case we use irreducible rings for ring statistics. A ring is primitive (or irreducible) if it can not be decomposed into two smaller rings [98, 99]. Fig.3.8 depicts the primitive ring analysis depending on the relations between the paths A, B, and C.

By analyzing Fig.3.8, primitive ring can be concluded as being depend on the relations between the paths A, B, and C:

- If paths A, B, and C have the same length: A = B = C then the rings 'AB', 'AC' and 'BC' are primitive rings.
- If the relation between the paths is like ? = ? < ? (ex: $A = B < C$) then one smaller ring ('AB') and two bigger rings ('AC' and 'BC') exist. None of these rings can be decomposed into the sum of two smaller rings therefore the three rings are again primitive rings.

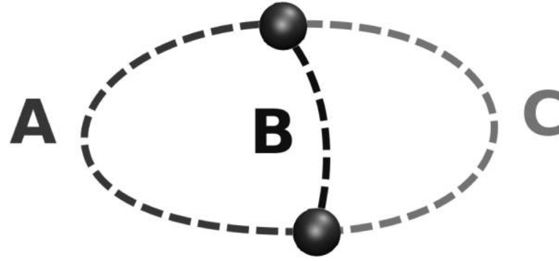


Figure 3.8: Primitive rings in the ring statistics: the AC ring defined by the sum of the A and the C paths is primitive only if there is no B path shorter than A and shorter than C which allows to decompose the AC ring into two smaller rings AB and AC [94].

- If the relation between the path is like $? < ? = ?$ (ex: $A < B = C$) or $? < ? < ?$ (ex: $A < B < C$) then a shortest path exists (A). It will be possible to decompose the ring ('BC') built without this shortest path into the sum of two smaller rings ('AB' and 'AC'), therefore this ring will not be a primitive ring

In the ideal tetrahedral structures, the smallest bond circuits of the covalent graph are six-membered rings with fourfold coordinated atoms. In crystalline wurtzite, the six-membered ring adopt two distinct configurations: one-quarter of them are in the chair configuration (Fig.3.9-a), the other three-quarters are in the boat configuration (Fig.3.9-b). However six-membered rings of the tetrahedral continuous random networks are not limited to these two specific geometries, instead it can have continuous spectrum of shapes. Beside, depending on the structure, all sized of n-rings can appear in the CRN. In addition to that, the presence of an odd-membered ring indicates wrong bonds (homonuclear bonds) in a tetrahedrally coordinated semiconductor alloys.

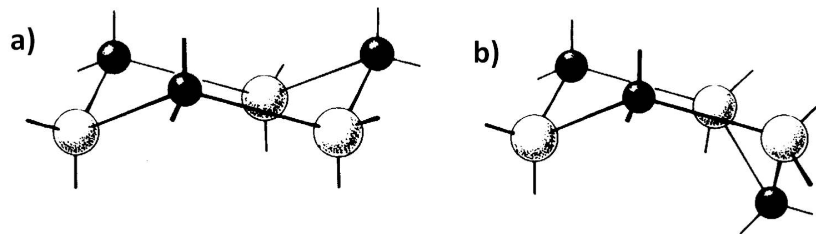


Figure 3.9: The a) chair and b) boat configurations of six-atom rings.

For ring statistic we have used "R.I.N.G.S" code. The details of calculations and code can be found in Le Roux et al.'s report [94]. In the literature either the number of Rings per node $R_N$ or the number of Rings per cell $R_C$ are presented as a result of the ring statistic analysis. $R_N$ can be calculated for one node by

counting all the rings corresponding to the property we are looking for (Kings, shortest path, primitive,etc). $R_C$ can be calculated by counting all the different rings corresponding at least once (at least for one node) to the property we are looking for (Kings, shortest path, primitive,etc.). In most simple cases the networks can be distinguished using only the number of rings. However the ring connectivity gives further information about the arrangement of atoms at a larger length scale, and enhances the understanding of the structure.

## 3.6 Electronic Properties

### 3.6.1 Electronic Density of State (EDOS) and Inverse Participation Ratio (IPR)

The density of states (DOS) of a system describes the number of states at each energy level that are available to be occupied. It is a horizontal projection of the band structure. The Kohn-Sham eigenvalues extracted from the results of DFT calculation can be used to determine the density of states (DOS) of a system. DOS analysis can provide useful information about the distribution of states in k-space and energy levels and therefore it is possible to determine energy gap of the material. Thus, electronic gap of amorphous $a - GaN_{1-x}As_x$ alloys have been analyzed through Electronic density of states (EDOS).

It is important to correlate the irregularities or defects in the amorphous structure with EDOS for further understanding. Thus, in order to understand the electron localization one can use the inverse participation ratio (IPR) [100]. IPR can identify a level as belonging to the band (delocalized), to the band-tail (partially localized), or to the gap (highly localized). The electronic localization of the band tail states can be characterized by inverse participation ratio, IPR, which can be defined as:

$$IPR = \frac{N \sum_{i=1}^{N} [n_i]^2}{(\sum_{i=1}^{N} [n_i])^2} \tag{3.10}$$

where $n_i = |\psi_i|^2$ is the electron density at site i and the sums extend to all sites N in the system. For an ideally localized state, only one atomic site contributes all the charge and so IPR=1. For a uniformly extended state, the charge contribution per site is uniform and equals 1/N and so IPR=1/N. Thus, large IPR corresponds to localized states. With this measure one can predict the bandgap of the amorphous structure [101].

### 3.6.2 Summary

In this chapter, we reviewed different computational methods such as *Ab initio* Molecular Dynamics , Classical Molecular Dynamics and Continuous Ran-

dom Network model and provided the calculation methods used throughout this thesis. We also introduced some brief definitions which are necessary to understand topology of the structures.

# CHAPTER 4

# MODELING OF THE AMORPHOUS $GaN_{0.5}As_{0.5}$ ALLOY

## 4.1 Introduction

It has been shown that $GaN_{1-x}As_x$ alloys are amorphous in the composition range of $0.17 > x > 0.75$ and crystalline outside this region [1, 2]. The band gap of the $GaN_{1-x}As_x$ alloy system varies from $\sim$ 0.8 eV to $\sim$ 3.4 eV. It has been seen from the experimental band gap of both As-rich [3] and N-rich [4] GaNAs that the theoretical models like virtual crystal approximation (VCA) or forced quadratic fitting cannot explain the experimental gap energies using a single bowing parameter. There is a lack of theoretical calculations for modeling of amorphous GaNAs alloys. This chapter present a brief comparison of the three methods that we have used to model amorphous $GaN_{1-x}As_x$.

In order to study amorphous $GaN_{0.5}As_{0.5}$ alloy at an atomistic level we have first performed *ab initio* molecular dynamics (AIMD) technique based on plane wave LDA. Second we have performed classical molecular dynamics using Tersoff potential as a force field. *Ab initio* MD calculations were carried out using the Vienna *Ab initio* Simulation Package (VASP) and classical molecular dynamics calculations were carried out using the Large-scale Atomic/Molecular Massively Parallel Simulator (LAMMPS). To generate the amorphous $GaN_{0.5}As_{0.5}$ alloy, we have used quenching from the melt method. As a final relaxation, we have always performed *ab initio* relaxation. Finally, we have also performed the continuous random network (CRN) model to generate the $GaN_{0.552}As_{0.448}$ alloys. This effective method has been successfully applied to generate model systems as diverse as amorphous silicon [91, 102], paracrystalline silicon [103], vitreous silica [104], GaN [105], InN [106], AlGaN [107] or GaAs[108]. For all models, the network topology is analyzed through radial distribution functions. The main features of the electronic structure are explained by analyzing the electronic density of states (EDOS). Finally, comparison of these three methods are presented.

## 4.2 *Ab initio* Molecular Dynamics Simulation of $GaN_{0.5}As_{0.5}$

We have performed *ab initio* molecular dynamics (AIMD) technique based on plane wave LDA to analyze amorphous $GaN_{0.5}As_{0.5}$ alloy at an atomistic level. The calculations were carried out using the Vienna *Ab initio* Simulation Package (VASP), where the electronic wavefunctions of the valence electrons are expanded in a plane wave basis set.

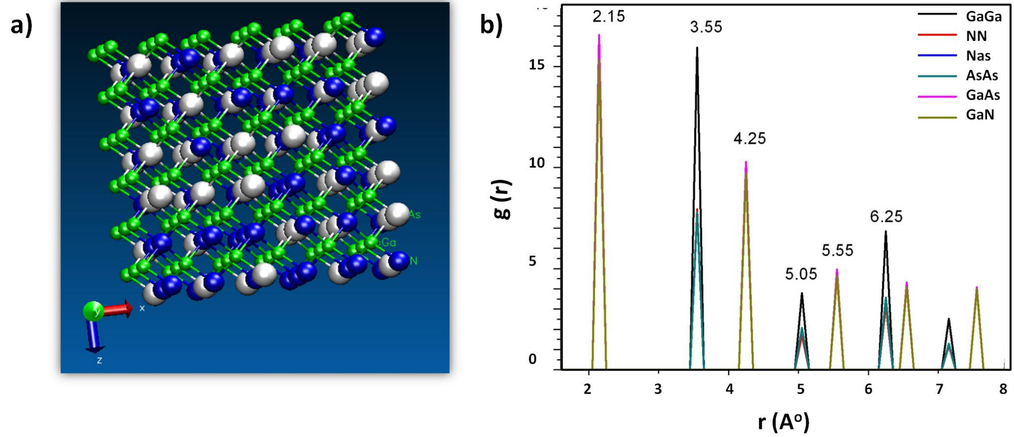


Figure 4.1: a) Initially random 216-atom model and b) Partial-pair distribution functions (PDFs) of initial $ZB - GaN_{0.5}As_{0.5}$. Blue (dark sphere), green and white (big bright sphere) spheres represents N, Ga and As atoms, respectively.

First of all, we have constructed an initial random 216-atom models of a cubic $ZB - GaN_{0.5}As_{0.5}$ alloy as shown in Fig.4.1-a and performed AIMD method to generate amorphous structure through the melt-quenching simulation. The size of the unit cell was calculated from Vegard's law. The partial pair distribution function of the initial ZB-$GaN_{0.5}As_{0.5}$ is depicted in Fig. 4.1-b. The initial crystal structure was first melted at high temperatures to achieve a completely disordered arrangement of atoms. It is also desired that all atoms forget their initial positions. The system is then quenched to 300K in 8 psec and equilibrated. Lastly, the system is relaxed to a local minimum energy configuration. During MD procedure, the volume of the cell was kept constant during the final relaxation and the shape and volume of the cell is allowed to change in order to ensure a zero pressure model. Final structure of $GaN_{0.5}As_{0.5}$ alloy and applied procedure are illustrated in Fig.4.2. Blue (dark sphere), green and white (big bright sphere) spheres represent N, Ga and As atoms, respectively, in Fig.4.2.

The quenching from the melt method can introduce bond defects into the structure, therefore a topology analysis of the final structure is necessary. We present in Fig.4.3 the corresponding partial-pair distribution functions of the generated amorphous $GaN_{0.5}As_{0.5}$ ($a - GaN_{0.5}As_{0.5}$) alloy. In order to obtain

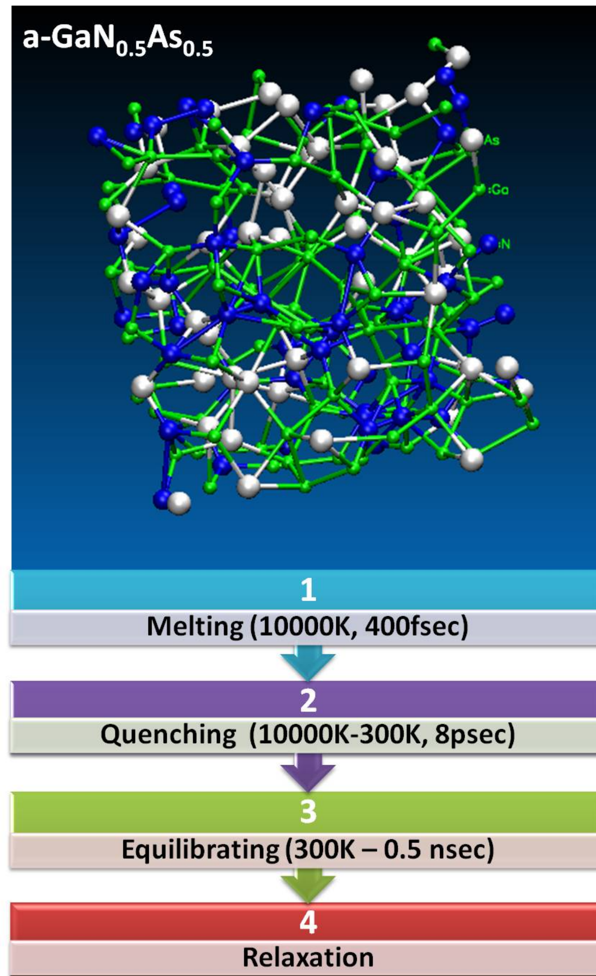


Figure 4.2: *Ab initio* Molecular Dynamics Scheme

realistic amorphous structure, any atom must built in such a way that it must retain its natural coordination (no dangling bonds) and also there must be no-homopolar bonds in the structure. The partial pair correlation function before (dash line) and after (solid line) relaxation is shown in Fig.4.3. It is noticeable from Fig.4.3 that pair distribution functions (PDFs), g(r), of unlike and like pairs of $a - GaN_{0.5}As_{0.5}$ alloy is almost the same before and after relaxation. Partial pair correlation functions of the Ga-N has a peak position at $1.95\mathring{A}$ representing the bond length for Ga-N pair. This value is in good agreement with experiment [1, 2]. We have determined the bond length for Ga-As pair as $2.55\mathring{A}$ which is higher than the experimental result of $2.45\mathring{A}$ [1, 2]. It is also noticable from Fig.4.3 that there is a considerable amount of N-As, N-N and As-As homopolar bonds in the network before and after the relaxation.

We use *ab initio* calculations within the local density approximation (LDA) to investigate the electronic properties of $a-GaN_{0.5}As_{0.5}$ of 216 atom model. The electronic properties of the structure has been investigated by means of density

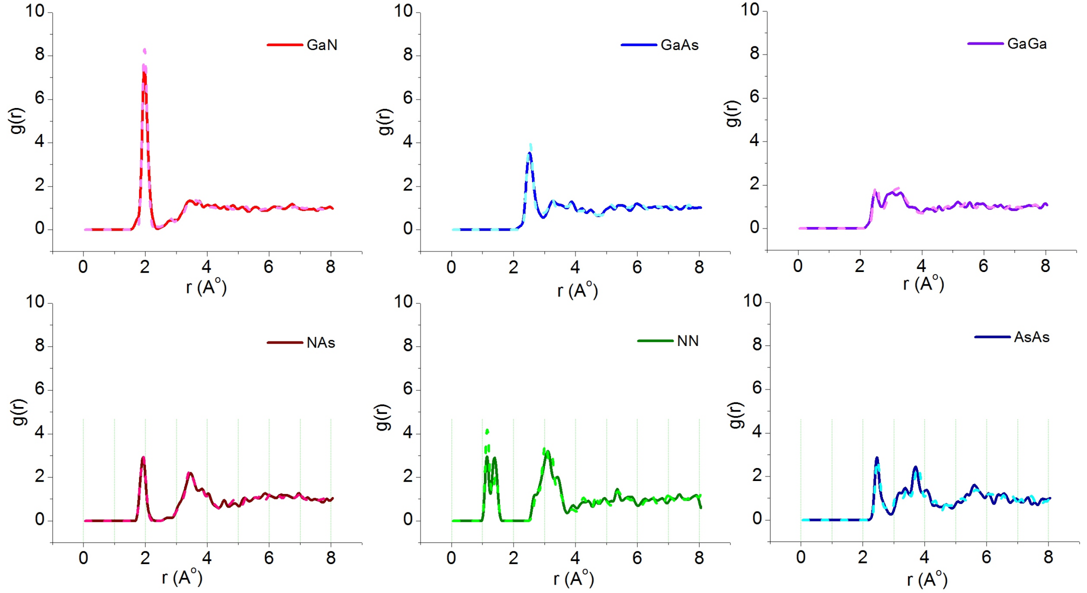


Figure 4.3: Partial-pair distribution functions of 216 atom model of $a-GaN_{0.5}As_{0.5}$, obtained from AIMD method, before (dash line) and after (solid line) the relaxation.

of states (DOS). However the local density approximation and density functional theory generally calculate the energy band gap of the structure smaller than that of the experiment. Because of this we have also used the corrected local density approximation (LDA+C) to obtain electronic density of states (EDOS). EDOS of $a-GaN_{0.5}As_{0.5}$ obtained with LDA (dash line) and LDA+C (solid line) are presented in Fig.4.4. As can be seen from Fig.4.4 there isn't an energy gap for $a-GaN_{0.5}As_{0.5}$ system using LDA or LDA+C. This could be as a result of the high number of homopolar bond in the structure. Even though lower melting temperature and longer simulation time may improve the quality of the $a-GaN_{0.5}As_{0.5}$ this method is computationally quite expensive to generate $a-GaN_{0.5}As_{0.5}$. Therefore we have decided to continue with classical molecular dynamics simulation which could reach much higher simulation time with lower computational power.

## 4.3 Classical Molecular Dynamics Simulation of $GaN_{0.5}As_{0.5}$

Similar to the AIMD simulation we have constructed an initial random 216-atom model of a cubic $ZB-GaN_{0.5}As_{0.5}$ and performed classical molecular dynamics method to generate amorphous structure through the quenching from the melt. Periodic boundary conditions have been used in all simulations. Nose-Hoover thermostat have been applied with a time step of 1 fs in the canonical

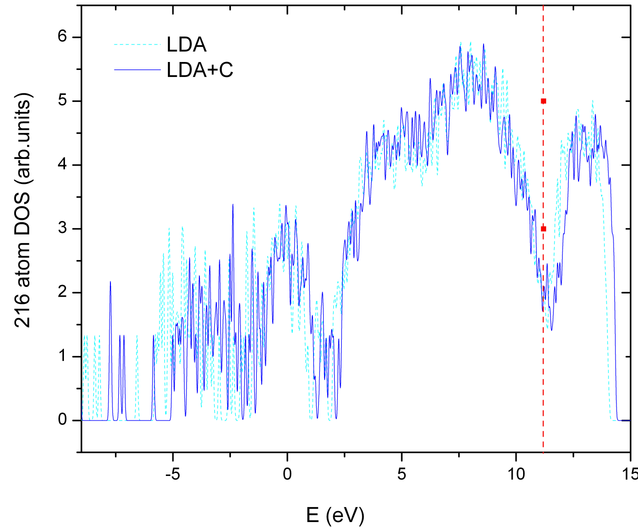


Figure 4.4: Electronic Density of States (EDOS) of $a - GaN_{0.5}As_{0.5}$ calculated by LDA and LDA+C at 300K. Vertical line indicates the position of Fermi level, $E_F$.

ensemble (NVT) simulations. Furthermore, we have used Tersoff-type potentials to describe the covalent bonding of the III-V structure. Tersoff model allows the formation and dissociation of covalent chemical bonds during simulation.

### 4.3.1 Three body Tersoff potential

Fig.4.5 shows the interatomic forces between atoms of covalently bonded molecule. When two isolated atoms are at a great distance from one another, there isn't any attractive or repulsive forces. However, as the atoms approach more closely, the attractive and repulsive forces between the two atoms become important. At very short distances, repulsive forces become more important than attractive forces, and the atoms repel each other. The interatomic potential has a minimum value at equilibrium with a bond length of $R_0$.

There are many analytical interatomic potential energy proposed to simulate different types materials. Since electronic properties of lattice mismatched epitaxial semiconductor layers are strongly affected by their structural properties, one should be careful while choosing the interatomic potential [109]. D. Powell et al. were obtained accurate Tersoff potential parameterisations for ZB III-As and III-N semiconductors. These parameter sets allow to reproduce calculated DFT-LDA values correctly. These allow also the implementation of molecular dynamics and molecular statics simulations [110].

The total potential energy of the Tersoff-Brenner can be written as a sum

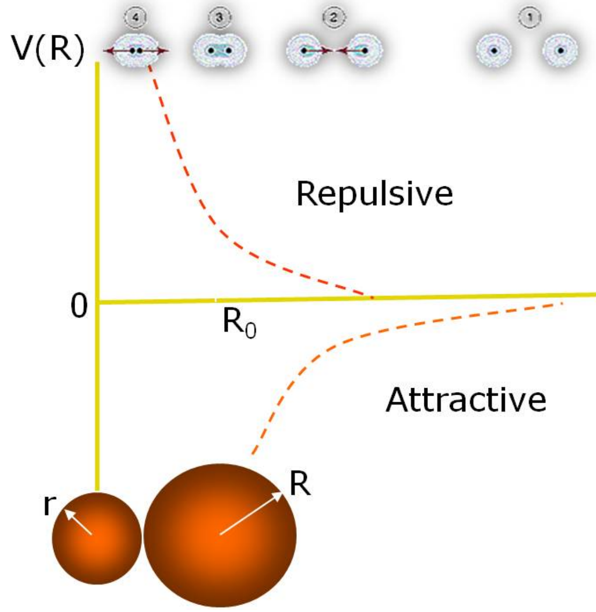


Figure 4.5: Interatomic potential of a dimer with respect to interatomic distance.

over individual bond energies.

$$E = \frac{1}{2}\sum_{i}\sum_{j\neq i} f_C(r_{ij})[f_R(r_{ij}) + b_{ij}f_A(r_{ij})] \tag{4.1}$$

The interaction is restricted to the next-neighbor sphere by a cut-off function

$$f_C(r) = \begin{cases} 1 & r < R - D, \\ \frac{1}{2}[1 - sin[\pi(r-R)/2D]] & R - D < r < R + D, \\ 0 & r > R + D. \end{cases}$$

where R and D are adjustable quantities.

The pair-like attractive and repulsive energies are given as Morse-like terms,

$$f_R(r) = Ae^{-\lambda_1 r}, \tag{4.2}$$

$$f_A(r) = -Be^{-\lambda_2 r}, \tag{4.3}$$

$$A = \frac{D_0}{S-1}e^{\lambda_1 r_0}, \tag{4.4}$$

$$B = \frac{SD_0}{S-1}e^{\lambda_2 r_0}, \tag{4.5}$$

$$\lambda_1 = \beta\sqrt{2S}, \tag{4.6}$$

$$\lambda_2 = \beta\sqrt{\frac{2}{S}}. \tag{4.7}$$

where $f_R$ is a two-body term and $f_A$ includes three-body interactions. The summations in the formula are over all neighbors j and k of atom i within a cutoff

distance of (R + D). The pair-like attractive and repulsive energies depend on the dimer energy $D_0$, the dimer bond distance $r_0$ and the adjustable parameter S. The parameter $\beta$ can be determined by the ground state oscillation frequency of the dimer. The bond order parameter $b_{ij}$ includes the angular dependencies, which are necessary to accurately model the deformation of covalent bonds.

$$b_{ij} = [1 + \beta\chi_{ij}]^{-1/2}, \tag{4.8}$$

$$\chi_{ij} = \sum_{k\neq i,j} f_C(r_{ik}) g(\theta_{ijk}) e^{\lambda_3(r_{ij}-r_{ik})}. \tag{4.9}$$

The angular function $g(\theta)$ is given by

$$g(\theta) = \gamma_{ijk}\left(1 + \frac{c^2}{d^2} - \frac{c^2}{[d^2 + (\cos\theta - \cos\theta_0)^2]}\right) \tag{4.10}$$

**Modification of Tersoff potential**

We have used the same parameters suggested in K.Albe et al.'s reports [111, 112] for the Ga-N, N-N, As-As and Ga-As dimers. However after classical MD simulation we have observed noticeable number of N-N, Ga-Ga, As-As and As-N bonds in the first nearest neighbor distance similar to that of the AIMD simulation. Once these bonds have been formed it is not possible to remove them by means of relaxation. N-N bonds are especially quite strong and usually this kind of dimers produces $N_2$ molecule with a bond length of 1.3$\mathring{A}$ . As mentioned before the electronic properties of amorphous semiconductors are strongly depended on the network topology. Thus we have modified the two-body interaction terms of N-N, Ga-Ga, As-As and N-As accordingly to avoid the homopolar and unwanted bonding during melting process. The two body interaction terms are plotted according to parameters suggested in K. Albe et al. (see Fig.4.6.a ) and modified two-body interaction terms as a function of atomic separation (see Fig.4.6.b). We have also increased the equilibrium bond length of $R_0$ for modified two-body interaction functions. These modification have been obtained by adjusting the interaction parameters of the two-body potentials of N-N, Ga-Ga, As-As and As-N pairs, which are listed in Table.4.1, to obtain smoother functions. During these procedure interaction parameters of the two-body potentials of Ga-As and Ga-N binaries are taken as they are suggested in the literature.

Fig. 4.6.a shows the total Tersoff-Brenner type potential energy calculated according to parameters suggested in K.Albe et al.[111, 112] for each dimer in the structure. Fig. 4.6.b depicts the modified version of total Tersoff-Brenner type potential energy. Latter one is calculated by modifying the two-body term and equilibrium bond length of $R_0$ of the binary pairs of $V_{Ga-N}$, $V_{Ga-As}$, $V_{N-As}$, $V_{N-N}$, $V_{As-As}$ and $V_{Ga-Ga}$ . Parameters of $\gamma$, $\lambda_3$, c, d, h and $\beta$ have been calculated from

arithmetic mean of N and As values for the $V_{N-As}$ potential. On the other hand, the parameters of R, D, S, $D_0$ and $r_0$ have been calculated from geometric mean of N and As for the $V_{N-As}$ potential. The initial crystal structure is melted at 1200K in 5.5 nsec. It is observed that higher temperature leads to phase separations as GaAs:N (Fig.4.7) before melting temperature similar to experiment.

After melting at 1200K, the system is quenched to 300K in 1 nsec and

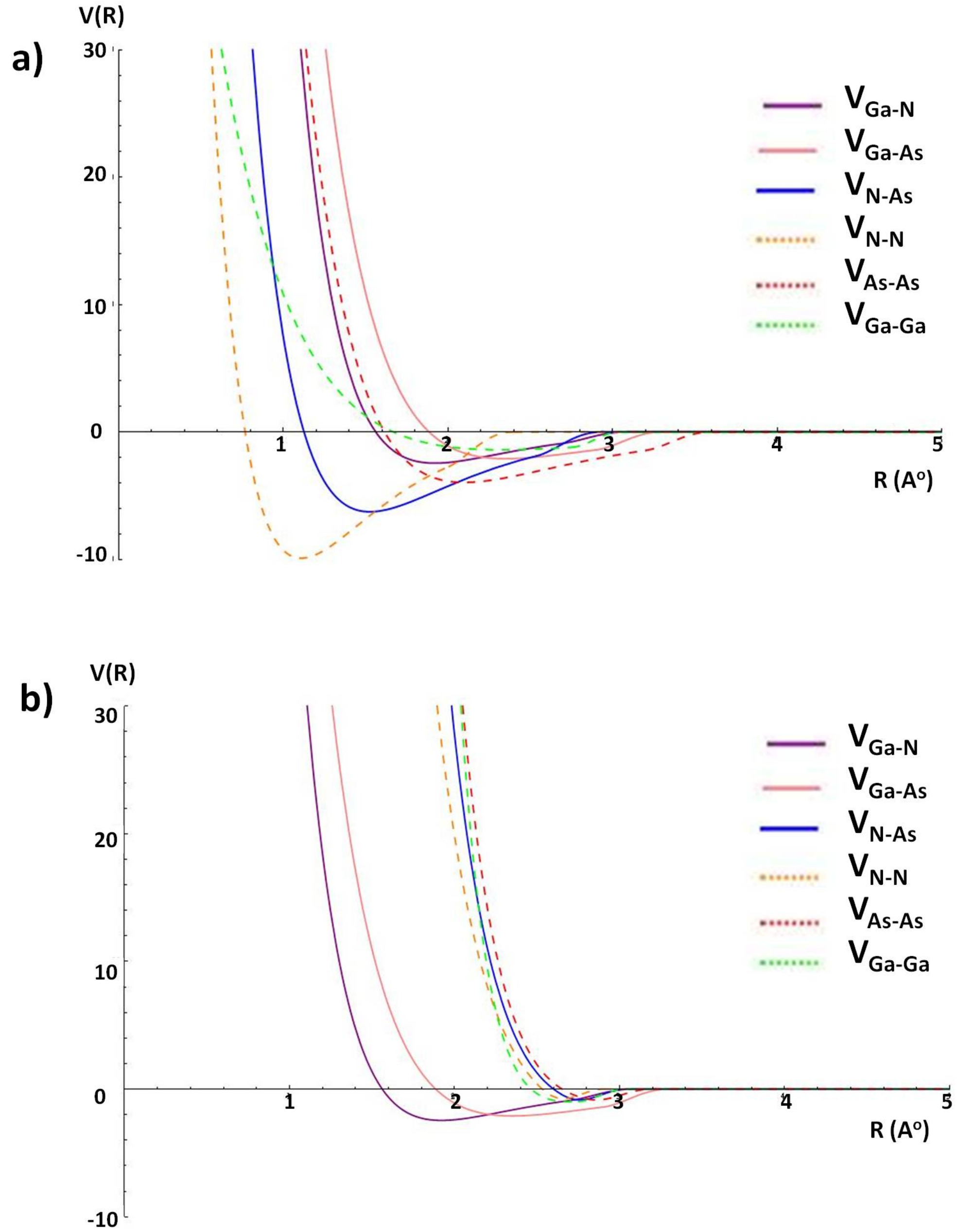


Figure 4.6: Tersoff-Brenner type total potential energy for Ga-N, Ga-As, N-As, N-N, As-As and Ga-Ga dimers according to a) parameters suggested in K. Albe et al.[111, 112] and b) modified two body interaction terms as a function of atomic separation ($\AA$ ).

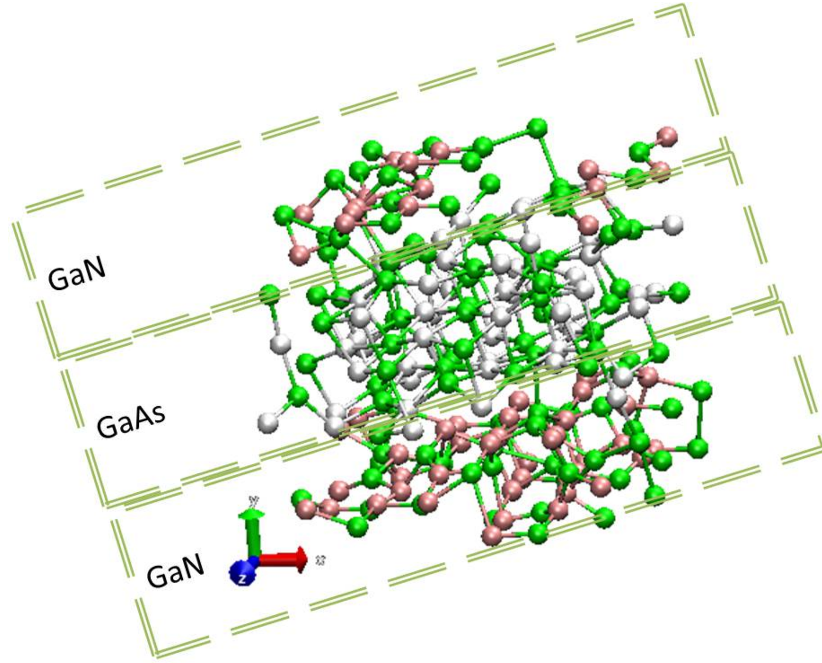


Figure 4.7: Phase separation of $GaN_{0.5}As_{0.5}$ alloy as GaAs:N before the melting temperature

equilibrated in 0.5 nsec. Finally, the system is relaxed to a local minimum energy state via *ab initio* relaxation. Topology of the resultant structure is illustrated at the top of the Fig.4.8. Blue (dark sphere), green and white (big bright sphere) spheres represents N,Ga and As atoms, respectively.

The pair correlation functions of $a - GaN_{0.5}As_{0.5}$ are depicted in Fig.4.9.

Table 4.1: Parameter sets for the three interaction types [111, 112].

| ij | Ga-N | Ga-As | Ga-Ga | N-N | As-As |
|---|---|---|---|---|---|
| $\gamma$ | 0.001632 | 0.0166 | 0.007874 | 0.76612 | 0.455 |
| S | 1.1122 | 1.1417 | 1.11 | 1.4922 | 1.86 |
| $\beta(\AA^{-1})$ | 1.968 | 1.5228 | $1.08 \Rightarrow 3.0^*$ | $2.05945 \Rightarrow 1.5^*$ | $1.435 \Rightarrow 2.0^*$ |
| $D_0$ (eV) | 2.45 | 2.1 | $1.40 \Rightarrow 1.0^*$ | $9.91 \Rightarrow 2.0^*$ | $3.96 \Rightarrow 1.0^*$ |
| $R_0$ ($\AA$) | 1.921 | 2.35 | $2.3235 \Rightarrow 3.1^*$ | $1.11 \Rightarrow 3.3^*$ | $2.1 \Rightarrow 3.3^*$ |
| c | 65.207 | 1.29 | 1.918 | 0.178493 | 0.1186 |
| d | 2.821 | 0.56 | 0.75 | 0.20172 | 0.1612 |
| h=cos($\theta_0$) | 0.518 | 0.237 | 0.3013 | 0.045238 | 0.7748 |
| $\lambda_3 = 2\mu(\AA)^{-1})$ | 0 | 0 | 1.846 | 0 | 3.161 |
| $R_{cut}(\AA)$ | 2.9 | 3.1 | $2.95 \Rightarrow 2.9^*$ | $2.2 \Rightarrow 2.7^*$ | $3.4 \Rightarrow 3.0^*$ |
| $D(\AA)$ | 0.2 | 0.2 | 0.15 | 0.2 | 0.2 |

* modified parameters

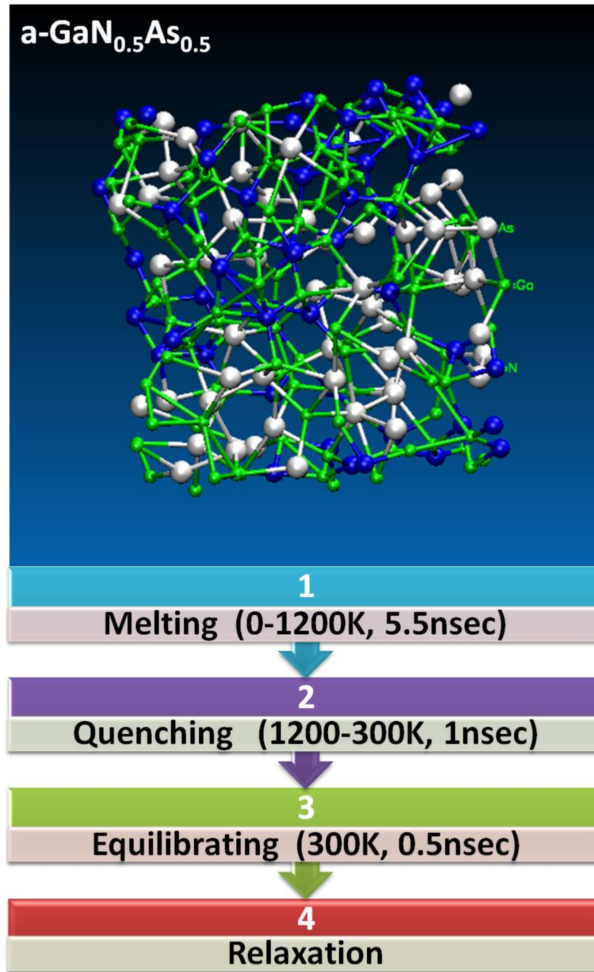


Figure 4.8: Classical Molecular Dynamics Scheme

It is clearly seen from the Fig.4.9 that there are no homopolar bonds of N-N, Ga-Ga, As-As or unwanted like As-N in the structure. At this point we can therefore offer our modified Tersoff potential as an ideal initial network for $a-GaN_{0.5}As_{0.5}$ modeling. However we have observed an insignificant number of unwanted bonds of N-N, N-As and As-As after *ab initio* (conjugated gradient) relaxation. Although their numbers are much smaller than that of the results of *Ab initio* molecular dynamics, one should calculate the EDOS to analyze the electronic structure of the system for further understanding.

The electronic density of states calculation of the 216-atom model of $a-GaN_{0.5}As_{0.5}$ is presented in Fig.4.10. According to our calculated results there is no band gap for $a-GaN_{0.5}As_{0.5}$ with this technique too. It can also be concluded from our calculated results that when the number of homopolar bonds decrease, both conduction- and valance-bands get deeper.

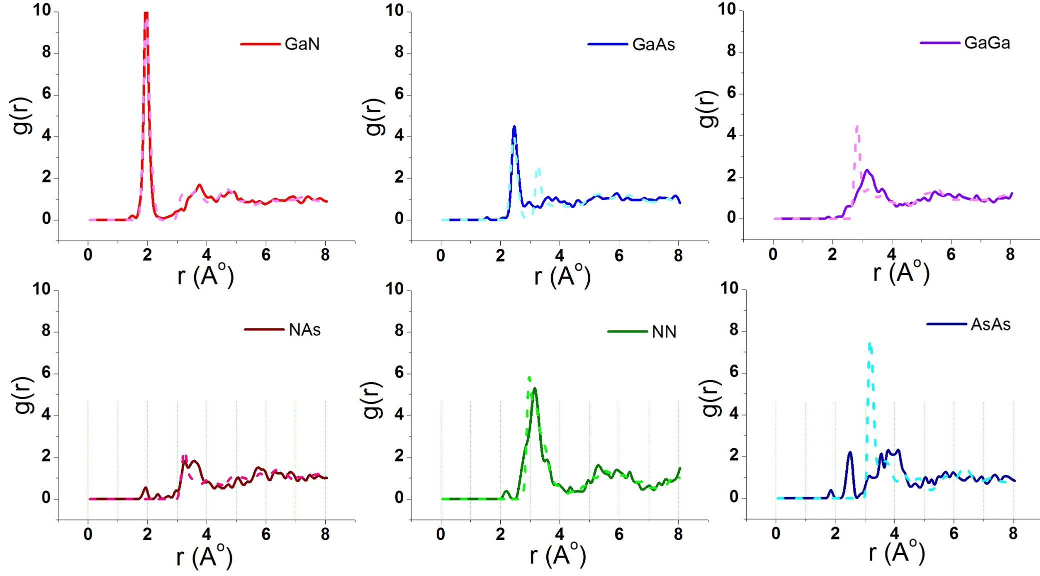


Figure 4.9: The partial-pair distribution functions of *Ab initio* relaxed 216-atom model of $a - GaN_{0.5}As_{0.5}$ via classical molecular dynamics.

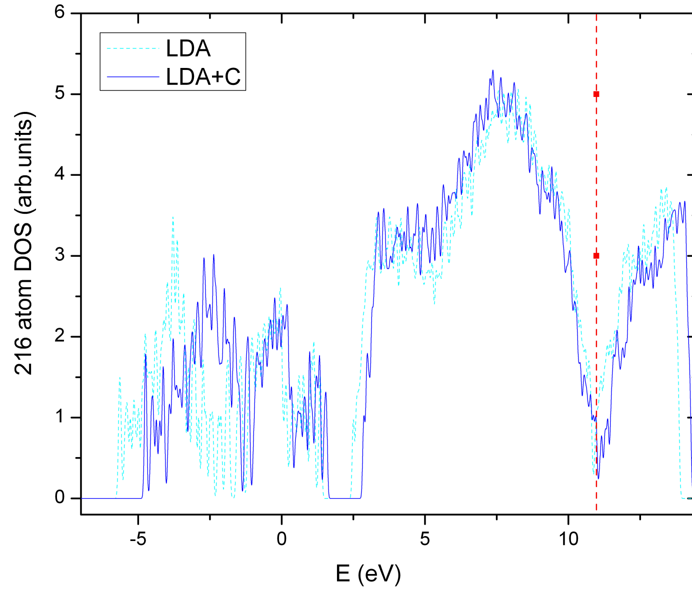


Figure 4.10: Electronic density of states (EDOS) of $a - GaN_{0.5}As_{0.5}$ calculated by LDA and LDA+C based on classical molecular dynamics model simulation

## 4.4 Continuous Random Network Modeling of $GaN_{0.552}As_{0.448}$

Continuous random network (CRN) model can be used as an alternative method to obtain realistic amorphous structure for such a highly ionic structure. CRN model is an idealized model for perfectly coordinated amorphous semicon-

ductors. This effective method has been successfully applied to generate model systems as diverse as amorphous silicon [91, 102], paracrystalline silicon [103], vitreous silica [104], GaN [105], InN [106], AlGaN [107] or GaAs[108].

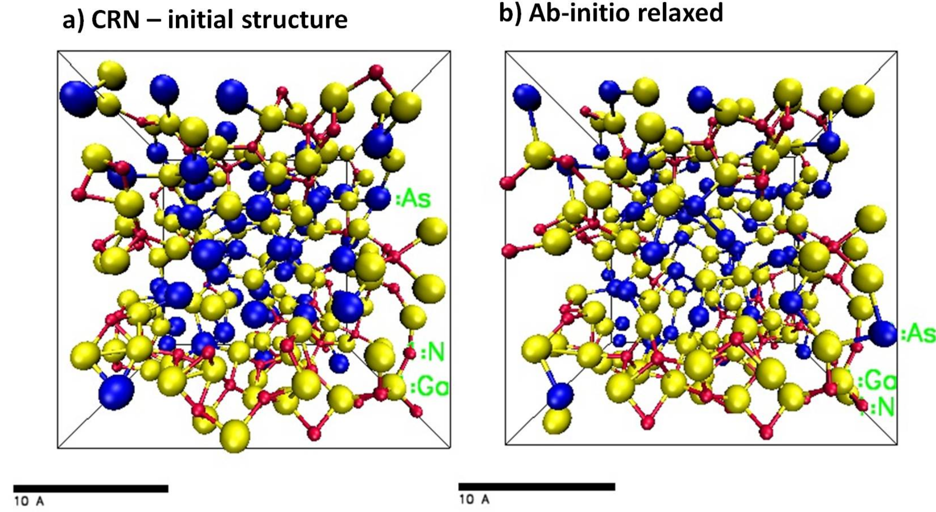


Figure 4.11: a) The topology of $a-GaN_{0.552}As_{0.448}$ structure before and b) after DFT relaxation.

Chemically ordered 250-atom model of amorphous $GaN_{0.552}As_{0.448}$ alloys have been studied with first principle density functional theory, starting with initial continuous random network structures. Initial structure of $a-GaN_{0.552}As_{0.448}$ was obtained from the $ZB-GaN_{0.552}As_{0.448}$. Keating potential is used as a force field and ideal bond length of of Ga-N and Ga-As were set to their experimental values of 0.195 nm and 0.246 nm [1], respectively. The initial structure is first relaxed by using the modified Wooten-Winer-Weaire (WWW) algorithm. It has been observed that all bond lengths were already close to their ideal values after modified Wooten-Winer-Weaire (WWW) relaxation. The nuclear positions were then fully relaxed using first principle DFT calculations until the forces were smaller than 0.02 $eV/\ \AA$ by density-functional methods in the local density approximation (LDA) and Vanderbilt's Ultrasoft pseudopotential. The simulations were performed with the Vienna *Ab initio* simulation package (VASP). During relaxation, atomic positions and lattice (cell volume) have been optimized one after another by conjugate gradient method. The shape of the cell was kept the same.

Fig.4.12 shows the calculated partial pair and total radial distribution functions of $a-GaN_{0.552}As_{0.448}$ after DFT relaxation. It can be seen from these figures that resultant structure of $a-GaN_{0.552}As_{0.448}$ do not have any homopolar or unwanted bonds.

Fig.4.13 illustrates the electronic density of states of $a-GaN_{0.552}As_{0.448}$

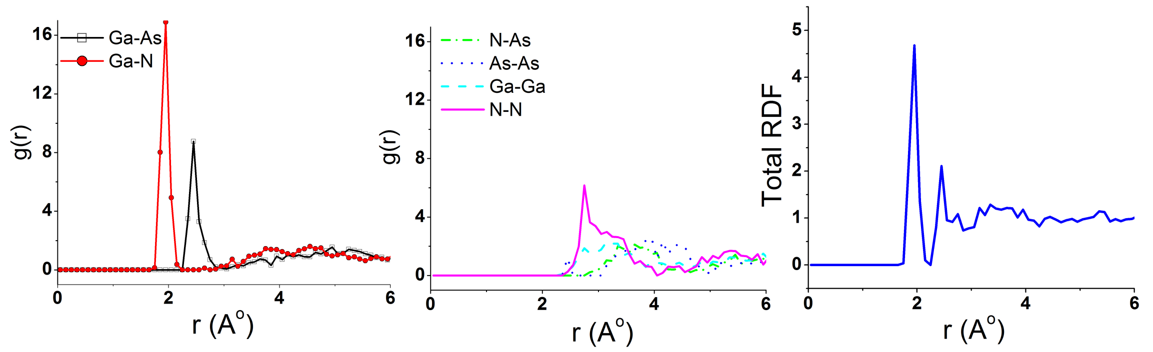


Figure 4.12: The partial-pair and total radial distribution functions of $a - GaN_{0.552}As_{0.448}$ after DFT relaxation.

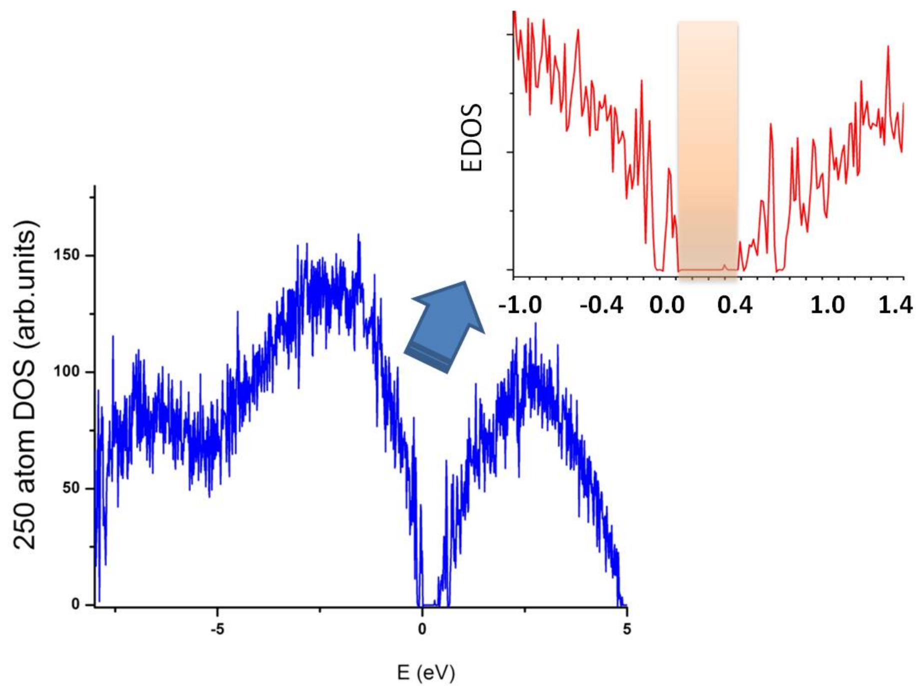


Figure 4.13: Electronic density of states of 250 atom model of $a{-}GaN_{0.552}As_{0.448}$. The Fermi level is at 0 eV.

with a bandgap of 0.8 eV. The measured bandgap of $a - GaN_{0.552}As_{0.448}$ is approximately 1.7 eV. Although the density-functional methods in the local density approximation (LDA) is generally very successful in predicting atomic structures, it usually underestimates the band gaps in semiconductors. In this situation this result is acceptable and we can confirm that the CRN is reliable method for modeling $a - GaN_{0.552}As_{0.448}$.

### 4.5 Summary

This chapter presents a DFT study of the atomic structure and electronic properties of highly mismatched alloys of amorphous $GaN_xAs_{1-x}$. We have investigated atomic structures and electronic properties of amorphous $GaN_{0.5}As_{0.5}$ by performing first principles local basis molecular dynamics (MD) and classical MD simulations. Our initial structure of $GaN_{0.5}As_{0.5}$ consist of randomly distributed 216-atoms inside the unit cell. Pair correlation functions of the resultant structures show that Ga-As and Ga-N peaks are dominant in the structure and the peak values are in agreement with experimental results. We also find that classical MD results (at 300 K) has less homopolar bonding according to pair correlation function even after conjugated gradient relaxation. We have calculated that the density of states (DOS) for both systems using local density approximation, LDA and band corrected local density approximation, LDA+C. Although we haven't found energy gap for both systems, we have seen that the reduction in homopolar bonds causes deeper conduction- and valance- band valley. As far as we know there is no theoretical work done on a-GaNAs for comparison up to our knowledge.

In addition, CRN model is used to generate the amorphous $GaN_{0.552}As_{0.448}$ network. We have used a 250 atom unit cell to represent the a-GaNAs structure. Density-functional theory is used to relax the network in the local density approximation (LDA) and Vanderbilt's Ultrasoft pseudopotential. Initial and relaxed network was analyzed with the pair-correlation functions and angle distributions. No homopolar bonds have been found in the structure. It has seen that the $a - GaN_{0.552}As_{0.448}$ has a clear band gap of 0.8 eV. According to our calculations we conclude that CRN provides an ideal initial network close to minimum energy configuration that can be reached with first principle calculations for amorphous materials. The calculated bond lengths of 1.95 $\mathring{A}$ and 2.45 $\mathring{A}$ for Ga-N and Ga-As, respectively, are in good agreement with the experimental data.

# CHAPTER 5

## MODELING OF THE AMORPHOUS $GaN_{1-x}As_x$ ALLOYS

### 5.1 Introduction

The main motivation for this chapter is to generate realistic amorphous $GaN_{1-x}As_x$ models using continuous random network (CRN) and density functional theory by varying As concentration. We then investigate and compare its structural and electronic properties with experiments. For this aim we began with the generation of atomic configurations using continuous random network (CRN) approach starting with a perfectly coordinated 250 atom-models. Firstly, a cubic simulation box (unit cell) was defined with a number of atoms of Ga, As and N in proportion to the composition of the $GaN_{1-x}As_x$ alloy. The number of As atoms was chosen as 21, 34, 38, 56 and 88 for an As concentration in $a-GaN_{1-x}As_x$ of $0.168, 0.272, 0.304, 0.448$ and $0.704$, respectively. The density of unit cells are calculated from Vegard's law and were rescaled to reproduce the density of $a-GaN_{1-x}As_x$ alloys which is about 0.85 of their corresponding crystalline values [2].

These initial disordered configurations which were obtained from the perfect zinc blende structures are highly strained, but then relaxed using the modified Wooten-Winer-Weaire (WWW) algorithm. In this algorithm, the Keating potential is used, in which for our specific purpose the ideal bond length of Ga-N and Ga-As were set to their experimental values of 0.195 nm and 0.246 nm [1], respectively. Also added to the standard Keating potential is an energetic penalty for homopolar bonds.

After relaxation, all bond lengths are close to their ideal value, and average bond angles are calculated as 108.3° for all generated systems. Because of the high efficiency of the modified WWW algorithm for samples of this size, this process can be repeated many times, resulting in many configurations, from which we then select the ones with the highest network quality with respect to low strain in the network and low spread in bond-length and bond angle distribution.

After high-quality starting configurations are obtained in this way, the nuclear positions were fully relaxed using DFT calculations until the forces are smaller in magnitude than 0.02 $eV/\text{Å}$ by density-functional methods in the

local density approximation (LDA) and Vanderbilt's Ultrasoft pseudopotential. The simulations were performed with the Vienna *Ab initio* Simulation Package (VASP). Our tests show that using projector augmented wave (PAW) pseudopotential method yields essentially the same result. During relaxation, atomic positions and lattice (cell volume) have been optimized one after another by conjugate gradient method. The shape of the cell was kept the same.

## 5.2 Atomic Structure of Amorphous $GaN_{1-x}As_x$ alloys

### 5.2.1 Total Radial and Partial Pair Distribution Functions of $GaN_{1-x}As_x$

We analyze the disorder of the networks using radial distribution function, g(r), defined as [113],

$$g(r) = \lim_{dr \to 0} \frac{p(r)}{4\pi (N_{pairs}/V) r^2 dr} \tag{5.1}$$

where r is the distance between a pair of particles, $p(r)$ is the average number of atom pairs found at a distance between $r$ and $r + dr$, V is the total volume of the system, and $N_{pairs}$ is the number of unique pairs of atoms where one atom is from each of the two sets (selections), $sel_1$, $sel_2$. If $sel_1 = sel_2$ then $N_{pairs} = N_1(N_1 - 1)$. If there are no atoms shared between $sel_1$ and $sel_2$ , $N_{pair} = N_1 N_2$, where $N_1$ and $N_2$ are the number of atoms in $sel_1$ and $sel_2$, respectively. These functions can give the probability density of a particle is separated by a distance r from another one. In this section, we provide an analysis and a comparison of radial distribution functions of the initial configuration from the CRN model using the Keating potential and the one further relaxed using DFT calculations. The partial-pair correlation functions are calculated for amorphous $GaN_{1-x}As_x$ systems for As concentrations of 16.8%, 27.2%, 30.4%, 44.8% and 70.4%. Fig.5.1.a-f show these calculated results. We also provide the total radial distribution functions according to increasing As concentration as shown in Fig.5.1g and h. Partial-pair correlation functions of Ga-As, Ga-N, As-N, N-N, Ga-Ga and As-As pairs are indicated with different symbols as stated in Fig.5.1. It can be seen from these figures that there are two well defined nearest neighbor peaks corresponding to Ga-N and Ga-As pairs and then there is a rapid loss of the interatomic correlations for all As concentrations. This rapid loss and presence of broad peaks indicate that the networks are topologically disordered.

We have determined the bond lengths for Ga-N and Ga-As pairs as $1.95\mathring{A}$ and $2.45\mathring{A}$ from the CRN model, respectively. These calculated peak positions of Ga-As and Ga-N agree very well with experimental results [1, 2, 114, 115] which implies that the generated $a - GaN_{0.832}As_{0.168}$ unit cell manage to obtain

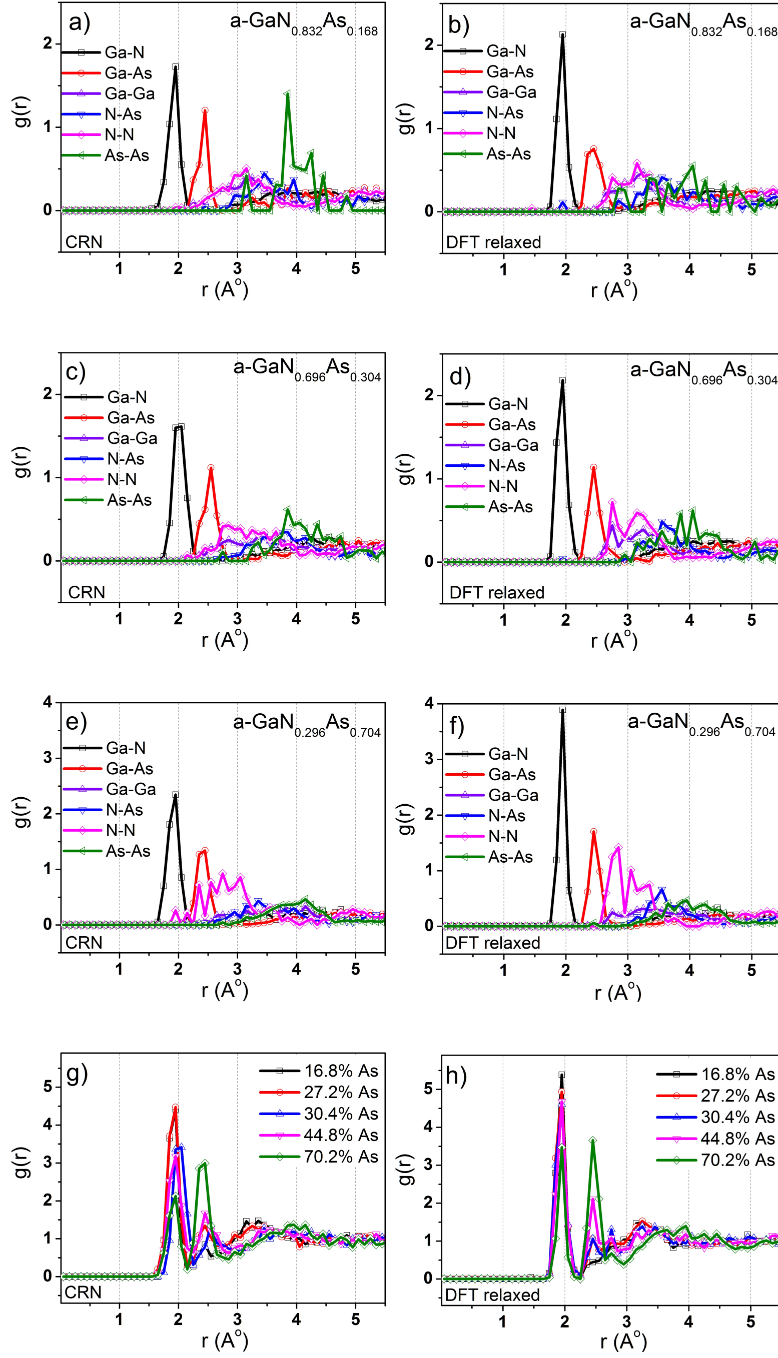


Figure 5.1: Total and partial-pair distribution functions (PDFs) of $a-GaN_{1-x}As_x$ for As concentrations of 16.8%, 30.4% and 70.4% by means of CRN model (left-hand side) and DFT relaxed (right hand side). A bin size of 0.1 Å used for calculations.

correct local structure order. Fig.5.1b illustrates the same analysis for the more accurate equilibrium structure found by relaxation through DFT calculations for $a-GaN_{0.832}As_{0.168}$. Same bond length values of $1.95\AA$ and $2.45\AA$ for Ga-N and Ga-As pairs, respectively, have been calculated confirming the validity of CRN model. It should be noticed from Fig.5.1a and b that the intensity of partial PDF of Ga-N pairs increases whereas that of Ga-As pairs decreases after DFT relaxation. However, a careful analysis reveals the fact that the areas under the related peaks of Ga-N and Ga-As are the same in Fig.5.1a and b, indicating that they have the same coordination numbers. Fig.5.1a also shows the presence of an strong As-As pair which is mostly localized around $3.8\AA$. However, other unwanted pairs such as N-N, Ga-Ga and N-As have broader unlocalized distribution in the CRN result. It has been seen that this strong peak corresponding to As-As pair is suppressed in Fig.5.1b which is obtained by relaxation of the $a-GaN_{0.832}As_{0.168}$ system. The reduction of As-As pair indicates a more homogenous distribution can be obtained after relaxation. Where chemical order is concerned it has been found that there is only one N-N homopolar bond and one N-As heteropolar bond within the first nearest neighbor distance for the DFT relaxed result. This can be acceptable for such a large unit cell. Overall our initial structure is already close to the final DFT relaxed configuration proves that the CRN model works quite well.

We now would like to investigate the effect of As concentration on the radial distribution function of $a-GaN_{1-x}As_x$ models. To do that we repeat the same calculations of Fig.5.1a and b for As concentrations of 0.304 and 0.704, see Fig.5.1c-f. These variations indicate that the increase in As concentration have no effect on the value of the bond length for Ga-N pairs for both models. On the other hand, a very slight change in the order of $\pm 0.1A^{\circ}$ in the peak position of Ga-As pair is observed in CRN model. However, the peak value of $2.45\AA$ has been obtained after DFT relaxation. One interesting point is that the N-N pairs prefer to shift to lower radial distances with increasing As concentrations. This is due to the fact that the increasing As concentration causes an increase in edge sharing tetrahedral bonds as we will illustrate in the next section. It is also noticeable from Fig 5.1.a-f that the number of wrong bonds such as N-N, Ga-Ga, As-N and As-As which are close to first nearest neighbor distance have been decreased with DFT relaxation. This indicates that the chemical order is also improved with DFT relaxation.

Fig.5.1g and h depict the total radial distribution functions (RDF) of the $a-GaN_{1-x}As_x$ alloys for different As concentrations of initial and relaxed models, respectively. It is evident from the total RDF that first and second sharp peaks are due to the Ga-N and Ga-As partial correlations, respectively. Minor contributions

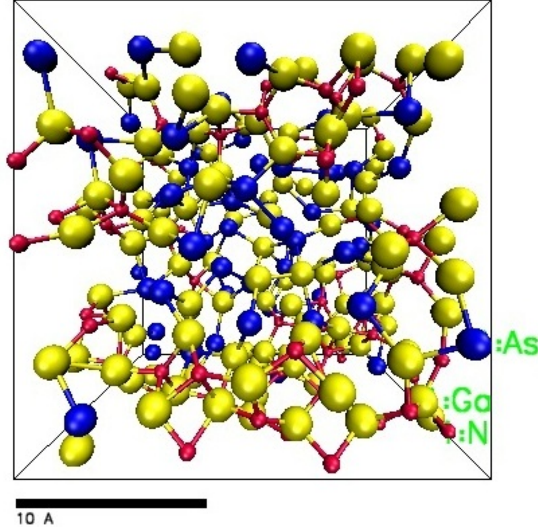


Figure 5.2: DFT relaxed 250-atom model of $a-GaN_{0.552}As_{0.448}$ cell. Red (small dark sphere) represents nitrogen, blue (big dark sphere) represents arsenic and yellow (bright sphere) represents gallium.

to the second peak are due to from N-N and Ga-Ga partial correlations. It is clearly seen from Fig.5.1g and h that Ga-As partial correlations becomes stronger and Ga-N partial correlation becomes weaker with increasing As concentrations as expected. As a general demonstration of $a-GaN_{1-x}As_x$ we present the atomic structure of our final 250-atom model for As concentrations of 44.8% in Fig.5.2.

### 5.2.2 Bond Angle Distribution

The most significant partial bond angle distributions are plotted with respect to the bond angle in Fig.5.3 for Ga-N-Ga, Ga-As-Ga, N-Ga-N, As-Ga-As and As-Ga-N pairs for DFT relaxed systems. These triple-correlation functions are defined as an average of bond angles between a reference atom and the pairs of atoms within a radius of first minimum of the total radial correlation function. We approximated the triple bond angle distribution by Gaussian function since bond angle distributions of large continuous random networks can be defined by Gaussian distribution [116]. According to Fig.5.3a, gaussian bond angle distribution of As-Ga-As correlations have an average bond angle of $102.64°, 113.5°, 106°, 107.2°$ and 107.8°'s with increasing As concentrations. These results show that in a short range order As-Ga-As tends to form tetrahedral structure for all systems and higher As concentration seems closer to the ideal tetrahedral bond angle.

Fig.5.3b shows the partial bond angle distribution of N-Ga-N correlation. Two peaks are observed as pre-peak and main peak which has a mean bond angle of 89.32° and 109.48°, respectively. Similar observations have been reported for a-GaN by Cai et al. [105]. Combining the results of Ga-Ga partial PDF with

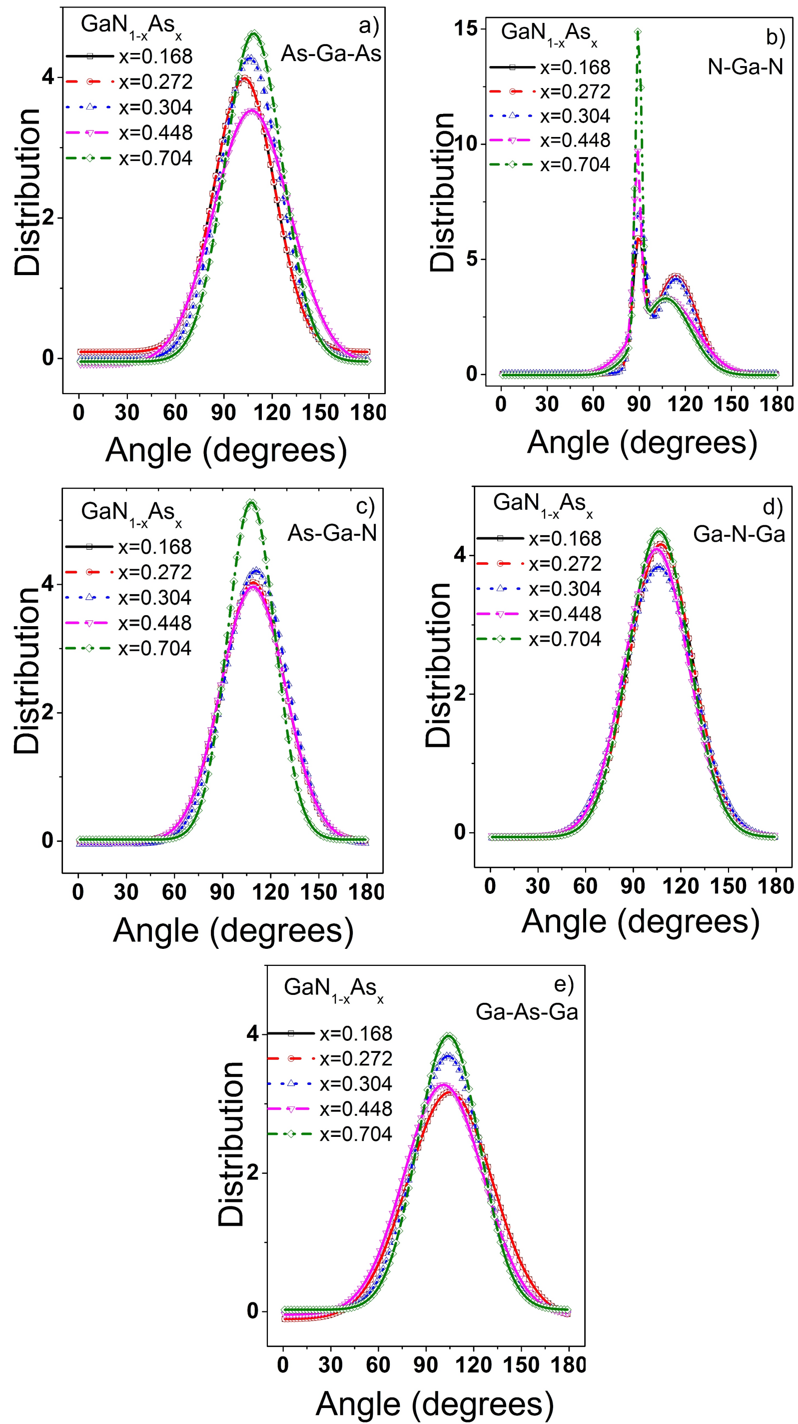


Figure 5.3: Partial bond-angle distribution in amorphous $GaN_{1-x}As_x$ alloys for triple-correlation function As-Ga-As, N-Ga-N, As-Ga-N, Ga-N-Ga and Ga-As-Ga as a function of As concentrations.

that of the N-Ga-N angle distribution one can conclude that the pre-peak can be related to edge sharing N tetrahedral structures and the main peak corresponds to the ideal tetrahedral structure. It is also observed that the number of edge sharing tetrahedral structure increases with As concentrations. The partial bond angles of As-Ga-N, Ga-N-Ga and Ga-As-Ga which are depicted in Fig.5.3c, d and e have mean values over all As concentrations as $108.7°, 105.6°$ and $102.8°$'s, respectively, being close with that of ideal tetrahedral bond angle of $109.45°$. The detailed investigations of Fig.5.3 reveals that full with at half maximum (FWHM) of triple-correlation functions decreases with As concentration. This shows that the bond angle disorder decreases with increasing As concentration.

### 5.2.3 Ring Statistics and Coordination Number

In this section we present the ring statistics and average coordination number of DFT relaxed $a-GaN_{1-x}As_x$ networks according to tetrahedral structures. We have calculated all rings in $a-GaN_{1-x}As_x$ using proper cut-off distances within periodic boundary conditions. The related cut-off distance for each pair has been determined by analyzing the partial-pair distribution functions of the network. Fig.5.4 shows the corresponding histogram of the primitive rings per cell distribution, $R_C$, of $a-GaN_{1-x}As_x$ for As concentrations of $0.168, 0.304$ and $0.704$.

A ring is defined as a closed path that includes a series of nodes and nearest neighbor bonds connected sequentially without overlapping. A ring is primitive (or irreducible) if it cannot be decomposed into smaller rings. The size of a ring is the number of atoms within a closed path [94]. A perfect tetrahedral structure has only 6-membered irreducible rings. In our model the most favored number of atoms in the ring statistic is also six which corresponds to fourfold coordination as

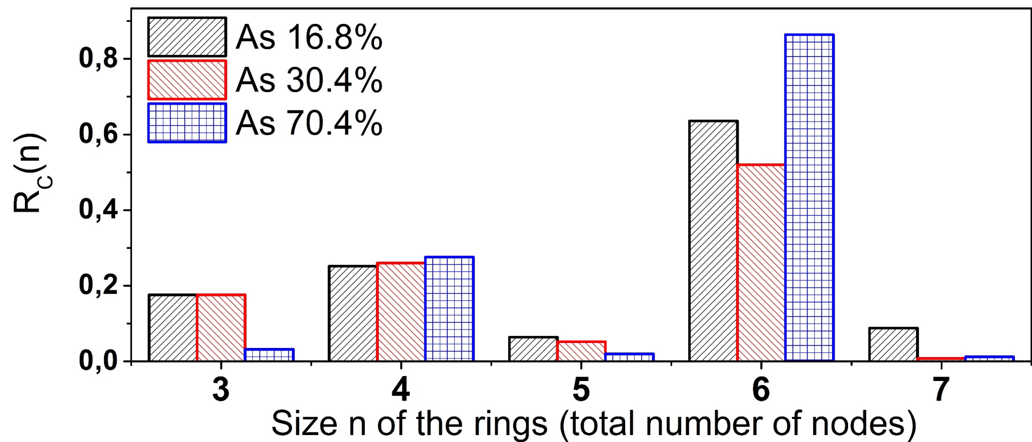


Figure 5.4: Distribution of primitive rings per cell in $a-GaN_{1-x}As_x$ alloys.

Table 5.1: Fraction (%) of different types of bonds over the total number of bonds and average coordination number for an As concentration of $a - GaN_{1-x}As_x$ of $0.168, 0.304$ and $0.704$

| System | atom | with Ga | with N | with As | Coord.Num |
|---|---|---|---|---|---|
| | Ga | 5.59 | 80.44 | 13.97 | 4.008 |
| 16.8% As | N | 94.38 | 5.15 | 0.47 | 4.106 |
| | As | 97.22 | 2.78 | 0 | 3.43 |
| | Ga | 7.17 | 66.93 | 25.9 | 4.016 |
| 30.4% As | N | 96.83 | 2.88 | 0.29 | 3.988 |
| | As | 99.24 | 0.76 | 0 | 3.447 |
| | Ga | 1.67 | 30.42 | 67.92 | 3.84 |
| 70.4% As | N | 98.65 | 1.35 | 0 | 4.0 |
| | As | 98.79 | 0 | 1.21 | 3.75 |

can be seen from Fig.5.4. This indicates that our model has a disordered tetrahedral characteristic as well. The presence of odd-membered rings indicates wrong bonds (homonuclear bonds) in a tetrahedrally coordinated semiconductor. It is noticeable from Fig.5.4 that odd-membered rings contribute much less than even-membered rings and their numbers are decreasing with increasing As concentrations; the rapid decrease of odd membered rings with increasing As concentration is observed. In contrast to odd-membered rings, numbers of even-membered rings are increasing with increasing As concentration. While the 6-membered ring represents the perfect tetrahedral structures, the four-membered rings represents the edge-sharing tetrahedral structures. It has been seen from Fig.5.4 that the edge sharing is increasing slightly with an increase in As concentration. This behavior is in agreement with that of the partial-pair distribution, see Fig.5.1, and triple angle distribution, see Fig.5.3, calculations.

The fraction of different types of bonds over the total number of bonds and the average coordination numbers of each atom types are tabulated for three As concentrations of 16.8%, 30.7% and 70.4%'s in Table 5.1. The same cut-off distances were used as that of the ring statistics. The atoms are said to be bonded if the inter-atomic distance is smaller than the cut-off distance for the related pairs obtained from the partial-pair distribution function and the first minimum of the total radial distribution function. It is observed from Table.5.1 that the fraction of N-Ga and As-Ga pairs are bigger than 97 percent over the total number of bonds for all As concentrations. This shows that N and As atoms are almost entirely bonded with Ga atoms. On the other hand, the number of As atoms bonded to a Ga center increases and the number of N atoms bonded to a Ga center decreases with an increase in As concentration as expected. The opposite behavior of Ga-As and Ga-N pairs indicates that the N nearest neighbors in the network are replaced

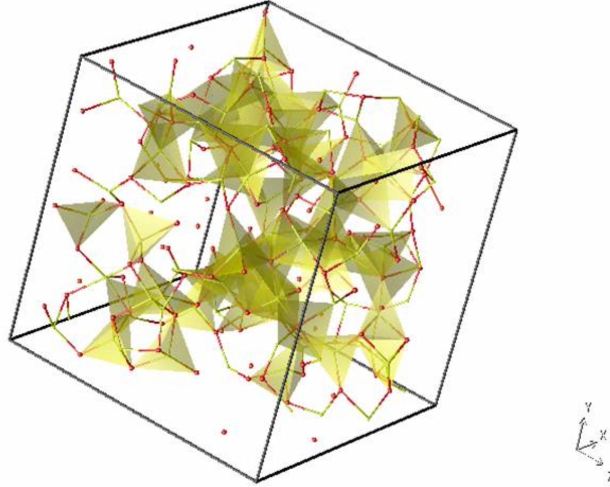


Figure 5.5: Illustration of the presence of tetrahedrally bonded atoms for a $a - GaN_{0.832}As_{0.168}$ system.

by As atoms as As concentration increases. It is also observed that the average coordination number of N is higher than As for all As concentrations. It can be expected since higher electronegativity of N results stronger bond with higher energetic driving force for formation. Thus N-related bonds are formed more probably than As related bonds. Except insignificant amount of As-As pairs in $a - GaN_{0.296}As_{0.704}$ system no As-As homopolar bond is found. With an increase in As concentration there is a decrease in N-N homopolar bonds. The N-As and As-N bonds are rapidly decreased to zero with increasing As concentrations. If we define N-N, N-As, As-N, As-As and Ga-Ga as a defect we can say that the $a-GaN_{0.832}As_{0.168}$ are more defective than $a-GaN_{0.296}As_{0.704}$. It is observed that increasing As concentration improves the amorphous quality by means of bond angle disorder and ring statistics. As reported in the literature the N introduces deeper defect level in the conduction band than As in the valance band thus N can introduce more defect to the structure. This can be interpreted to mean that the higher nitrogen content further distorts the As local environment resulting in an increase in disorder. Number of tetrahedral bonds can also be seen from this from Fig.5.5. The shaded areas illustrates the tetrahedral bonds for $a-GaN_{0.832}As_{0.168}$.

## 5.3 Electronic Properties of Amorphous $GaN_{1-x}As_x$ alloys

In amorphous semiconductors the presence of disorder produces distributions of localized electronic states and these states encroach into the otherwise empty band gap region. These encroaching electronic states commonly referred

to as tail states and have a profound influence on the electronic character of amorphous semiconductors. It is known that many of the tail states associated with amorphous semiconductors are localized by the site disorder, and there exists a critical energy associated with each band, termed as a mobility edge, which separates the localized electronic states from their extended counterparts. In the valence band of an amorphous semiconductor, there are both valence band extended (VBE) and valence band localized (VBL) electronic states, and these states are separated by the valence band mobility edge. Similarly, in the conduction band of an amorphous semiconductor, there are both conduction band extended (CBE) and conduction band localized (CBL) electronic states, and these states are also separated by the conduction band mobility edge [117, 118]. Since the nature of the band tail states are of primary interest in amorphous systems we use first principle DFT calculations within the generalized gradient approximation (GGA) to investigate the electronic properties of $a - GaN_{1-x}As_x$ systems of As concentrations of 16.8%, 27.2%, 30.4%, 44.8% and 70.4%. The investigation of electronic structure has been achieved by means of the electronic density of states (EDOS) and inverse participation ratio (IPR).

The IPR can identify a level as belonging to the band (delocalized), to the band-tail (partially localized), or to the gap (highly localized). The electronic localization of the band tail states can be characterized by inverse participation ratio, IPR, which can be defined as:

$$IPR = \frac{N \sum_{i=1}^{N} [n_i]^2}{(\sum_{i=1}^{N} [n_i])^2} \tag{5.2}$$

where $n_i = |\psi_i|^2$ is the electron density at the site i and the sums extend to all sites N in the system. For an ideally localized state, only one atomic site contributes all the charge and so IPR=1. For a uniformly extended state, the charge contribution per site is uniform and equals 1/N and so IPR=1/N. Thus, large IPR corresponds to localized states. With this measure one can predict the bandgap of the amorphous structure [105, 101, 119, 68].

We calculate the electronic localization of amorphous $GaN_{1-x}As_x$ for various As concentration in order to see how the electronic properties evolve with As concentration. Fig.5.6a-e shows the EDOS and IPR of the $a - GaN_{1-x}As_x$ systems for different As concentrations. According to our electronic density of states calculations the band gap gets narrower with increasing As concentration defining the band gap as the difference between highest occupied molecular orbital (HUMO) and lowest unoccupied molecular orbital (LUMO) based on the $\Gamma$ point. The reduction in bandgap with increasing As concentration is already observed experimentally, see Fig.5.7, showing the validity of our calculations. We estimate the magnitude of band gap as 1.0 eV for 16.8% and 0.3 eV for 70% As concentra-

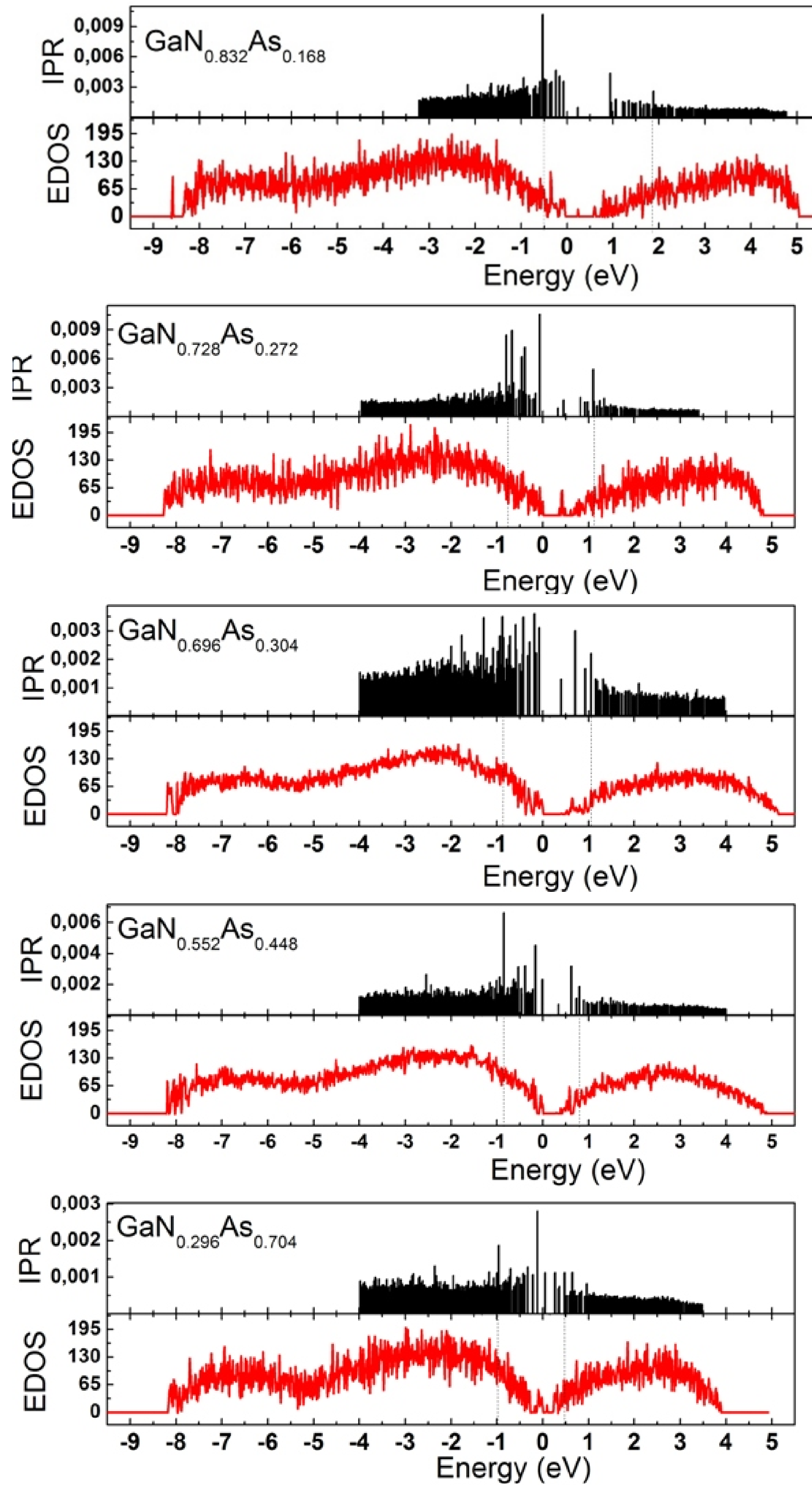


Figure 5.6: The electron density of states and inverse participation ratio (IPR) of $a - GaN_{1-x}As_x$ alloys versus energy for 16.8%, 30.4% and 70.4% As concentrations. The dashed line shows the mobility edges of conduction- and valance-bands.

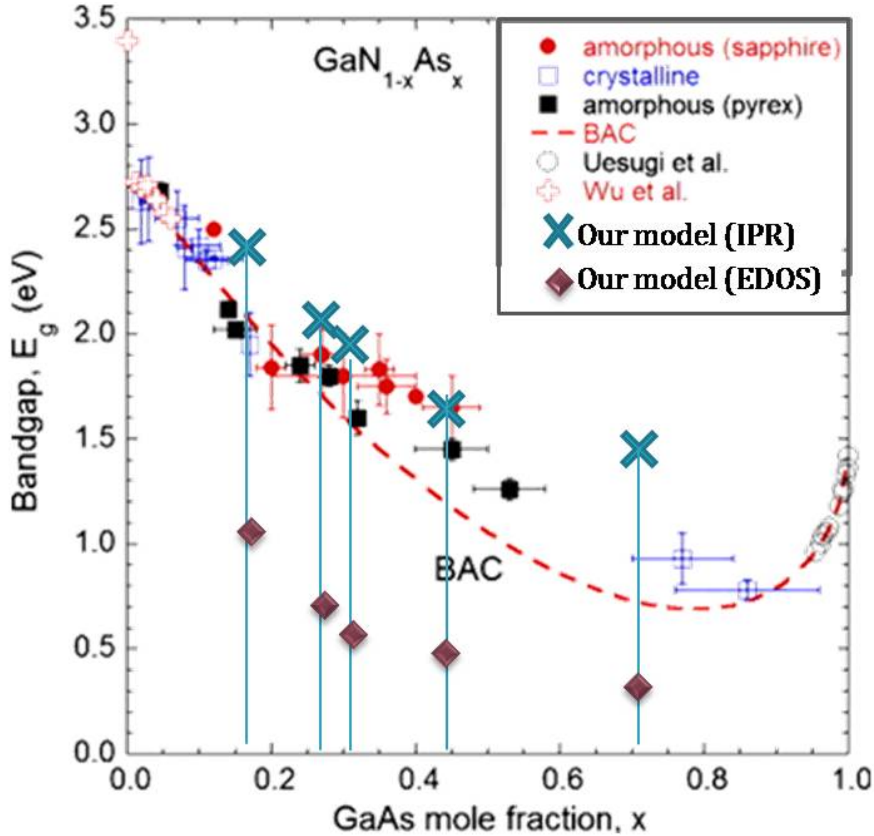


Figure 5.7: Electronic energy gap ($E_g$) versus arsenide concentration x for $GaN_{1-x}As_x$ alloys. Experimental concentration dependence of the bandgap of crystalline and amorphous GaNAs alloys and calculated concentration dependence according to BAC and our model results are shown.

tion according to our EDOS calculations. Our estimations are much smaller than the experimental values as can be seen from Fig.5.7. This is not surprising since density-functional approximations underestimate the band gap. It is clear that both valance- and conduction-band edges are sensitive to As concentration and there are many electronic states in the band gap for stated As concentrations. It is hard to estimate the band gap from the difference of HUMO and LUMO due to the presence of localized states inside and at the edge of the band gap. Instead, we have estimated the mobility edges to approximate the effective band gap. These edges can be defined as the energy points separating the VBE from VBL, and CBE from CBL. In practice, such mobility edges are estimated from the first onset (the big peak) of the localized states near the band edge in the IPR spectrum shown in Fig.5.6. Starting from the onset towards the inside of the VB or CB, the IPR becomes smooth and the states are extended. This is the same procedure as used in [105, 101, 119, 68]. Admittedly, this is a rather approximated method to determine the mobility edge especially when only relatively small systems are calculated. Nevertheless, we believe this will not change

the overall trend and picture of our results. Fig.5.6 depicts the localization of tail- and extended-states for $a-GaN_{1-x}As_x$ as a function of As concentrations. The plots of IPR as a function of increasing As concentration show that the number of band-tail states close to conduction band edges decreases whereas the number of band-tail states close to valence band edges increases. This is because when small amount of As is added into a GaN network, it introduces localized states above the valence band, while when small amount of N is added into a GaAs network, it introduces localized states below the conduction band [3, 4]. Thus, at small As concentration, most localized states are near the valence band edge, and at small N concentration, most localized states are at the conduction band edge. We depict the mobility band gaps of the a-GaNAs systems as 2.41, 2.08, 1.99, 1.64 and 1.43 eV for As concentrations of 16.8%, 27.2%, 30.4%, 44.8% and 70.4%, respectively, from the IPR plots. There is an overall tendency of having narrower band gaps with increasing As concentration as shown in Fig.5.7. Our results are in good agreement with available experimental data. Therefore IPR considered as an effective tool to estimate the band gap of amorphous $a-GaN_{1-x}As_x$ alloys. As a conclusion estimated mobility gap as a function of As concentration x is shown in the Fig.5.7. Estimated energy band gap values are plotted in Fig.5.7 and our results are in agreement with experiment.

### 5.4 Summary

In this work, we present a DFT study of the atomic structure and electronic properties of highly mismatched alloys of amorphous $GaN_{1-x}As_x$ as a function of As concentration. Since continuous random network (CRN) model is an effective method to generate large atomistic model for ideal amorphous systems, this model is used to generate the amorphous $GaN_{1-x}As_x$ network for As concentrations of 16.8%, 27.2%, 30.4%, 44.8% and 70.4%. We have used 250 atom unit cell to represent the a-GaNAs network. Density-functional theory is used to relax the networks in the local density approximation (LDA) and Vanderbilt's Ultrasoft pseudopotential. According to our calculations we conclude that CRN provides an ideal initial network close to minimum energy configuration that can be reached from the first principle calculations for amorphous materials. The calculated bond lengths of 1.95 Å and 2.45 Å for Ga-N and Ga-As, respectively, are in good agreement with the experimental data. Although no homopolar bonds have been found except relaxed $a-GaN_{0.832}As_{0.168}$ alloy system according to radial distribution function calculations, an insignificant numbers of N-N and Ga-Ga is observed in average coordination number calculations.

It has been shown from the ring analysis that our 250 atom $a-GaN_{1-x}As_x$ model has a disordered tetrahedral characteristic. The main contribution of the

number of rings per cell comes from the tetrahedral bonds (fourfold). The minor contributions that come from floating bonds have been decreased and from dangling bonds have been increased with increasing As concentrations. It has also been noticeable from the average coordination number calculations that N and As atoms are almost entirely bonded to Ga atoms and the coordination number of N-Ga and As-Ga pairs are almost unaffected from the variation of As concentration. These results are in agreement with that of the partial-pair distribution and triple angle distribution calculations. The analysis of electronic density of states and inverse participation ratio to estimate the band gap of amorphous $GaN_{1-x}As_x$ alloys have been shown that the band gap gets narrower with increasing As concentration. These calculations also confirms the fact that inverse participation ratio can estimate the bandgap and this estimation is in good agreement with experiments and theoretical band anti-crossing model.

# CHAPTER 6

# CONCLUSIONS

The work carried out in this thesis aims to study the atomic structure and electronic properties of highly mismatched alloys of amorphous $GaN_{1-x}As_x$ as a function of As concentration. The chemically ordered 250-atom models were created for amorphous $GaN_{1-x}As_x$ alloys in the concentration range of $0.17 < x < 0.75$. We have studied the behavior of the structural and electronic properties on these created models. Structural properties of these models were investigated by partial-pair correlation functions, bond angle distributions, ring statistics and average coordination numbers. Similarly, the electronic properties were investigated by electronic density states (EDOS) and inverse participation ratios (IPR) calculations. Although appropriate conclusions have already been presented in the summary part of the related chapters, it is useful to briefly summarize the major conclusions that could be derived from the thesis work in this chapter.

A highly mismatched $GaN_{1-x}As_x$ immiscible alloy system grown successfully by Yu et al. synthesized in the whole composition range using a non-equilibrium low temperature molecular beam epitaxy technique. The crystal structure of $GaN_{1-x}As_x$ thin films are reported wurtzite (crystalline) for $x < 0.17$, amorphous for $0.17 < x < 0.75$, and zinc blend (crystalline) for $x > 0.75$. $GaN_{1-x}As_x$ alloys have following several unique features. The energy gap of $GaN_{1-x}As_x$ changes monotonically across the crystalline amorphous boundary and as the amorphous phase composition is varied. The band gap of $GaN_{1-x}As_x$ system varies from 0.8 eV to 3.4 eV and it has great potential for optoelectronic devices since it covers the full wavelength spectrum from visible to UV light. So, GaNAs is a good candidate for several photovoltaic applications such as high efficiency multi-junction solar cells using a single ternary alloy system. The amorphous nature of this alloy over a wide alloy range can also be advantageous since they can be deposited on low-cost glass substrate, further reducing the cost of such device. $GaN_{1-x}As_x$ alloys show dramatic restructuring of the electronic bands by alloying. The reduction in the band gap can be successfully explained by band anti-crossing (BAC) model by the downward movement of the conduc-

tion band minimum (CBM) for alloys with $x > 0.2$, and to the upward movement of the valance band minimum (VBM) for alloys with $x < 0.2$. This unusual electronic structure and capability for controlling the locations of the conduction band edge (CBE) and valance band edge (VBE) offer unprecedented opportunity for using these alloys for novel solar power conversion devices.

In chapter 4, various computational simulation techniques such as molecular dynamics simulations (classical and *ab initio*) and continuous random network have been applied to study structural and electronic properties of amorphous $GaN_{0.5}As_{0.5}$ alloy. For all models partial pair distribution functions (PDFs) and electronic density of states (EDOS) have been obtained. Comparison of these three methods have been presented. We have also compared the results with experimentally observed electronic structures of amorphous $GaN_{0.5}As_{0.5}$. We have first presented our generated amorphous $GaN_{0.5}As_{0.5}$ alloy from *ab initio* molecular dynamics method through the quenching from the melt. The calculated bond length of Ga-N and Ga-As were $1.95\mathring{A}$ and $2.55\mathring{A}$ , respectively. Although Ga-N bond length found in good agreement with experiment, Ga-As bond length was slightly higher. A considerable amount of N-As, N-N and As-As homopolar bonds were observed in the network before and after the density functional (DFT) relaxation. In addition, it was shown that the obtained amorphous $GaN_{0.5}As_{0.5}$ was not have an energy gap for $a-GaN_{0.5}As_{0.5}$ system in contrast the experimentally observed energy gap using LDA or LDA+C. We have shown that high number of homopolar bond in the structure cause the conduction- and valance-band valley to get close.

Secondly we have generated an amorphous $GaN_{0.5}As_{0.5}$ alloy using classical molecular dynamics method. The calculated bond length of Ga-N and Ga-As were in in good agreement with experiment. The electronic density of states (EDOS) has been obtained without a clear band gap for our generated amorphous $GaN_{0.5}As_{0.5}$ with this technique too. We have shown that by modifying the Tersoff potential, which used as a force field during classical molecular dynamics simulation, it is possible to lower the number of unwanted bonds in the resultant structure. We have shown that the resultant structure had deeper conduction- and valance band valley. Finally, we have generated an initial structure by means of CRN which is an alternative method to obtain realistic amorphous structure. It has been observed that all bond lengths were already close to their ideal values in these initial structures. It was calculated that the resultant structure of $a - GaN_{0.552}As_{0.448}$ do not have any homopolar or unwanted bonds after DFT relaxation. The energy band gap of resultant $a - GaN_{0.552}As_{0.448}$ structure was observed as a 0.8 eV which similar to the experimental results. Our calculations have confirmed that the CRN is a reliable method for modeling $a-GaN_{0.552}As_{0.448}$

for such a highly ionic structure.

In chapter 5, a systematic study of atomic structure and electronic properties of amorphous $GaN_xAs_{1-x}$ as a function of As concentration by CRN model was carried out. We have generated an amorphous $GaN_xAs_{1-x}$ network for As concentrations of 16.8%, 27.2%, 30.4%, 44.8% and 70.4%. It was shown that the continuous random network structures relaxed by DFT simulations has minor changes in structural properties for all generated networks. We have also determined that the calculated bond lengths are in good agreement with the experimental data. The investigation of network topology by means of coordination numbers, ring statistics, and bond angle distribution of these system showed that the generated systems have slightly disordered tetrahedral and bond angle characteristics which decrease with increasing As concentration. It has been observed that $a-GaN_{0.832}As_{0.168}$ is more defective than $a-GaN_{0.296}As_{0.704}$. It has been found that increasing As concentration results a decrease in N-N homopolar bonds as reported in the literature. A clear band gap is observed for all systems. The electronic localization of the band tail states were obtained from the inverse participation ratio (IPR). We have estimated the mobility band gap from a detailed investigation of IPR calculations. The mobility band gaps of a-GaNAs systems have been found as 2.41, 2.08, 1.99, 1.64 and 1.43 eV for As concentrations of 16.8%, 27.2%, 30.4%, 44.8% and 70.4%, respectively, which were in good agreement with available experiments. It has then been concluded that the IPR is an effective tool to estimate the band gap of amorphous $a-GaN_{1-x}As_x$ alloys. The plots of IPR as a function of increasing As or decreasing N concentration have revealed that the number of band-tail states close to conduction band edges decreases whereas the number of band-tail states close to valence band edges increases. This is in agreement with CBAC and VBAC model. As described in BAC the restructuring of the conduction (valence) band of the alloys were due to the anti-crossing interaction between localized impurity states and the extended conduction (valence) band states of the matrix. In low As concentration of $GaN_xAs_{1-x}$ which corresponds to N-rich GaNAs, more metallic and larger arsenic atom replaces the highly electronegative nitrogen anion and produces arsenic defect in GaN. Thus the number of localized impurity states close to VBE increases with increasing As concentration which is in agreement with VBAC. Similarly, an increase in N concentration corresponds to an increment of band-tail states close to CBE. Our analysis has been revealed that the band gap gets narrower with increasing As concentration in agreement both with experimental data and BAC model. We have then concluded that the CRN model is an ideal model to create initial structure to obtain realistic amorphous structures.

# LIST OF REFERENCES


[1] Yu, K. M., Novikov, S. V., Broesler, R., Demchenko, I. N., Denlinger, J. D., Liliental-Weber, Z., Luckert, F., Martin, R. W., Walukiewicz, W., Foxon, C. T. (2009). Highly mismatched crystalline and amorphous $GaN_{1-x}As_x$ alloys in the whole composition range. *Journal of Applied Physics* **106 10** 103709.

[2] Levander, A., Yu, K., Novikov, S., Tseng, A., Foxon, C., Dubon, O., Wu, J., Walukiewicz, W. (2010). GaNBi: Extremely mismatched semiconductor alloys. *Applied Physics Letters* **97** 101906–101909.

[3] Uesugi, K., Morooka, N., Suemune, I. (1999). Reexamination of N composition dependence of coherently grown GaNAs band gap energy with high-resolution x-ray diffraction mapping measurements. *Applied Physics Letters* **74 9** 1254–1256.

[4] Wu, J., Walukiewicz, W., Yu, K., Denlinger, J., Shan, W., Ager III, J., Kimura, A., Tang, H., Kuech, T. (2004). Valence band hybridization in N-rich $GaN_{1-x}As_x$ alloys. *Physical Review B* **70 11** 115214–115221.

[5] Takahashi, K., Yoshikawa, A., Sandhu, A., 2007. Wide Bandgap Semiconductors: Fundamental Properties and Modern Photonic and Electronic Devices. Springer.

[6] Adachi, S., Capper, P., Kasap, S., Willoughby, A., 2009. Properties of Semiconductor Alloys: Group-IV, III-V and II-VI Semiconductors. Wiley Series in Materials for Electronic & Optoelectronic Applications, Wiley.

[7] Adachi, S., 1992. Physical Properties of III-V Semiconductor Compounds. Wiley-Interscience publication, Wiley.

[8] Vegard, L. (1921). Die konstitution der mischkristalle und die raumfüllung der atome. *Zeitschrift für Physik A Hadrons and Nuclei* **5 1** 17–26.

[9] Van Vechten, J., Bergstresser, T. (1970). Electronic structures of semiconductor alloys. *Physical Review B* **1 8** 3351.

[10] Richardson, D., Hill, R. (1972). The origins of energy gap bowings in substitutional semiconductor alloys. *Journal of Physics C: Solid State Physics* **5 8** 821.

[11] Nordheim, L. (1931). Zur Elektronentheorie der Metalle. I. *Annalen der Physik* **401 5** 607–640.

[12] Wu, J., 2002. Band anticrossing effects in highly mismatched semiconductor alloys. Ph.D. thesis, University of California, Berkeley.

[13] Pauling, L. (1932). The nature of the chemical bond. IV. The energy of single bonds and the relative electronegativity of atoms. *Journal of the American Chemical Society* **54** **9** 3570–3582.

[14] Pauling, L., 1960. The Nature of the Chemical Bond and the Structure of Molecules and Crystals: An Introduction to Modern Structural Chemistry. George Fisher Baker lectures, Cornell University Press.

[15] Walukiewicz, W., Shan, W., Yu, K., Ager III, J., Haller, E., Miotkowski, I., Seong, M., Alawadhi, H., Ramdas, A. (2000). Interaction of localized electronic states with the conduction band: Band anticrossing in II-VI semiconductor ternaries. *Physical Review Letters* **85** **7** 1552–1555.

[16] Shan, W., Walukiewicz, W., Ager III, J., Haller, E., Geisz, J., Friedman, D., Olson, J., Kurtz, S. R. (1999). Band anticrossing in GaInNAs alloys. *Physical Review Letters* **82** **6** 1221.

[17] Erol, A., 2008. Dilute III-V Nitride Semiconductors and Material Systems: Physics and Technology, volume 105. Springer.

[18] Sólyom, J., 2007. Fundamentals of the Physics of Solids: Volume 1: Structure and Dynamics. Springer-Verlag Berlin Heidelberg.

[19] Basak, C., Sengupta, A., Kamath, H. (2003). Classical molecular dynamics simulation of $UO_2$ to predict thermophysical properties. *Journal of Alloys and Compounds* **360** **1** 210–216.

[20] Henini, M., 2004. Dilute nitride semiconductors. Access Online via Elsevier.

[21] Hjalmarson, H. P., Vogl, P., Wolford, D., Dow, J. D. (1980). Theory of substitutional deep traps in covalent semiconductors. *Physical Review Letters* **44** 810–813.

[22] Wolford, D., Bradley, J., Fry, K., Thompson, J., 1984. Physics of Semiconductors ed JD Chadi and WA Harrison.

[23] Thomas, D., Hopfield, J., Frosch, C. (1965). Isoelectronic traps due to nitrogen in gallium phosphide. *Physical Review Letters* **15** **22** 857.

[24] Yu, K., Walukiewicz, W., Wu, J., Shan, W., Beeman, J., Scarpulla, M., Dubon, O., Becla, P. (2003). Diluted II-VI oxide semiconductors with multiple band gaps. *Physical Review Letters* **91** **24** 246403.

[25] Mattila, T., Zunger, A. (1998). Deep electronic gap levels induced by isovalent P and As impurities in GaN. *Physical Review B* **58** **3** 1367.

[26] Trumbore, F. A., Gershenzon, M., Thomas, D. G. (1966). Luminescence due to the isoelectronic substitution of bismuth for phosphorus in gallium phosphide. *Applied Physics Letters* **9** **1** 4–6.

[27] Alberi, K., Wu, J., Walukiewicz, W., Yu, K., Dubon, O., Watkins, S., Wang, C., Liu, X., Cho, Y.-J., Furdyna, J. (2007). Valence-band anticrossing in mismatched III-V semiconductor alloys. *Physical review B* **75** **4** 045203.

[28] Goldman, R., Feenstra, R., Briner, B., OSteen, M., Hauenstein, R. (1996). Atomic-scale structure and electronic properties of GaN/GaAs superlattices. *Applied Physics Letters* **69** **24** 3698–3700.

[29] Bi, W., Tu, C. (1997). Bowing parameter of the band-gap energy of $GaN_xAs_{1-x}$. *Applied Physics Letters* **70** **12** 1608–1610.

[30] Guido, L., Mitev, P., Gherasimova, M., Gaffey, B. (1998). Electronic properties of arsenic-doped gallium nitride. *Applied Physics Letters* **72** **16** 2005–2007.

[31] Li, X., Kim, S., Reuter, E., Bishop, S., Coleman, J. (1998). The incorporation of arsenic in GaN by metalorganic chemical vapor deposition. *Applied Physics Letters* **72** **16** 1990–1992.

[32] Wu, J., Shan, W., Walukiewicz, W. (2002). Band anticrossing in highly mismatched III–V semiconductor alloys. *Semiconductor Science and Technology* **17** **8** 860.

[33] Klar, P., Gruning, H., Heimbrodt, W., Koch, J., Hohnsdorf, F., Stolz, W., Vicente, P., Camassel, J. (2000). From N isoelectronic impurities to N-induced bands in the $GaN_xAs_{1-x}$ alloy. *Applied Physics Letters* **76** **23** 3439–3441.

[34] Uesugi, K., Suemune, I., Hasegawa, T., Akutagawa, T., Nakamura, T. (2000). Temperature dependence of band gap energies of GaAsN alloys. *Applied Physics Letters* **76** **10** 1285–1287.

[35] Plaza, J., Castaño, J., García, B., Carrère, H., Bedel-Pereira, E. (2005). Temperature dependence of photoluminescence and photoreflectance spectra of dilute GaAsN alloys. *Applied Physics Letters* **86** **12** 121918–121918.

[36] Cheng-Chun, T., Jun-Chi, C., Yun-Ze, L., Hong-Xing, Y., Bin, S., Hong-Di, Z. (2011). Preparation of curled microfibers by electrospinning with tip collector. *Chinese Physics Letters* **28** **5** 056801.

[37] Kimura, A., Tang, H., Kuech, T. (2004). Growth of GaNAs alloys on the N-rich side with high As content by metalorganic vapor phase epitaxy. *Journal of Crystal Growth* **265** **1** 71–77.

[38] Pozina, G., Ivanov, I., Monemar, B., Thordson, J., Andersson, T. (1998). Properties of molecular-beam epitaxy-grown GaNAs from optical spectroscopy. *Journal of Applied Physics* **84** **7** 3830–3835.

[39] Kimura, A., Paulson, C. A., Tang, H., Kuech, T. F. (2004). Epitaxial GaNAs layers with high As content grown by metalorganic vapor phase epitaxy and their band gap energy. *Applied Physics Letters* **84** 1489.

[40] Zhao, C.-Z., Li, N.-N., Wei, T., Tang, C.-X., Lu, K.-Q. (2012). A model for the bandgap energy of the N-rich GaNAs (0 x 0.07). *Applied Physics Letters* **100 14** 142112–142112.

[41] Broesler, R. J., Jr., 2010. Characterization of Novel Semiconductor Alloys for Band Gap Engineering. Ph.D. thesis, University of California, Berkeley.

[42] Yuen, H. B., 2006. Growth and characterization of dilute nitride antimonides for long-wavelength optoelectronics. Ph.D. thesis, Stanford University.

[43] Weyers, M., Sato, M., Ando, H. (1992). Red shift of photoluminescence and absorption in dilute GaAsN alloy layers. *Japanese Journal of Applied Physics* **31 7A** L853–L855.

[44] Zhang, S., Wei, S.-H. (2001). Nitrogen solubility and induced defect complexes in epitaxial GaAs: N. *Physical Review Letters* **86 9** 1789.

[45] Foxon, C., Harrison, I., Novikov, S., Winser, A., Campion, R., Li, T. (2002). The growth and properties of GaN: As layers prepared by plasma-assisted molecular beam epitaxy. *Journal of Physics: Condensed Matter* **14 13** 3383.

[46] Iwata, K., Asahi, H., Asami, K., Kuroiwa, R., ichi Gonda, S. (1998). GaN-Rich Side of GaNAs Grown by Gas Source Molecular Beam Epitaxy. *Japanese Journal of Applied Physics* **37 Part 1, No. 3B** 1436–1439.

[47] Zhao, Y., Deng, F., Lau, S., Tu, C. (1998). Effects of arsenic in gas-source molecular beam epitaxy. *Journal of Vacuum Science & Technology B: Microelectronics and Nanometer Structures* **16 3** 1297–1299.

[48] Scarpulla, M., Dubon, O., Yu, K., Monteiro, O., Pillai, M., Aziz, M., Ridgway, M. (2003). Ferromagnetic GaMnAs produced by ion implantation and pulsed-laser melting. *Applied Physics Letters* **82** 1251.

[49] Yu, K., Walukiewicz, W., Beeman, J., Scarpulla, M., Dubon, O., Pillai, M., Aziz, M. (2002). Enhanced nitrogen incorporation by pulsed laser annealing of GaNAs formed by N ion implantation. *Applied Physics Letters* **80** 3958.

[50] Ohno, H. (1998). Making nonmagnetic semiconductors ferromagnetic. *Science* **281 5379** 951–956.

[51] Kaxiras, E., 2003. Atomic and electronic structure of solids. Cambridge University Press.

[52] Street, R. A., 2005. Hydrogenated amorphous silicon. Cambridge University Press.

[53] Pan, Y., 2009. Topological Origin of the Urbach Tail. Ph.D. thesis, Ohio University.

[54] Gould, H., Tobochnik, J., Wolfgang, C., 2005. An introduction to computer simulation methods: applications to physical systems. Addison-Wesley Longman Publishing Co., Inc.

[55] de Pablo, J. J., Curtin, W. A. (2007). Multiscale modeling in advanced materials research: challenges, novel methods, and emerging applications. *MRS Bulletin* **32** **11** 905–911.

[56] Horstemeyer, M. F., 2001. From Atoms to Autos-A new Design Paradigm Using Microstructure-Property Modeling Part 1: Monotonic Loading Conditions. Technical report, Sandia National Labs., Albuquerque, NM (US); Sandia National Labs., Livermore, CA (US).

[57] Horstemeyer, M., Wang, P. (2003). Cradle-to-grave simulation-based design incorporating multiscale microstructure-property modeling: Reinvigorating design with science. *Journal of Computer-aided Materials Design* **10** **1** 13–34.

[58] Campbell, C., Olson, G. (2000). Systems design of high performance stainless steels I. Conceptual and computational design. *Journal of Computer-aided Materials Design* **7** **3** 145–170.

[59] Alder, B. J., Wainwright, T. (1959). Studies in molecular dynamics. I. General method. *The Journal of Chemical Physics* **31** 459.

[60] Rahman, A. (1964). Correlations in the motion of atoms in liquid argon. *Physical Review* **136** **2A** A405.

[61] Rahman, A., Stillinger, F. H. (1974). Propagation of sound in water. A molecular-dynamics study. *Physical Review A* **10** **1** 368.

[62] Verlet, L. (1967). Computer" experiments" on classical fluids. I. Thermodynamical properties of Lennard-Jones molecules. *Physical Review* **159** **1** 98.

[63] Verlet, L. (1968). Computer "Experiments" on Classical Fluids. II. Equilibrium Correlation Functions. *Physical Review* **165** 201–214.

[64] Berendsen, H. J., Postma, J. P. M., van Gunsteren, W. F., DiNola, A., Haak, J. (1984). Molecular dynamics with coupling to an external bath. *The Journal of Chemical Physics* **81** 3684.

[65] Andersen, H. C. (1980). Molecular dynamics simulations at constant pressure and/or temperature. *The Journal of Chemical Physics* **72** **4** 2384.

[66] Hoover, W. G. (1985). Canonical dynamics: Equilibrium phase-space distributions. *Physical Review A* **31** **3** 1695.

[67] Nosé, S. (1984). A molecular dynamics method for simulations in the canonical ensemble. *Molecular physics* **52** **2** 255–268.

[68] Drabold, D. (2009). Topics in the theory of amorphous materials. *The European Physical Journal B* **68** **1** 1–21.

[69] Car, R., Parrinello, M. (1985). Unified approach for molecular dynamics and density-functional theory. *Physical Review Letters* **55** **22** 2471.

[70] Sarnthein, J., Pasquarello, A., Car, R. (1995). Structural and Electronic Properties of Liquid and Amorphous $SiO_2$: An Ab Initio Molecular Dynamics Study. *Physical Review Letters* **74 23** 4682.

[71] Massobrio, C., Pasquarello, A., Car, R. (2001). Short-and intermediate-range structure of liquid $GeSe2$. *Physical Review B* **64 14** 144205.

[72] Giacomazzi, L., Massobrio, C., Pasquarello, A. (2007). First-principles investigation of the structural and vibrational properties of vitreous $GeSe_2$. *Physical Review B* **75 17** 174207.

[73] Cobb, M., Drabold, D., Cappelletti, R. (1996). Ab initio molecular-dynamics study of the structural, vibrational, and electronic properties of glassy $GeSe_2$. *Physical Review B* **54 17** 12162.

[74] Vink, R., 2002. Computer Simulations of Amorphous Semiconductors. Ph.D. thesis, Utrecht University.

[75] Luedtke, W., Landman, U. (1988). Preparation and melting of amorphous silicon by molecular-dynamics simulations. *Physical Review B* **37 9** 4656.

[76] Cook, S. J., Clancy, P. (1993). Comparison of semi-empirical potential functions for silicon and germanium. *Physical Review B* **47 13** 7686.

[77] Hohenberg, P., Kohn, W. (1964). Inhomogeneous electron gas. *Physical review* **136 3B** B864.

[78] Kohn, W., Sham, L. J. (1965). Self-consistent equations including exchange and correlation effects. *Physical Review* **140 4A** A1133.

[79] Perdew, J. P., Wang, Y. (1992). Accurate and simple analytic representation of the electron-gas correlation energy. *Physical Review B* **45 23** 13244.

[80] Monkhorst, H. J., Pack, J. D. (1976). Special points for Brillouin-zone integrations. *Physical Review B* **13 12** 5188–5192.

[81] Vanderbilt, D. (1990). Soft self-consistent pseudopotentials in a generalized eigenvalue formalism. *Physical Review B* **41 11** 7892.

[82] Lee, S., 2008. First Principles-based Atomistic Modeling of the Structure and Nature of Amorphous Gold-silicon Alloys and Their Application to Silicon Nanowire Synthesis. Ph.D. thesis, The University of Texas at Austin.

[83] Zachariasen, W. H. (1932). The atomic arrangement in glass. *Journal of the American Chemical Society* **54 10** 3841–3851.

[84] Bell, R. J., Dean, P. (1966). Properties of Vitreous Silica: Analysis of Random Network Models. *Nature* **212 5068** 1354–1356.

[85] Polk, D. (1971). Structural model for amorphous silicon and germanium. *Journal of Non-Crystalline Solids* **5 5** 365–376.

[86] Henderson, D., Herman, F. (1972). Simulation of the atomic arrangements in amorphous silicon and germanium. *Journal of Non-Crystalline Solids* **8** 359–363.

[87] Wooten, F., Winer, K., Weaire, D., et al. (1985). Computer generation of structural models of amorphous Si and Ge. *Physical Review Letters* **54 13** 1392–1395.

[88] Metropolis, N., Rosenbluth, A. W., Rosenbluth, M. N., Teller, A. H., Teller, E. (1953). Equation of state calculations by fast computing machines. *The Journal of Chemical Physics* **21** 1087.

[89] Keating, P. N. (1966). Effect of Invariance Requirements on the Elastic Strain Energy of Crystals with Application to the Diamond Structure. *Physical Review* **145** 637–645.

[90] Djordjević, B., Thorpe, M., Wooten, F. (1995). Computer model of tetrahedral amorphous diamond. *Physical Review B* **52 8** 5685.

[91] Barkema, G. T., Mousseau, N. (2000). High-quality continuous random networks. *Physical Review B* **62 8** 4985.

[92] Wright, A. C., Thorpe, M. F. (2013). Eighty years of random networks. *Physica Status Solidi (b)* **250 5** 931–936.

[93] S, F. D. (1991). Computation of rings statistics for network models of solids. *Physical Review B* **44 10** 4925–4930.

[94] Le Roux, S., Jund, P. (2010). Ring statistics analysis of topological networks: New approach and application to amorphous $GeS_2$ and $SiO_2$ systems. *Computational Materials Science* **49 1** 70–83.

[95] King, S. V. (1967). Ring configurations in a random network model of vitreous silica. *Nature* **213** 1112–1113.

[96] Guttman, L. (1990). Ring structure of the crystalline and amorphous forms of silicon dioxide. *Journal of Non-Crystalline Solids* **116 23** 145 – 147.

[97] Franzblau, D. (1991). Computation of ring statistics for network models of solids. *Physical Review B* **44 10** 4925.

[98] Goetzke, K., Klein, H.-J. (1991). Properties and efficient algorithmic determination of different classes of rings in finite and infinite polyhedral networks. *Journal of Non-crystalline Solids* **127 2** 215–220.

[99] Yuan, X., Cormack, A. (2002). Efficient algorithm for primitive ring statistics in topological networks. *Computational Materials Science* **24 3** 343–360.

[100] Abtew, T. A., 2007. Structure and carrier transport in amorphous semiconductors. Ph.D. thesis, Ohio University.

[101] Mota, F., Justo, J., Fazzio, A. (2002). Defect centers in a-SiNx: electronic and structural properties. *Brazilian journal of physics* **32 2A** 436–438.

[102] Mousseau, N., Barkema, G. T. (1999). Exploring high-dimensional energy landscapes. *Computing in Science & Engineering* **1** **2** 74–80.

[103] Nakhmanson, S., Voyles, P., Mousseau, N., Barkema, G., Drabold, D. (2001). Realistic models of paracrystalline silicon. *Physical Review B* **63** **23** 235207.

[104] Vink, R., Barkema, G. (2003). Large well-relaxed models of vitreous silica, coordination numbers, and entropy. *Physical Review B* **67** **24** 245201.

[105] Cai, B., Drabold, D. (2011). Properties of amorphous GaN from first-principles simulations. *Physical Review B* **84** **7** 075216–075222.

[106] Cai, B., Drabold, D. (2009). Ab initio models of amorphous InN. *Physical Review B* **79** **19** 195204–195208.

[107] Chen, K., Drabold, D. A. (2002). First principles molecular dynamics study of amorphous $Al_xGa_{1-x}N$ alloys. *Journal of Applied Physics* **91** **12** 9743–9751.

[108] Mousseau, N., Barkema, G. (2004). Binary continuous random networks. *Journal of Physics: Condensed Matter* **16** **44** S5183–S5190.

[109] Pollak, F. H. (1990). Effects of homogeneous strain on the electronic and vibrational levels in semiconductors. *Strained-Layer Superlattices* **32** 17–53.

[110] Powell, D., Migliorato, M., Cullis, A. (2007). Optimized Tersoff potential parameters for tetrahedrally bonded III-V semiconductors. *Physical Review B* **75** **11** 115202.

[111] Nord, J., Albe, K., Erhart, P., Nordlund, K. (2003). Modelling of compound semiconductors: analytical bond-order potential for gallium, nitrogen and gallium nitride. *Journal of Physics: Condensed Matter* **15** **32** 56495662.

[112] Albe, K., Nordlund, K., Nord, J., Kuronen, A. (2002). Modeling of compound semiconductors: Analytical bond-order potential for Ga, As, and GaAs. *Physical Review B* **66** **3** 035205.

[113] Levine, B. G., Stone, J. E., Kohlmeyer, A. (2011). Fast analysis of molecular dynamics trajectories with graphics processing unitsRadial distribution function histogramming. *Journal of Computational Physics* **230** **9** 3556–3569.

[114] Ridgway, M., Glover, C., Foran, G., Yu, K. (1998). Characterization of the local structure of amorphous GaAs produced by ion implantation. *Journal of Applied Physics* **83** **9** 4610–4614.

[115] Ridgway, M., Everett, S., Glover, C., Kluth, S., Kluth, P., Johannessen, B., Hussain, Z., Llewellyn, D., Foran, G., Azevedo, G. d. M. (2006). Atomic-scale structure of irradiated GaN compared to amorphised GaP and GaAs. *Nuclear Instruments and Methods in Physics Research Section B: Beam Interactions with Materials and Atoms* **250** **1** 287–290.

[116] Biswas, P., Atta-Fynn, R., Drabold, D. (2004). Reverse Monte Carlo modeling of amorphous silicon. *Physical Review B* **69** **19** 195207–195212.

[117] Orapunt, F., O Leary, S. K. (2008). Optical transitions and the mobility edge in amorphous semiconductors: A joint density of states analysis. *Journal of Applied Physics* **104** **7** 073513.

[118] Cohen, M. H., Fritzsche, H., Ovshinsky, S. (1969). Simple band model for amorphous semiconducting alloys. *Physical Review Letters* **22** 1065–1068.

[119] Chen, H., Chen, K., Drabold, D., Kordesch, M. (2000). Band gap engineering in amorphous AlGaN: Experiment and ab initio calculations. *Applied Physics Letters* **77** 1117–1120.

## LIST OF PUBLICATIONS

[1] Bakır Kandemir, E., Gönül, B., Barkema, G.T., Yu, K.M., Walukiewicz, W. and Wang, L.W. (2014). Modeling of the atomic structure and electronic properties of amorphous $GaN_{1-x}As_x$. *Computational Materials Science* **82** 100 – 106.

[2] Gönül, B., Bakır, E. and Köksal, K. (2006). Analysis of the band alignment of highly strained indium-rich GaInNAs QWs on InP substrates. *Semiconductor Science and Technology* **21** **7** 876.

[3] Gönül, B.,Köksal, K. and Bakır, E. (2006). An alternative treatment for yukawa-type potentials. *Physica Scripta* **73** **3** 279.

[4] Gönül, B., Bakır, E. and Köksal, K. (2008). Two electrons in a quantum dot: A unified approach. *International Journal of Theoretical Physics* **47** **12** 3091–3100.

[5] Gönül, B.,Köksal, K. and Bakır, E. (2007). A theoretical investigation of carrier and optical mode confinement in GaInNAs QWs on GaAs and InP substrates. *Physica Status Solidi C Current Topics* **4** 671–673.

[6] Gönül, B.,Köksal, K. and Bakır, E. (2006). Comparison of the band alignment of strained and strain-compensated GaInNAs QWs on GaAs and InP substrates. *Physica E: Low-dimensional Systems and Nanostructures* **31** **2** 148–154.

[7] Tuna, Ö., Hahn, H., Bakır Kandemir, E., Giesen, C., Yablonskii, G. P., Lutsenko, E. V., Kalisch, H., Vescan, A. and Heuken, M. (2012). MOVPE growth and characterization of thick Mg-doped InGaN. ICMOVPE-16. Busan, Korea.

[8] Tuna, Ö., Kirste, R., Mohn, S., Bakır Kandemir, E., Giesen, C., Kalisch, H., Vescan, A., Hoffman, A. and Heuken, M. (2012). Comprehensive study on the structural, optical and electrical properties of MOCVD-grown high-quality InN and the influenced of the V/III ratio. IWN2012. Sapporo, Japan.

[9] Bakır Kandemir, E., Giesen and Heuken, M. (2012). a-plane Indium Nitride films growth by MOVPE on r-plane Sapphire. Marie Curie Actions Conference 2012. Dublin, Ireland.

[10] Bakır Kandemir, Tuna, Ö., Kure, T., Giesen, C., Kalisch, H., Vescan, A., Hoffman, A. and Heuken, M. (2012). Optimization of a-plane InN films by MOCVD on r-plane Sapphire. IWN2012. Sapporo, Japan.

[11] Tuna, Ö., Hahn, H., Bakır Kandemir, E., Boyd, A., Giesen, C., Yablonskii, G. P., Lutsenko, E. V., Kalisch, H., Vescan, A. and Heuken, M. (2012). MOCVD of thick high In content InGaN and InGaN:Mg layers. NanoTR-8. Ankara, Turkey.

[12] Bakır, E., Wang, L.W. and Walukiewicz., W. (2010). MRS spring meeting. A DFT Study of Atomic Structure and Electronic Properties of Highly Mismatched GaNAs Alloy. San Francisco, USA.

[13] Bakır, E. (2008). Fundamental ideas of density functional theory and basic applications. ISCBPU-6. Bodrum, Turkey.

[14] Gönül, B., Bakır, E. and Köksal, K. (2007). Two electrons in a quantum dot: a unified approach. NanoTR-3. Ankara, Turkey.

[15] Gönül, B., Oduncuoğlu, M., Bakır, E. and Köksal, K. (2006). A theoretical study of the laser characteristics of GaInNAs QWs. ICSNN. İstanbul, Turkey.

[16] Bakır, E., Köksal, K. and Gönül, B. (2006). The investigation of the band alignment of compressively/tensile strained and strain-compensated GaInNAs QWs on GaAs and InP substrate. NanoTR-2. Ankara, Turkey.

[17] Köksal, K., Gönül, B. and Bakır, E. (2006). A theoretical investigation of carrier and optical mode confinement in GaInNAs QWs on GaAs and InP substrates. ICSNN. İstanbul, Turkey.

[18] Bakır, E. and Köksal, K. and Gönül, B. (2005). A theoretical comparative study of dilute GaInNAs on GaAs and InP substrates. TFD 23. Mula, Turkey.